KEK Proceedings 91-5
July 1991
H/R

RADIATION DETECTORS AND THEIR USES

Proceedings of the Sixth Workshop on
Radiation Detectors and Their Uses

KEK, Japan, January 29-30, 1991

edited by

M. MIYAJIMA and S. SASAKI

NATIONAL LABORATORY FOR
HIGH ENERGY PHYSICS

RADIATION DETECTORS AND THEIR USES

Proceedings of the Sixth Workshop on Radiation Detectors and Their Uses

KEK, Japan, January 29-30, 1991

edited by

M. MIYAJIMA and S. SASAKI
National Laboratory for High Energy Physics

National Laboratory for High Energy Physics, 1991

KEK Reports are available from:

Technical Information & Library
National Laboratory for High Energy Physics
1-1 Oho, Tsukuba-shi
Ibaraki-ken, 305
JAPAN

Phone: 0298-64-1171
Telex: 3652-534 (Domestic)
(0)3652-534 (International)
Fax: 0298-64-4604
Cable: KEKOHO

FOREWORD

The Sixth Workshop on Radiation Detectors and Their Uses was held at the National Laboratory for High Energy Physics (KEK) from January 29 to 30, 1991. The workshop has been hosted by the Radiation Safety Control Center, KEK.

The main purpose of the workshop is focused on most of current experimental and theoretical activities in the various fields, which handle ionizing radiation, from a view point of developing radiation detectors. The development and the application of radiation detectors are closely related to various fields, such as radiation physics, radiation chemistry, atomic-molecular physics, high-energy physics and so on. There are, however, little opportunities for researchers working on the different fields to discuss related problems in Japan. It was also aimed at promoting effective collaboration among the researchers in the above different fields.

In this workshop, a particular emphasis was put on a topic "Laser Application". The workshop consisted of 22 contributions in which 6 talks related to this topic were presented. It was attended by above 100 participants. There was extensive discussion on subjects of common interest.

Finally, we would like to express our great appreciation to all authors who have prepared manuscript quickly for the timely publication of this proceedings. We also expect to receive many contributions from various fields at the next workshop.

M. Miyajima, KEK
S. Sasaki, KEK

TABLE OF CONTENTS

EXTREMELY-HIGH VACUUM PRESSURE MEASUREMENT BY LASER IONIZATION

Kiyohide KOKUBUN
Electrotechnical Laboratory
1-1-4, Umezono, Tsukuba, Ibaraki, 305 JAPAN

1. INTRODUCTION

The laser-ionization method has a very high sensitivity for detecting atoms or molecules. Hurst et al successfully detected a single Cs atom amongst many other molecules by means of resonance ionization spectroscopy (RIS) developed by them[1]. Noting this high sensitivity, the authors have attempted to apply the laser-ionization method to measuring gas pressure, particularly, in the range of ultrahigh vacuum (UHV) to extremely-high vacuum (XHV, $<1x10^{-9}$ Pa).

Presently, the hot cathode ionization gauge (B-A gauge) is most conventionally used for measuring gas pressure in the range of high-vacuum to ultra-high-vacuum. This type of gauge, however, has disadvantages such as soft X-ray effect, the generation of thermal desorption ions, the releasing of gaseous molecules or atoms from the heated filament etc. For these reasons, the hot cathode ionization gauge is unreliable and has the limit for measuring pressure in the range of XHV.

On the other hand, the pressure measurement using the laser has not these disadvantages, and has the advantage that the sensitivity of detecting atoms and molecules is extremely high. This method, therefore, might be very effective for the pressure measurement in the XHV region.

The pressure measurement utilizing the laser-ionization method is based on the principle that when a laser light is focused through a lens, the amount of atom or molecule ions generated in the focused space region (ionization space) is proportional to the

gas pressure. In this paper, the experimental results are presented for the nonresonant multiphoton ionization characteristics of various kinds of gases, the ion-detection systems with high sensitivity, and an extremely-high vacuum system prepared for the laser-ionization experiment in the XHV region.

2. NONRESONANT MULTIPHOTON IONIZATION CHARACTERISTICS OF VARIOUS KINDS OF GASES

In the laser-ionization technique, there are the resonant multiphoton ionization method and the nonresonant multiphoton ionization one. From the standpoint of measuring the total pressure of a gas, the authors have adopted the latter. To obtain the basic data for the pressure measurement, the dependence of the amount of generated ions on the gas pressure and on the laser intensity have been measured for various kinds of gases[2-6].

The experimental apparatus is shown in Fig.1. The laser light is focused through a spherical lens with a focal length of 300 mm or 500 mm into the center of the ionization box of a quadrupole mass spectrometer installed in a vacuum chamber. The ions generated in the focused region (ionization region) are detected with the quadrupole mass spectrometer (the filament of the spectrometer was turned off in the experiment). The laser intensity was regulated by making the laser beam pass through NO_2 gas, whose pressure is variable. XeCl, KrF and two ArF excimer lasers were used in the experiment. As the sample gases, rare gases such as Xe, Kr, Ar and He, and Molecular gases such as O_2, N_2, H_2 and CO_2 were used.

The main results obtained are as follows:

1) For all the measured gases, the proportional relation between the amount of generated ions and the gas pressure was observed. In particular, in the Kr gas, it was verified over the range of $2x10^{-8}$ to $1x10^{-3}$ Pa. In Fig.2, the result for the Kr gas is shown.
2) By means of a high power ArF excimer laser, the nonresonant 4-photon ionization of He atom, which has the highest ionization energy, 24.58 eV, amongst atoms and molecules, was successfully

detected[4]. This result means that it is possible to observe the nonresonant ionization of any atom or molecule with the experimental system of Fig.1.

3) It was found that the dissociation significantly takes place in the ionization of molecules[7].
4) In rare gases, the dependence of the amount of generated ions on the laser intensity was in good agreement with the theory of nonresonant multiphoton ionization. In Fig.3, the dependence of the ionization signal on the Xe gas pressure with the KrF excimer laser is shown.
5) The 2+1 ionization of Kr was observed in the ArF laser[3,6].
6) As seen in Fig.3, saturations of ionization were observed for Xe, Kr, $O_2$and H_2. Saturation of ionization is important for the pressure measurement using laser, because it is directly related to the detection sensitivity for atoms or molecules.

3. ION-DETECTION SYSTEM WITH HIGH SENSITIVITY

In the extremely-high vacuum of $1x10^{-11}$ Pa, there are only several atoms and molecules in the ionization region. To measure a pressure in XHV region, therefore, the ion-detection system must have a high sensitivity so that it can even detect a single atom or molecule. For this purpose, the authors attempted to fabricate two types of ion-detection system with high sensitivity. The one is based on the pulse-counting method, and the other utilizes the image-processing technique.

Figure 4 shows the scheme of the ion detection system using the pulse-counting method. the ion pulse generated with the pulsed laser light is amplified with a electron multiplier of channeltron, a preamplifier and a main amplifier. After A-D converted, the amplified signal is registered in a muti-channel analyzer (MCA). On calculation, this system is designed to be able to detect a single ion. Presently, the preliminary test for the system is carried out.

In the ion-counting system using the image-processing method, a cluster of ions generated with the pulsed laser light is

broadened with a electrostatic lens and enters into a micro-channel plate (MCP). After each ion was amplified there, the cluster of ions makes the distributed bright spots on a fluorescent screen. This signal is processed by the image-processing technique and reproduced on a display. It was confirmed that this ion-counting system can count accurately the ions of a few to several hundreds[8]. Figure 5 is the photograph of the ion signal represented on the display.

4. EXTREMELY-HIGH VACUUM SYSTEM

To verify that the pressure-measurement method using the laser ionization is effective for measuring pressure in the region of XHV, an extremely-high vacuum system is indispensable. Such an experimental vacuum system was fabricated to realize the ultimate pressure lower than 1×10^{-10} Pa.

It is very difficult to fabricate an extremely-high vacuum system with the present vacuum technique. Presently, in our country, various attempts are carried out to develop the extremely-high vacuum technique. As a result, to realize the extremely-high vacuum, electrolytic-polioshing or electrolytic-abrasive-polishing of the innner surface of the vacuum vessel is considered as very effective.

The authors, however, adopted another method as follows:

1) degassing all the components in vacuum for 4-5 hours before setting up the vacuum system.
2) machining all the inner surfaces of the vessel to remove the rugged layer on the surface.
3) adopting of the low-outgassing material.

By this method, the authors succeeded in realizing the ultimat pressure lower than 1×10^{-10} Pa. Figures 6 and 7 are the system construction and the pumping characteristic, respectively.

5. CONCLUDING REMARK

The pressure measurement using the laser-ionization method is based on the new principle different from the conventional vacuum technique. Hereafter, using the prepared extremely-high vacuum system, the authors will verify that this method is effective for the XHV pressure measurement

REFERENCES

1) G.S.Hurst, M.H.Nayfeh, and J.P.Yang, Appl. Phys. Lett. **30**, 229 (1977).
2) S.Ichimura, K.Kokubun, and H.Shimizu, Jpn. J. Appl. Phys. **26**, L573(1987).
3) K.Kokubun, S.Ichimura, and H.Hashizume, H.Shimizu, Y.Oowadano, Y.Matsumoto, and K.Endo, Jpn. J. Appl. Phys. **28**, L2271(1989).
4) K.Kokubun, S.Ichimura, and H.Shimizu, Jpn. J. Appl. Phys. **29**, L673(1990).
5) K.Kokubun, S.Ichimura, and H.Hashizume, H.Shimizu, Y.Oowadano, Y.Matsumoto, and K.Endo, J. Vac. Sci. Technol. **A8**, 3310(1990).
6) K.Kokubun, S.Ichimura, and H.Shimizu, Jpn. J. Appl. Phys. **29**, L1509(1990).
7) K.Kokubun, S.Ichimura, and H.Shimizu, J. Vac. Soc. Jpn. **33**, 7(1990).
8) S.Ichimura, K.Goto, K.Kokubun, H.Shimizu, and H.Hashizume, Rev. Sci. Instrum. **61**, 1192(1990).
9) K.Kokubun, H.Shimizu, S.Ichimura, H.Kawahara, and M.Kondo, J. Vac. Soc. Jpn. **34**, 14(1991).

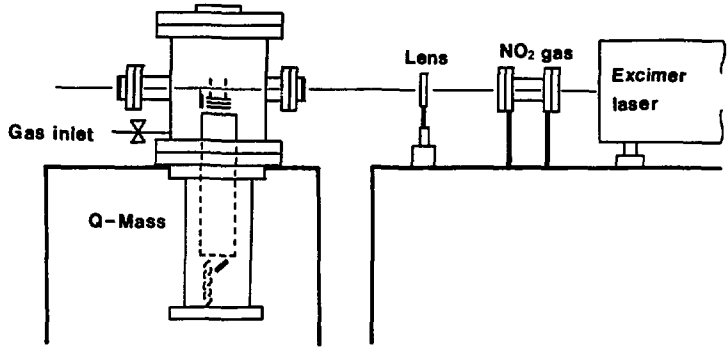

Fig.1 Experimental apparatus for measuring the laser-ionization characteristics of gases.

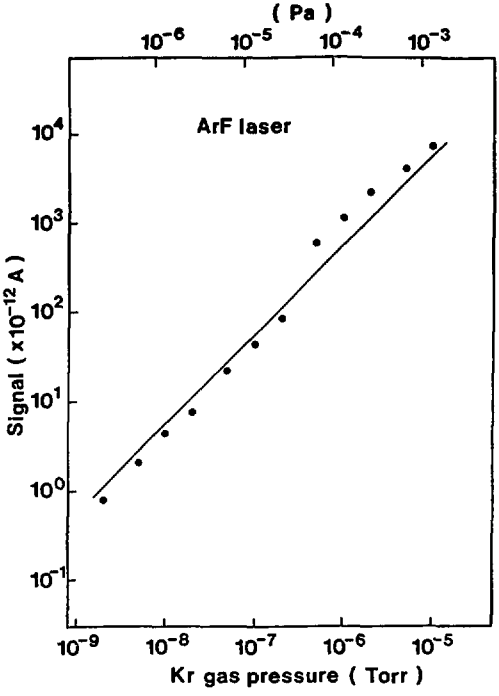

Fig.2 Ionization signal (amount of generated ions) vs Kr gas pressure characteristic with the ArF laser.

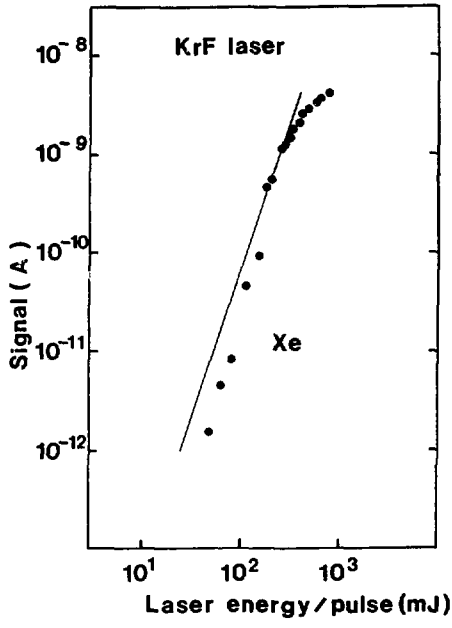

Fig.3 Ionization signal vs laser pulse energy for Xe gas with the KrF laser.

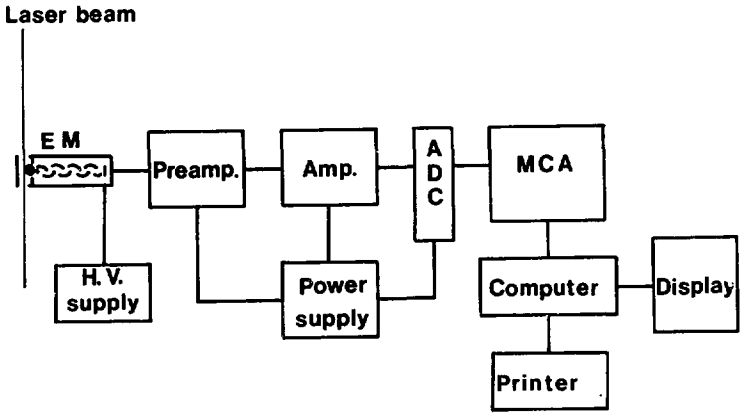

Fig.4 Construction of the experimental ion-detection system

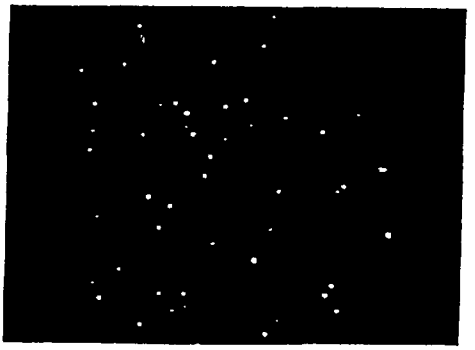

Fig.5 Bright-spot distribution on the display representing the ions generated with the pulsed laser light.

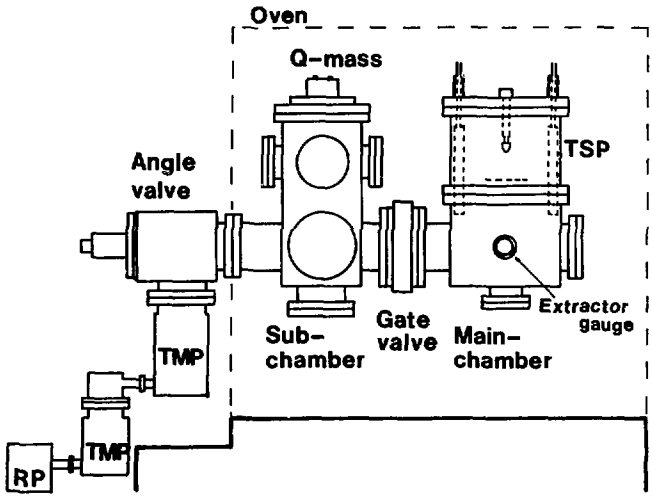

Fig.6 Construction of the experimental extremely-high vacuum system.

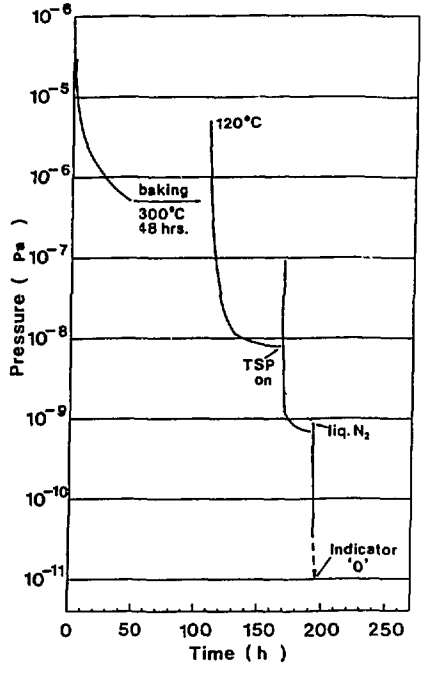

Fig.7 Pumping characteristic of the experimental extremely-high vacuum system.

INTENSE ULTRA-SLOW POSITIVE MUON BEAM BY LASER IONIZATION OF THERMAL MUONIUM

K. Nagamine

Meson Science Laboratory, Faculty of Science, University of Tokyo(UT-MSL)

Hongo, Bunkyo-ku, Tokyo, Japan

Abstract

Basic idea, design considerations and state of construction are given for the ultra-slow μ^+ facility currently under construction at UT-MSL/KEK. Intense monochromatic (several keV) and high quality μ^+ beam will be produced by utilizing a laser ionization of intense thermal muonium which is produced from the atomic surface of the hot tungsten placed right on the primary proton beam.

1 INTRODUCTION

The positive muon (μ^+) now established as a probe to understand microscopic magnetic properties of the condensed matter. So far, all the experiments have been carried out by using MeV μ^+ beam availlable from the pion decay in flight or at the surface skin of the production target. A new epoch-making progress can be expected, if an intense and high quality slow (below keV) μ^+ beam can be realized. There have been two proposals up to now concerning how to achieve such a slow beam production: a) a re-emission method using the re-emission phenomena of the thermal muonium (Mu), μ^+ or Mu^- from a material surface after stopping conventional muons inside specially selected materials [1,2] ; b) beam-cooling method using electro-magnetic acceleration and/or deceleration after detecting the phase space of an injected conventional muon [3].

2 BASIC CONCEPT OF THE PROPOSED SLOW μ^+ BEAM

Here, we would like to concetrate on the re-emission method for μ^+, which was mainly proposed and developped by the present author and coworkers at UT-MSL located at KEK [1,2]. The re-emission of a slow beam of μ^+ can be relatively easily realized compared to that of μ^-, since μ^+ thermalization and diffusion can always occur in condensed matter. The following three processes have been considered towards the

realization of an intense slow μ^+ source: 1) generation of thermal muonium (Mu) in vacuum after stopping μ^+ in special materials; 2) production of slow μ^+ by the ionization of thermal Mu; and 3) further increase in the slow μ^+ production by arranging these two processes straightly at the primary beam. A schematic view of the first and the second processes and shown in Fig. 1 and the third process can be seen in Fig. 2.

The actual first step of the project was initiated by the first successful experiment carried out at UT-MSL/KEK regarding the production of thermal Mu in vacuum from a hot tungsten foil [4]. There, in the W foil as shown in Fig. 1 the following successive processes take place: a MeV μ^+ stopping near the rear surface of the foil; a part of the μ^+ diffuses towards the atomic surface of the foil; and there, after picking up unpaired electron, the neutral Mu evaporates in a thermionic emission process. The production rate, which is roughly equal to the ratio of the μ^+ diffusion length in W versus the μ^+ stopping length, was found to be around 4%. Following our hot W experiment, another efficient thermal Mu production phenomena was also found from SiO_2 powder at TRIUMF [5].

As the next step, an experiment concerning the ionization of the thermal Mu was carried out at UT-MSL/KEK using a laser 3-photon ionization method ($1 \rightarrow 2s \rightarrow$ unbound) [6]. Although the main concern of the experiment was not to achieve highly efficient ionization, laser-ionized μ^+ was successfully detected from the thermal Mu in vacuum.

As the final step, at UT-MSL/KEK, a new facility is under construction to realize the idea of the intense slow μ^+ production by conducting the thermal Mu production and its laser ionization in the most efficient way, namely, by plaicng these two processes at the primary proton beam. The aim of the present article is to summarize the design and construction works for the ultra-slow μ^+ facility with a particular emphasis on the laser system

3 YIELD ESTIMATION OF DIRECT THERMAL MU PRODUCTION

In order to estimate how much intense thermal Mu to be produced from the hot W placed at the primary proton beam, several model calculations have been performed with the help of K. Ishida (RIKEN). For this purpose, the dependence of the thermal Mu yield N_{Mu} on the thickness of the W foil was calculated by a Monte-Carlo method with two different geometris, forward and backward production. The N_{Mu} can be represented by proton current (I_p), cross section of the stopping π^+ ($\sigma_{stop\pi}$), the π^+ to

μ^+ conversion rate inside the target ($\eta_{\pi\mu}$) and the thermal Mu production efficiency (ε_{Mu}),

$$N_{Mu} = I_p \cdot \sigma_{stop\pi} \cdot \eta_{\pi\mu} \cdot \varepsilon_{Mu}$$

By a Monte-Carlo method the number of $\sigma_{stop\pi} \cdot \eta_{\pi\mu}$, the stopping μ^+ yield within 100 mg/cm^2 from the surface, was obtained (Fig. 3). The number becomes 2 x 10^{-6} for 1 g/cm^2 thick W. By using I_p = 3 x 10^{13} p/s available at UT-MSL/KEK and ε_{Mu} = 0.04, we can obtain N_{Mu} = 2 x 10^6 /s.

It is obvious that $\sigma_{stop\pi}$ does increase for the low-Z material. Thus, more efficient thermal Mu production can be expected by adopting a combined target of low Z material and hot W; the former is for low energy π^+ production and the latter is for π^+ stopping and thermal Mu productions. For the first-phase Monte-Carlo calculation, the following assumptions have been made ; π^+ production cross section is 10 mb x $Z^{1/3}$, where angular dependence is isotropic in c.m. system and π^+ energy dependence is a linear dependence with a peak at m_π /2 in c.m. system.

In order to optimize a geometrical arrangement of these two targets, the calculation has been made by taking the following numbers as parameters; the distance of the vector between the two targets L, the angle between proton beam and the first target α, the angle between the first target and the vector α_1 and the angle between the vector and the hot W target α_2.

As a reasonable first target, we adopted a stack made of Be and the hot W Then, the calculation was made for optimization of the μ^+ stopping number at the second target of the 100 μm hot W target. The advantage of the stack target was clearly seen. Then, the thickness of the first Be target was optimized by changing the taget thickness for the stacked target geometry. Then, the optimum condition can be considered for the thickness of Be target as 1 g/cm^2, more thicker target gives no increase of N_{Mu} and increase in the scattering of primary beam.

4 IONIZATION METHOD OF THERMAL MUONIUM

There are several possible methods to ionize thermal Mu in a vacuum other than by 3-photon ionization: laser 2-photon ionization (1s→2s→unbound); electron impact ionization; ionization in a D^+e^- plasma; laser blasting ionization of Mu on surfaces. On the other hand, the direct production of thermal or epithermal slow μ^+ as well as slow Mu^- was found from the surface of solid Ar or alkali-halides [7]. As far as the production efficiency is concerned, it is below 10^{-6} for these direct slow μ^+/Mu^- production, but larger than 10^{-2} for thermal Mu. Therefore, if we can employ an

ionization method with an efficiency larger than 10^{-4}, the resultant thermal μ^+ becomes far stronger than the direct μ^+ or Mu^- production

After a series of long discussions, the UT-MSL group led by the present author and Y. Miyake (UT-MSL) has adopted laser 2-photon ionization as the most suitable method for thermal Mu ionization, where Mu is excited from 1s to 2p by 122 nm photons, follwed by an absorption of the second photon with a wavelength shorter than 366 nm. The advantages can be summarized as follows: a) a reasonably high ionization efficiency can be expected, since with an intense pulsed laser source full ionization is possible for Mu in a volume of $(5\ mm)^2$ x (a few cm); b) no further momentum spread is expected due to recoil motion; c) the μ^+ extraction optics following the ionization process is not disturbed at all; d) new laser technology has just realized an intense pulsed light source for both 122 nm and around 366 nm. Here, we must emphasize the advantage of a sharply pulsed μ^+ beam available at UT/MSL/KEK [8] as well as RAL, which is just suitable for a coupling with an intense pulsed laser source.

5 LASER SYSTEM FOR MUONIUM IONIZATION

For the ionization of Mu by laser, it is required to have two light sources, namely, 122 nm one for 1s to 2p excitation and shorter than 366 nm one for 2p to unbound excitation. For this particular purpose of the Mu ionization, several additional requirements exist.

a) Since the Mu is generated from 2000 K hot W, the Doppler broadening does seriously affect the 1s to 2p excitation.

b) High power pulsed laser is inevitable to realize a cascade excitation from the excited 2p state whose life time is 1.7 ns.

So far, several methods have been proposed how to produce very intense 122 nm laser.

1) Method using Hg resonance state of 6S-6P-7S-8P. This method was originally employed to produce an very intensive VUV light, by A.V. Smith et. al. for the so-called "SANDIA" System [9]. This method has the highest conversion efficiency of UVU light, but requiring not only three independent lasr lights of 555, 405 and 255 nm but also a mercury cell with a heat pipe, causing a much more cost and a lot of maintenance work.

2) Method using three wave non-resonant mixing of 366 nm in Kr-Xe cell. This method has been used by a lot of scientists to generate the Hydrogen Lyman α. This is not only technically the easiest method but also taking an excellent advantage in that the original 366 nm of laser light can be used even for ionizing 2P state of muonium. But

unfortunately the conversion efficiency to generate UVU is too low to satsfy the power requirement.

3) Method using two-photon resonant difference frequency mixing in Kr. This method was originally proposed by G. Hilbig [10] and developed by J.P. Marangos et al. [11] particularly for the intense Lyman-α generation. This method has several advantages in the easiness of Kr-cell handling, and the better conversion efficiency than the non-resonant method.

4) Method using Hg resonance state of 6S-6D-11P. This method utilizes two wavelength of 280 nm and 941 nm for the transition of 6S-6D and 6D-11P.. Of these two wavelengths, 280 nm can be generated by triplihg of 841 nm but 941 nm is just out of range of Ti-Sapphire laser.

These features of four methods have been criticized and compared with the helps of S. Chu, (Stanford), T. Kuga (ISSP) and Y. Miyake. Consequently, Method using two-photon resonant difference frequency mixing was adopted since better conversion efficiency can be expected than the other methods

In order to excite 1S state muonium atoms into 2P and ionize them, an intense pulsed laser system generating 122 nm and 355 nm was designed and developed at UT - MSL. This system can be operated with use of all solid state oscillators and amplifier stages. It will be operational with the frequency of 20 Hz synchronously with the KEK-Booster proton beam operation.

As for 122 nm light, two kinds of photons are needed. One is the narrow band 212.5 nm to excite Kr atoms into $4P^5 5P$ resonance state and the other is the broad band 823 nm laser as a difference frequency. The former 212.5 nm is generated by quadrupling the 850 nm photon in the two β-Ba_2-BO_4 crystals, which are generated by the narrow band TiS laser system pumped by YAG laser, producing 3mJ/pulse in a 5 ns time width with 0.3-1 GHz band width. The latter is also generated by the similar TiS laser system pumped by YAG lase, producing 30 mJ/pulse in a 10 ns time width with 200 GHz band width. According to the work by Marangos et. al., we can except the 20 μJ Lyman α light by using these two lights.

As for the photon to ionize 2P state of muonium, 355 nm was chosen instead of 366 nm, because the frequency of 355 nm can be easily generated as the third harmonic of YAG's fundamental 1064 nm which is, otherwise, disposed as a waste of the pumping laser, 532 nm, for TiS. As a result we can expect 30 mj/5ns 355 nm light from the pulsed YAG source.

The layout of the TiS laser system for these three lights are shown in Fig. 4.

6 EXPECTED ULTRA-SLOW μ^+ YIELD

The power requirement for each of 2 lights have been calculated with the help of K. Kojima (UT-MSL). The result which took into consideration of the Dopper broadening effect is summarized in the form of ionization probability versus powers of both of these two rights. Then, by using above-mentioned laser powers,ionization efficiency of 0.06 can be obtained.

The eventual expected yield of the slow μ^+ can be written as follows.

$$N_{SL\mu^+} = N_{ThMu}\ \eta_{laser}\ \varepsilon_{ioni}\ \varepsilon_{col},$$

where η_{laser} is a volume ratio of the intersection region between thermal Mu and laser versus total thermal Mu, and ε_{col}, is the collection efficiency for the produced slow μ^+.

By placing N_{ThMu} and ε_{ioni} already mentioned and $\varepsilon_{laser} = 0.1$ as well as $\varepsilon_{col} = 0.5$, we can conclude $N_{SL\mu^+} = 10^4$/s.

7 THE ULTRA-SLOW μ^+ FACILITY

The ionization product of the slow μ^+ is collected, accelerated and extracted by the ion optics system designed with the helps of R. Kadono (RIKEN) and P. Strasser (UT-Nucl. Eng.) as shown in Fig. 5 which is composed of the SOA lens, electrostatic bend, magnetic bend, electrostatic quadrupole lenses. The optics has a mass and momentum selection capability.

As mentioned earlier, the target system is made of low Z material of 1 mm thick Boron Nitrate and 100 μm thick hot W, which are placed in the ultra high vacuum (10^{-10} Torr). The target heating is done by a direct current through the W target which will be turned off during a few ms around the μ^+ pulse arrival in order to eliminate the disturbance to electrostatic field of the SOA lens system.

New laboratory space and dedicated 500 MeV proton beam line have been constructed for Ultra Slow μ^+ facility with the helps of Y. Miyake, K. Nishiyama, K. Fukuchi and M. Iwasaki (UT-MSL) as shown in Fig. 6. Here, the compact radiation shielding is arranged towards the proton beam line. There, the access for the ion optics installation and possible future modification can be obtained by movable iron shielding block (0.8 m high x 2 m width x 2 m length).

The laboratory building is completed in April 1991. Ultra high vacuum around the target region will be attained in June 1991 and the laser ionization will be tested in July 1991 followed by ultra-slow μ^+ beam production.

Various new physics will be realized by using the ultra-slow μ^+. The novel examples are as follows.

(1) surface sciences with slow μ^+

The intense, high quality polarized μ^+ will be used to explore new aspects of materials surface, catalytic chemical reactions of Mu on surface, etc.

(2) Intense production of thermal Mu and QED

Once we have the keV μ^+ source, thermal Mu can be produced in a controlled way; complete conversion can be expected from keV μ^+ to thermal Mu on either hot W or SiO_2 surface. Intense and localized thermal Mu can be used for the improved measurement of QED e.g. 1s-2s resonance.

ACKNOWLEDGEMENT

The auther acknowleges the contributions of the collaborators at UT-MSL/KEK, in particular, the members invoved in the facility construction; Dr. Y. Miyake, Dr. K. Nishiyama, Mr. P. Strasser, Dr. M. Iwasaki and Dr. S. Sakamoto.

Helpful Informations from Prof. S. Chu, Dr. A.P. Mills Jr. Dr. K. Ishida, D. R. Kadono, Dr. T. Matsuzaki, Dr. T. Kuga, and Dr. E. Torikai are also acknowledged

REFERENCES

[1] K. Nagamine and A.P. Mills, Jr., Los Alamos Report LA-10714C p.216(1986).

[2] K. Nagamine, Atomic Physics 10, 221 (1987).

[3] D. Taqqu, private communication.

[4] A.P. Mills, Jr., J. Imazato, K. Nagamine, et. al, Phys. Rev. Lett. 56, 1463 (1986).

[5] G.A. Beer et. al., Phys. Rev. Lett. 57, 671 (1988).

[6] S. Chu, A.P. Mills, Jr., A. Yodoh, K. Nagamine et al., Phys. Rev. Lett., 60, 101 (1988).

[7] D.A. Harshman et. al., Phys. Rev. Lett. 56, 2850 (1986).

[8] K. Nagamine, Hyperfine Interactions 8 781 (1981).

[9] A.V. Smith et al., Opt. Soc. Am. B, Vol 15, (1988).

[10] R. Hilbig and R. Wallenstein, IEEE J. Quantum Electro. QE-17 1566 (1981).

[11] J.P..Marangos, et. al., to be published (1990).

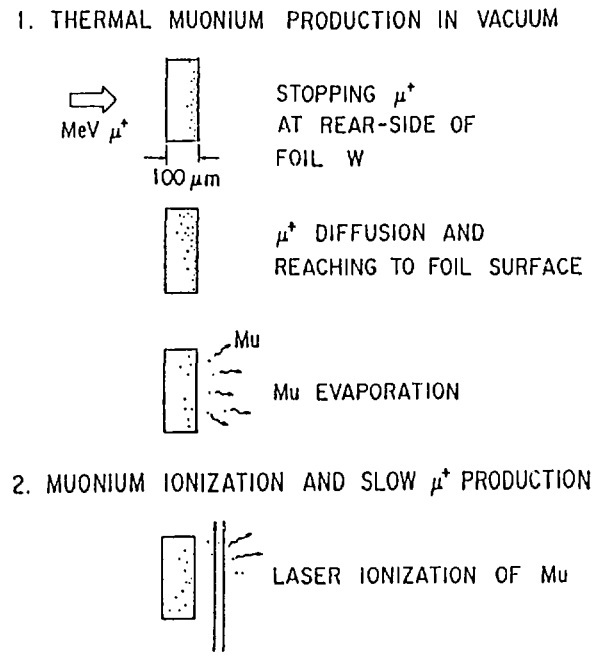

Fig. 1. Concept of thermal Mu production from hot W surface and slow μ^+ production by laser ionization.

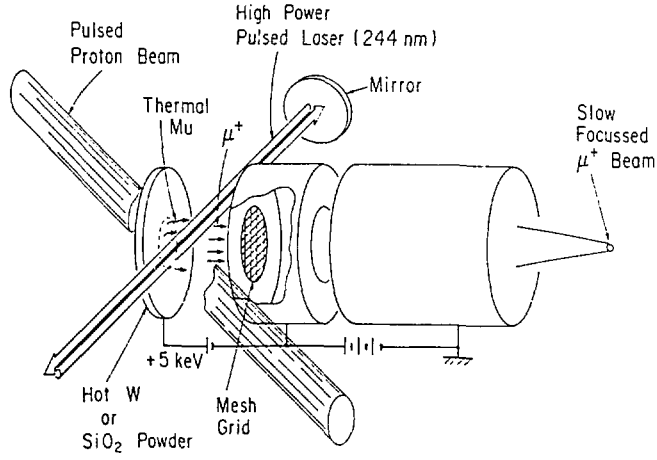

Fig. 2. Schematic view of slow μ^+ production from hot W plased at the proton beam line.

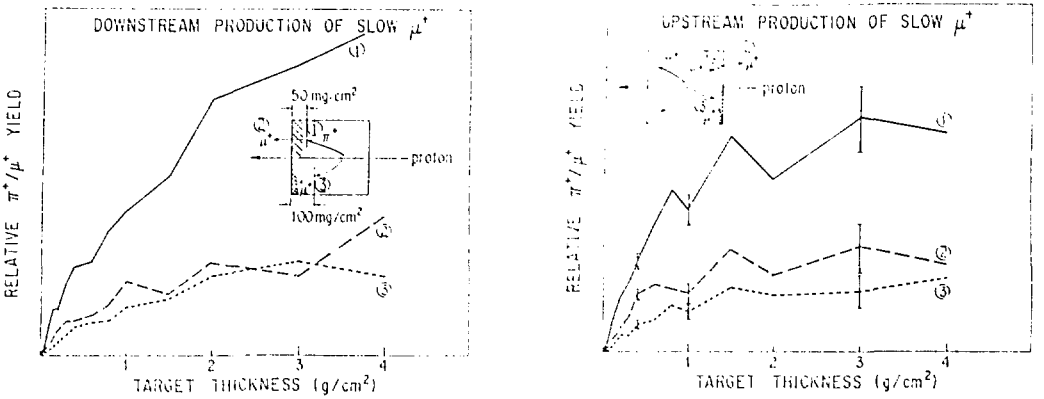

Fig. 3. Results of a Monte Carlo calculation concerning the of slow π^+/μ^+ yield for forward direction production (left) and for backward direction production (right) as a function of W target thickness. Curves represent (1) π^+ stopping within 100 mg/cm^2 from the target surface, (2) μ^+ emerging from the surface and (3) μ^+ stopping within 50 mg/cm^2 from the target surface.

Fig. 4. Schematic layout of laser systems for thermal Mu ionization installed at UT-MSL/KEK; 212 nm part (upper) and 823 nm part (lower).

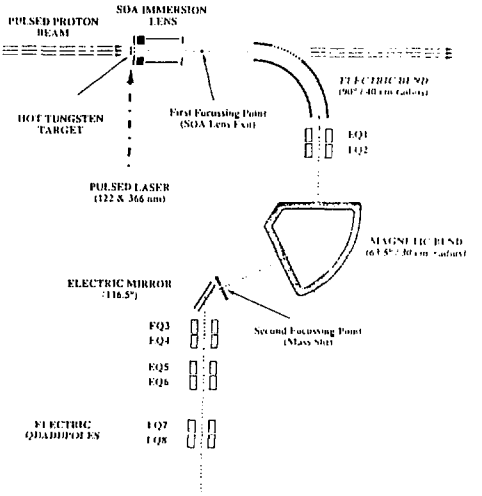

Fig. 5. μ^+ Ion Extraction Optics installed at UT/MSL/KEK.

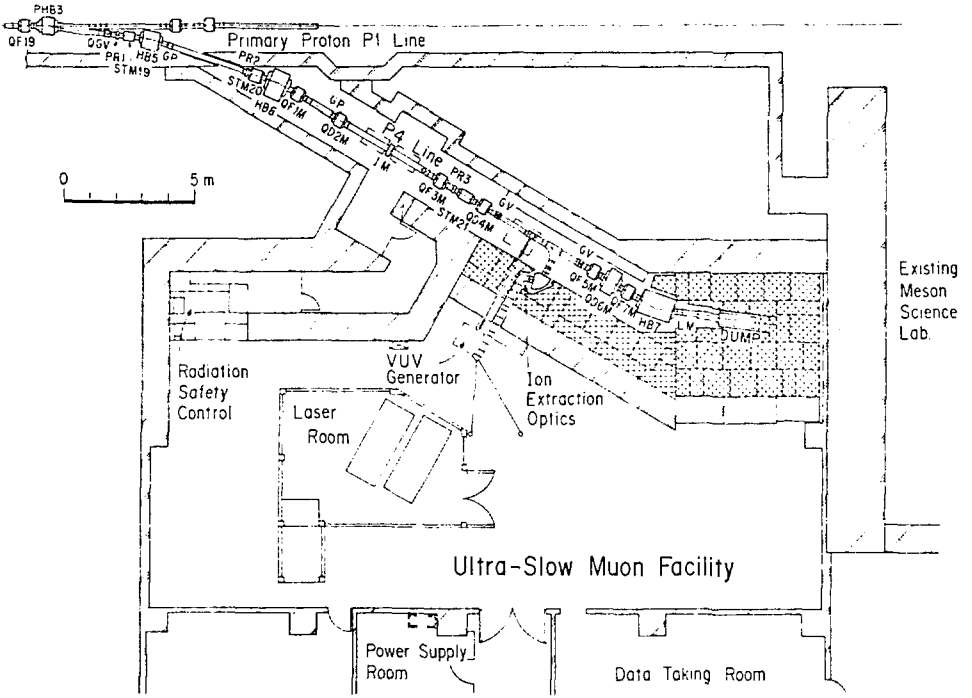

Fig. 6. Layout of the Ultra-Slow μ^+ Facility almost completed at UT-MSL/KEK in June, 1991.

TIME OF FLIGHT MASS SPECTROMETRIC ANALYSIS OF DAUGHTER ISOTOPE OF ^{136}Ba IN DOUBLE BETA-DECAY OF ^{136}Xe

M. MIYAJIMA, S. SASAKI and H. TAWARA
National Laboratory for High Energy Physics
Oho 1-1, Tsukuba, Ibaraki 305, Japan

1. Introduction

There have been recently growing interests in nuclear double beta decay [1]. It is a very rare process in which an atomic nucleus (A,Z) decays to another nucleus (A,Z+2) by emitting two electrons and other particles in one of the following modes:

$$(A,Z) \text{ -- } (A,Z+2) + 2e^- + 2\bar{\nu} \qquad (1)$$

$$(A,Z) \text{ -- } (A,Z+2) + 2e^- \qquad (2)$$

$$(A,Z) \text{ -- } (A,Z+2) + 2e^- + X \qquad (3)$$

where A is the mass number of atomic nucleus, Z the atomic number, e the electron, $\bar{\nu}$ the neutrino, and X the Majoron.

The first mode is allowed as a second-order weak process by the standard model of weak interaction. The second and the third modes require lepton number nonconservation and a mechanism of helicity reversal, and could be allowed by physics beyond the standard model. The double beta decay has been investigated with three different methods, (a) the direct detection method, (b) the geochemical method and (c) the radiochemical method. In the first

method, the summed energies of two emitted electrons are measured. The decay of mode (1) produces a four-body spectrum peaking at about 0.32 x E_0, where E_0 is the total energy available in the decay. The decay of mode (2) produces a mono-chromatic peak at E_0. The decay of mode (3) shows a three-body spectrum peaked at about 0.76 x E_0. These three processes are experimentally distinguishable in the direct method and ^{48}Ca, ^{76}Ge, ^{82}Se, ^{100}Mo and other nuclei have been so far investigated with this method[1]. In the geochemical method, the excess of a daughter isotope accumulated for geological periods is measured in an ore sample that contains the parent isotope. On the other hand a daughter isotope is accumulated under laboratory conditions in the radiochemical method [2]. With the geological and the radiochemical method it is however not possible to distinguish the above three modes. The double beta decays of ^{82}Se, ^{128}Te and ^{130}Te have been investigated in the geochemical method [3] and that of in the radiochemical method.

At present we are developing apparatus for detection of the double beta decay of ^{136}Xe both with the direct detection method [4] and with the radiochemical method [5].

Here we briefly describe the apparatus for the latter method and its preliminary experimental works.

2. Double beta decay of ^{136}Xe

There are nine stable isotopes in the natural mixture of xenon isotopes. ^{134}Xe and ^{136}Xe, of which each isotopic abundance is 10.4 % and 8.9 % respectively, are candidates for double beta

decay. The liquefied xenon is the most promising material for radiation detection. The W value defined as an average energy expended per ion-pair is 15.6±0.3 eV [6] and also the W_s defined as an average energy expended per scintillation photon is 16.9±0.3 eV [7]. Presently, a liquid xenon ionization drift chamber (LXIDC) with a effective volume of 2 liter is under developing in order to search for the neutrinoless double beta decay of ^{136}Xe [4]. In liquid xenon, both signals of ionization and scintillation due to radiation are observable. The number of liberated electrons due to ionization is used to measure the energy of radiation. The drift time of those electrons to a collector electrode from the time that scintillation is observed is a measure of the position of the event. The summed energy of two emitted electrons in the decay of ^{136}Xe is 2.491 MeV. However, it is lower than the maximum energy of naturally occurred gamma-ray backgrounds (2.716 MeV). Then, it is essential to make the detection system ultra low background and also to require the excellent energy resolution for the detection of the neutrinoless double beta decay. Furthermore, it is desirable that a detected event as a candidate for a neutrinoless double beta decay may be confirmed with an independent method. One of the methods is to assure the existence of a daughter nucleus around the decay point in the detector. The method of one atom detection, which was demonstrated by Hurst et al. in 1977 [8], is one of the resonance ionization spectroscopy with lasers (RIS) and is a promising one for that purpose.

As a preliminary work, we are developing a measuring system of

daughter nucleus ^{136}Ba as the first step for that purpose. The system is composed of two parts, a positive ion collector (PIC) and a time of flight mass spectrometer (TOFMS) which we will briefly describe below.

3. Positive ion collector (PIC)

A schematic diagram of the positive ion collector (PIC) is shown in Fig.1. The PIC is a spherical stainless steel chamber with a small spherical central collector electrode (CE) of ^{136}Ba ions inside. The chamber is fixed in the vessel thermally shielded with vacuum and is cooled down to about $-110^{o}C$ by a refrigerator. It is also rapidly cooled down by filling liquid nitrogen in the vessel for emergency purposes. The CE is connected to a moving stage through a insulator with a long stainless steal rod and is movable to a position above a gate valve from the center of chamber. The chamber is evacuated to a pressure of $1x10^{-7}$ torr and is filled with liquid xenon condensed from gaseous xenon with natural mixture of isotopes by the refrigerator. The CE is negatively biased in liquid xenon with a high voltage supply, while the chamber is grounded. The positively charged barium ions, which are emerged as daughter nuclei in the double beta decay of xenon, move slowly toward the CE and are trapped to the surface of it. The bias voltage is maintained for a long period of time to collect barium ions enough to analyze with the TOFMS. After that, the CE is removed from the liquid xenon and is transferred to the TOFMS without exposing its surface to air.

4. Time of flight mass spectrometer

The system of TOFMS is schematically shown in Fig.2. The system composes of lasers for ablation of the surface of CE and for resonance ionization spectroscopy of sampled atoms, an electrode assembly for acceleration of ionized ions, free flight space of ions and an ion detector. The lasers used in the system are two pulsed Nd-YAG lasers of 800 mJ/pulse and 200 mJ/pulse at the wavelength of 1064 nm and a dye laser excited with the second or the third harmonics from the YAG-laser with the power of 800 mJ/pulse. The CE is transferred to the TOFMS from the PIC after the daughter ions are collected for an enough collection time. Those trapped atoms are liberated from the surface of CE with a laser beam from the YAG laser. The neutral atoms of barium are selectively and resonantly ionized with an beam from the dye laser by the method of RIS [5]. The barium ions ionized in the effective volume are accelerated in the electric field of the electrode assembly and are detected by a detector which is assembled with two stages of a micro-channel plate (MCP) after flew the free space of about 1.5 m long. Signals from MCP are fed into a digitizing signal analyzer (DSA 602, Sony-Tektronix). The number of ions is measured as a function of the flight time of ions.

5. Preliminary works

There are many preliminary works to accomplish in order to obtain our final goal. At present we are developing a system of TOFMS as a first step among those. The third harmonics from YAG

laser pumps the dye laser. The light from the dye laser are fed directly or through a frequency doubler (BBO crystal) into the TOFMS. Two measured examples of TOF spectrum are shown in Fig.3 and Fig.4. The first case shows a spectrum which was obtained with a gas sample of natural barium. The barium atoms are vaporized from its metal by an electric furnace and are introduced into the TOFMS. Five peaks are observed at positions corresponding to ^{134}Ba to ^{138}Ba in the natural mixture of barium isotopes. However, two isotopes with isotopic abundance of about 0.1 % are not detected. The abundance ratio and the flight time measured from the spectrum are shown with its mass and its natural abundance in Table 1. Each abundance is well agreed with a difference of a few percent. The second case shows a spectrum of xenon with the natural mixture of isotopes. The TOFMS was filled with a gaseous xenon at the pressure of 2.8×10^{-6} torr. The laser beam of 0.13 mJ/pulse from the dye laser tuned to 252.484 nm was used to excite and to ionize xenon atoms. All the isotopes are observed as shown in Fig.5. Also, the measured abundance ratios and the flight times are shown in Table 2. The measured abundance ratio of each isotope is well agreed with its natural abundance ratio.

6. Detection efficiency of TOFMS.

From the above results, we can estimate detection efficiency of TOFMS and also detected number of ions under several assumptions. By making use of the isotopic abundance (26.4 %) of ^{129}Xe, the most abundant isotope, we estimate the number of ^{124}Xe. The number density of xenon atoms in the system of TOFMS is 1.0 x

10^{11} cm^3 from the pressure of 2.8 x 10^{-6} torr. The number of ^{129}Xe in the effective volume of TOFMS is written to be 2.6 x 10^{10} x V_e x F_{ris}, where V_e is the effective volume which is defined by the beam size of laser and the effective area of a detector and F_{ris} is the efficiency of resonance ionization. In this system V_e was $8x10^{-5}$ cm^3. On the one hand, the output signal from the detector was 650 mV in the height and 25 ns in the full width at half maximum on a 50 ohm output load and the gain of the detector (MCP) was 5.0 x 10^5 at the present applied voltage. Then, the number of ^{129}Xe, which is detected by the detector, is 4.1 x 10^3. The transparency, F_{tra}, of TOFMS from the ionization region to the detector is defined as a ratio of the number of ions detected at the detector to the number of ions ionized by the laser beam. In the present case, F_{tra} = 4.1 x 10^3 / 2.6 x 10^{10} X V_e x F_{ris} = 5.1 x 10^{-2} where F_{ris} is reasonably assumed to be unity. From these results, the number of ^{124}Xe isotope detected can be estimated to be about 15 and the number of ions ionized in the ionization region is about 300. Namely, the density of ^{124}Xe is 3.7 x 10^4 cm^{-3} in the ionization region of the system.

7. Estimation of detection limit of ^{136}Xe double beta decay

The volume of the PIC for collection of ^{136}Ba ions decayed from ^{136}Xe in liquid xenon is about 4 liter. In this apparatus the number of ^{136}Ba, N_c, collected on the CE for a collection time t (year) is written as follows;

$$N_c = 3.51 \times 10^{24} \times (t/T) \times F_{col}, \quad (4)$$

where T is the half life of double beta decay of ^{136}Xe in the

unit of year and F_{col} is the collection efficiency of the CE. Then, the number of ^{136}Ba ions, n_d, detected by the system of TOFMS is written as follows;

$$n_d = N_c \times F_{ab} \times F_{sam} \times F_{ris} \times F_{tra} \times F_{det}, \quad (5)$$

if the surface of CE is completely surveyed by laser ablation, where F_{ab}, F_{sam}, and F_{det} are the efficiencies of the liberation of ^{136}Ba by laser ablation, of the sampling of liberated ^{136}Ba by the laser beam for resonance ionization, and of detection of ^{136}Ba ions by the ion detector, respectively. Since F_{ris} and F_{det} are reasonably assumed to be unity and $F_{tra} = 5 \times 10^{-2}$, the number of ^{136}Ba detected in the TOFMS system is rewritten in the following manner,

$$n_d = 1.8 \times 10^{23} \times F_{ab} \times F_{sam} \times (t/T), \quad (6)$$

assuming $F_{col} = 1$.

The half life of double beta decay of ^{136}Xe is theoretically estimated to be 2.1×10^{19} y in the decay mode (1) and 1.8×10^{23} y in the mode (2). Then, n_d is expected to be about 100 in the former case and about 1 in the latter case for the one year collection of ^{136}Ba, assuming the unknown efficiency, $F_{ab} \times F_{sam}$ of 1 %.

8. Conclusion

There are many unknown factors in this experiments. Mobility or life time of singly or doubly charged barium ions in liquid xenon under an electric field has not been measured. The efficiencies on laser ablation for a trace amount of isotopes on the metal surface should be experimentally determined by the same

apparatus. The contamination on the metal surface with natural barium is presently not known.

At present we are developing an apparatus to study behaviors of barium ions in liquid xenon and experiments to solve above problems are in preparation.

References;

(1) For reviews see W.C.Haxton and G.J.Stephenson,Jr, Prog. Part. Nucl. Phys., 12(1984)409; T.Tomoda, Rep. Prog. Phys. 54(1991)53; H.Ejiri, Proc. of XVI INS Inter. Symp. Tokyo, March, 1988.

(2) W.C.Haxton, G.A.Cowan and M.Goldhaber, Phys. Rev. C28(1983)467.

(3) T.Kristen, AIP conf. Proc. 96(1983)396.

(4) M.Miyajima, Ionizing Radiation, 15(1988)45, in Japanese.

(5) M.Miyajima, H.Tawara and S.Sasaki, Proc. the 4th Workshop on Radiation Detectors and Their Uses, KEK Peport 89-5.

(6) T.Takahashi et al., Phys. Rev. 12A(1975)1771.

(7) M.Miyajima, S.Sasaki and E.Shibamura, To be published in NIM.

(8) G.S.Hurst, M.H.Nayfeh and J.P.Young, Appl. Phys. Lett. 30(1977)229.

Table 1 Results of Ba isotopes by TOFMS.

Mass Number	Mass (amu)	$(m)^{1/2}$ (amu)1/2	Abundance (%)	Intensity (counts/peak)	Flight Time (μsec)	Measured Abundance (%)
130	129.903	11.398	0.101	——	——	——
132	131.905	11.485	0.097	——	——	——
134	133.905	11.572	2.42	61.01	20.375	1.68
135	134.906	11.615	5.59	204.16	20.448	5.63
136	135.905	11.658	7.81	229.68	20.521	6.33
137	136.906	11.701	11.32	426.30	20.597	11.76
138	137.905	11.743	71.66	2661.52	20.676	73.39

Table 2 Results of Xe isotopes by TOFMS.

Mass Number	Mass (amu)	$\sqrt{m}$ $(amu)^{1/2}$	Abundance (%)	Intensity (count/peak)	Flight Time (μs)	Measured Abundance(%)
124	123.906	11.131	0.10	11.08	20.850	0.11
126	125.904	11.221	0.09	10.20	20.812	0.10
128	127.904	11.309	1.91	191.3	20.974	1.92
129	128.905	11.354	26.4	2849.5	21.060	26.60
130	129.904	11.398	4.1	404.0	21.150	4.06
131	130.905	11.441	21.2	2121.8	21.230	21.31
132	131.904	11.485	26.9	2688.1	21.324	26.97
134	133.905	11.572	10.4	1017.0	21.490	10.21
136	135.907	11.658	8.9	868.5	21.646	8.72

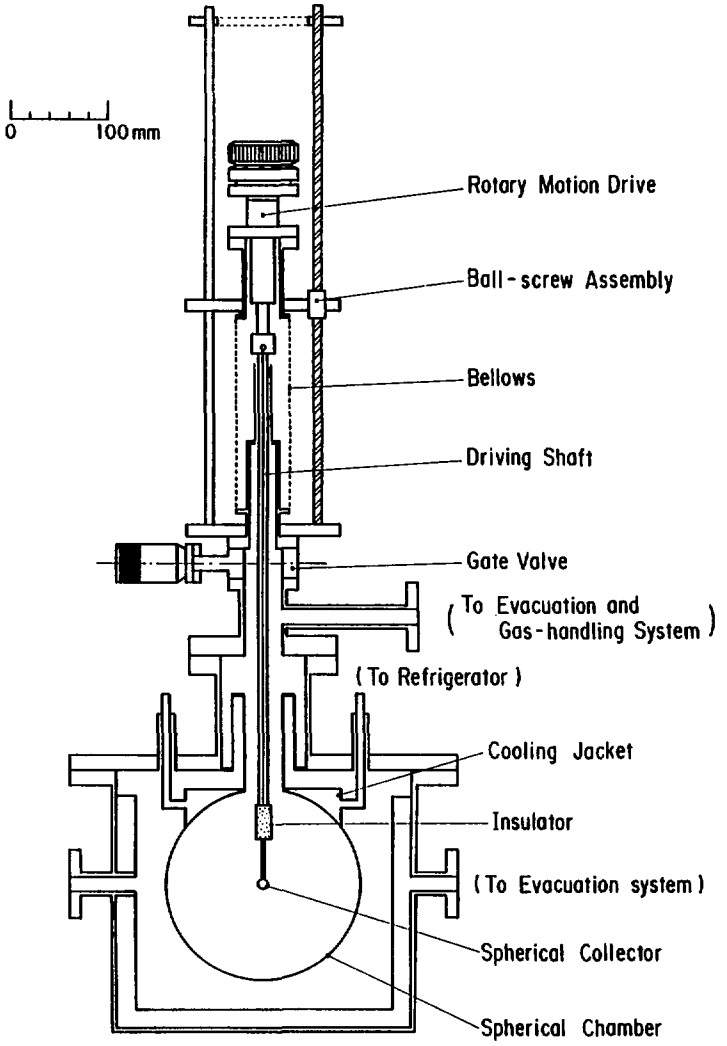

Fig.1 Schematic diagram of the positive ion collector (PIC).

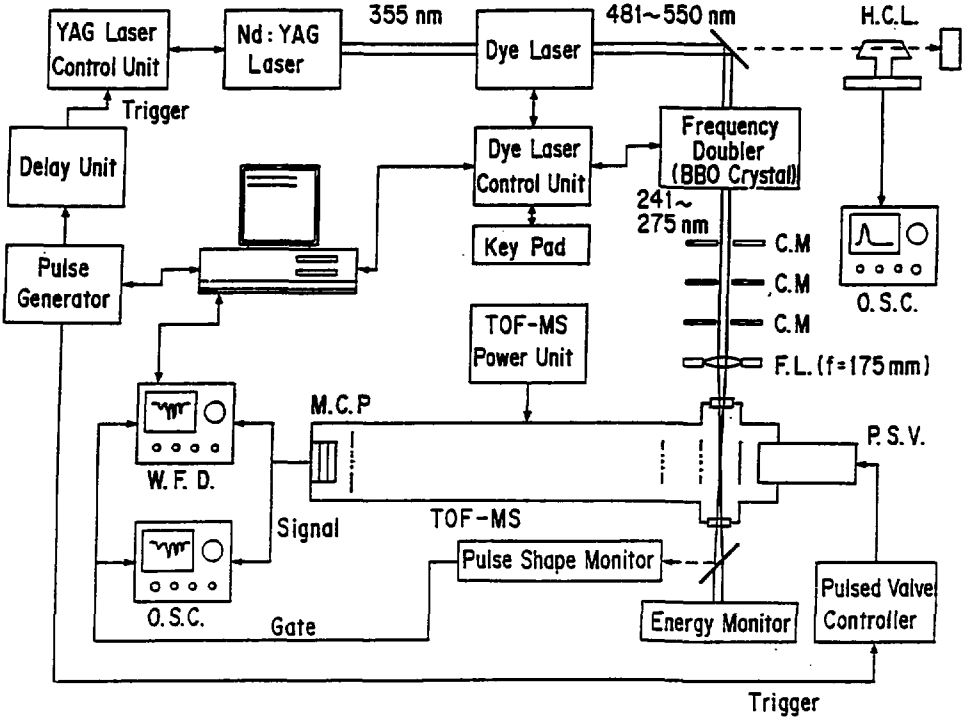

Fig.2 Schematic diagram of the time of flight mass spectrometer (TOFMS) system.

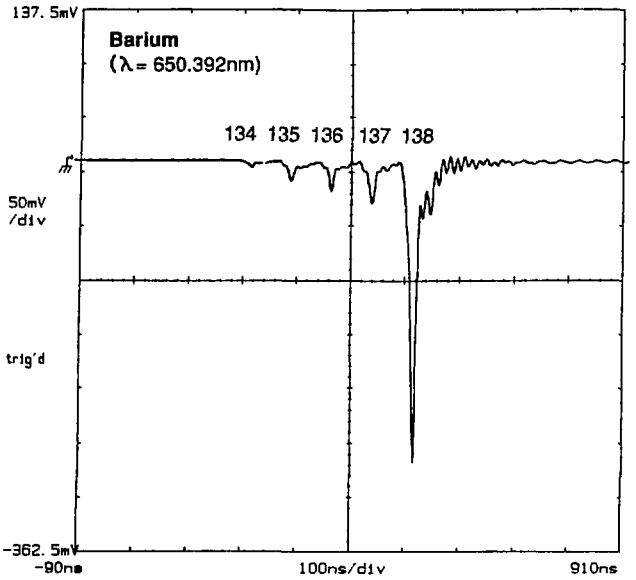

Fig.3 TOFMS spectrum of natural Ba isotopes. Barium atom is exited from its ground state to $6s6d\,^3D_2$ excited state by the two-photon absorption, and ionized by the absorption of another photon of the same wavelength.

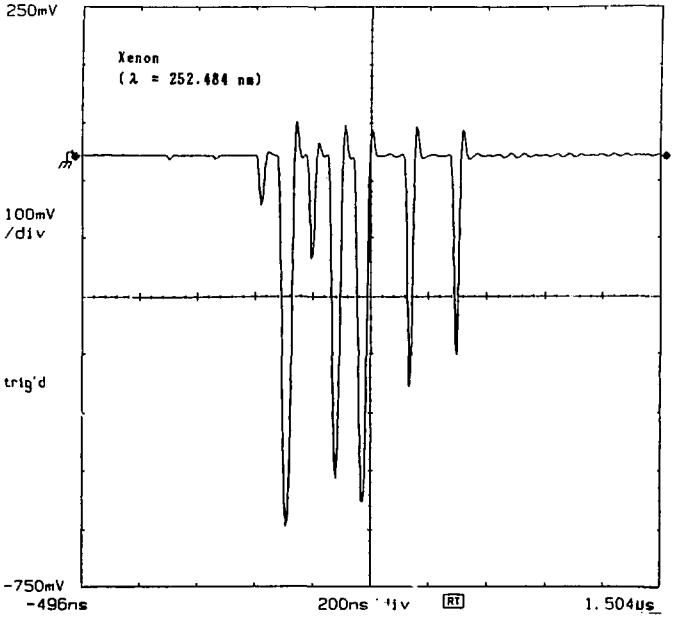

Fig.4 TOFMS spectrum of xenon isotopes. Data are for gaseous pure Xe with the natural mixture isotopes. Xenon atom is excited from its ground state to $6p[3/2]_2$ excited state by the two-photon absorption, and ionized by the absorption of another photon of the same wavelength.

MEASUREMENT OF LIQUID XENON SCINTILLATION USING A SILICON PHOTODIODE

Nobumiti Ishida and Tadayoshi Doke
Science and Engineering Research Laboratory, Waseda University,
17 Kikui-cho, Shinjuku-ku, Tokyo 162

Kimiaki Masuda
Saitama College of Health,
519 Kamiokubo, Urawa-shi Saitama 338

Introduction

Liquid xenon is a excellent material for radiation detectors, especially for γ-rays and electromagnetic showers, because of its high atomic number and high density. Liquid xenon has very good properties not only for ionization detectors, but also for scintillation detectors [1]. The large scintillation yield of Liquid xenon (4×10^{-7} photons / GeV) [2] and the fast decay time (5 ns and 20 ns) [3] make the liquid a suitable detector medium for fast and high energy-resolution calorimeters for future experiments at hadron colliders such as the SSC [4].

Until now, no experimental evidence of good energy resolution for high energy deposition has been shown with the scintillation in liquid xenon. So far we have tested several purification methods for liquid xenon, observed the scintillation light of liquid xenon excited by 100 MeV / n Al ions using a silicon photodiode as a photon sensor, and measured the attenuation length of the scintillation light with reflectors. In this paper, we describe the results of the measurement and indicate the possibility of fast, high

resolution liquid xenon electromagnetic calorimeters.

The Proposed Xenon Calorimeter

We propose a precision electron / photon detector using multiple layers of photodiodes to measure the scintillation light from liquid xenon in order to detect photons and electrons with an energy resolution of better than 0.5% and spatial resolution of better than 2 mm, as well as to make accurate determination of the three dimensional shower profile for pattern recognition and vertex reconstruction. Our experiments using scintillating liquid xenon, performed during the past year, have resolved most of the technical problems associated with building a prototype detector. Some of the most important results to date are summarized below:

- large size UV photodiodes and fast amplifiers work well inside liquid xenon,
- the photo-electron yield collected by these photodiodes in liquid xenon is very large,typically about 107 / GeV
- we have achieved an energy resolution of <0.6% with a 20 ns rise time for heavy ions at E > 1.6 GeV.

Based on the technical information described above, we feel confident to propose an EM calorimeter using scintillation liquid xenon as a new type of detector. Shown in Figure 1 is a quadrant schematic of the xenon calorimeter which consists of a hollow ellipse filled with ~ 3×10^4 cells in which layers of UV photodiodes measure the longitudinal and transverse shower development, in addition to the total UV scintillation signal. The full detector is composed of two independent half shells bolted to a vertical plate located at the midplane. The overall dimensions are 5.2 m in length and 2.8 m in diameter.

The complete xenon detector assembly comprises:

- 15 m^3 of liquid xenon,

- 70,000 channels: photodiodes, fast amplifiers, analog trigger, and readout electronics,
- recording and computer facilities,
- xenon circulation and storage,
- xenon purifier,
- cooling loop circulation and storage system, and
- controls and security system including emergency power.

1. UV photo sensor to measure the light signals from xenon (170 nm).

As a photon detector we use a silicon photodiode, which has fast response, occupies only small space and works at low temperature and in a magnetic field with a rather low bias voltage. (see Fig. 2) The diode is of the surface barrier type . The full diameter of silicon wafer is 2 inches and the effective diameter is 38 mm. The thickness is 450 μm. the electrode facing the beam window is a gold mesh with 20 μm width, 100 μm spacing, and 200 Å thickness. The back side of the silicon is plain aluminum for ohmic contact.

Experiments

1) α particle test and calibration

We tested 5 cm diameter silicon photodiodes in liquid xenon using 5.49 MeV alpha particles from a 241 Am source. The leakage current of the diode was ~10 μÅ at room temperature and ~10 nA at liquid xenon temperature. The capacitance of the detector decreases with increasing bias voltage and reach 600 pF at a bias of 150 V. At this bias voltage the thickness of the depletion layer is 350 μm.

The liquid xenon chamber and cryostat used to test the performance of the photodiode is shown in Figure 3. The distance between the alpha source and the photodiode is 7 mm. Xenon was purified either with a Ba-Ti getter purifier for at least 1 day or by passing it through an Oxisorb filter with a flow rate of 3.5 litters / min. The

temperature and pressure of the liquid nitrogen and -100°C and 1.5 atm absolute with ethyl alcohol cooled by liquid nitrogen and -75°C and 5 atm absolute with dry ice in ethyl alcohol. A typical pulse height spectrum of scintillation light due to alpha particles in liquid xenon measured by a slow charge sensitive preamplifier followed by a shaping amplifier with a peaking time of 1 μs is shown in Figure 4. The measured pulse height of photoelectrons corresponds to 4.0×10^4 electrons with a resolution, dominated by the electronic noise of the amplifier, of 6.6%. This amount of collected charge indicates the quantum efficiency of the photodiode to be 45%. No correction for reflection loss on the detector surface and absorption loss in the gold mesh has been made. As for temperature dependence of the scintillation yield, the yield at -100°C was several percent more than that at -75°C. No significant difference was observed in the performance between the two methods of purification, at least for a 7 mm pathlength of light, indicating that scintillation yield is far less sensitive to impurities than ionization yield. Indeed, one can use ionization to monitor the purity of liquid xenon to control the scintillation yield.

b) The Energy Resolution Using a Fast Amplifier

To demonstrate that the performance of the proposed detector is satisfactory for the SSC project (dE / E = 0.5% at ~ GeV Time response ~10 ns), we observed scintillation light in liquid xenon excited by 100 MeV / n Al ions with a silicon photodiode followed by a fast preamplifier. The photodiode was same as used in alpha particle calibration test. The practical quantum efficiency was observed to be 22% for the wavelength of liquid xenon scintillation light (170 nm). An energy resolution of 0.5% r.m.s. has been achieved for the energy deposition of 2.5 GeV in liquid xenon.

Figure 3 shows a schematic drawing of the liquid xenon cell together with the vacuum chamber for thermal insulation. the chamber has two thin metal windows, 40 μm Havar foil and 100 μm stainless steel foil, for beam incidence. The distance between the inner beam window and the photodiode is 10 mm. The chamber is cooled down by a bath of dry ice and ethyl alcohol, surrounding the chamber pipe. The operating

temperature and pressure are -75°C and 5 atm, respectively. The density of liquid xenon is 2.8 g / cm^3 at this time.

The cell was evacuated to less than 1×10^{-7} torr without baking because photodiodes are easily damaged by heat. The out gassing rate was about 1×10^{-5} torr l / s. Commercial xenon gas of research grade from Teisan Co. was purified by an Oxisorb filter [5] at room temperature with a flow rate of 15 l / min. The volume of the liquid is about 250 cm^3.

The charge signals from the photodiode were fed to a fast preamplifier and a post amplifier. Then the output pulses were integrated with an ADC (LeCroy 2249W).

The ion beam at the Ring Cyclotron of RIKEN (The Institute of Physical and Chemical Research) was used. The energy at the entrance of the liquid xenon was calculated to be 92 MeV / n and the energy deposition in the liquid to be 2.47 GeV. The range of the ions in liquid xenon is estimated to be about 7.1 mm.

Figure 5 shows the block diagram of the electronic circuit. The charge signal from the photodiode were fed to fast preamplifier and a post amplifier. Then the output pulses were integrated with an ADC (LeCroy 2249W). For a fast response time the preamplifier is mounted as close as possible to the photodiode in the liquid xenon. The post amplifier is outside the chamber and is used to amplify the preamplifier output signal by a factor of 20.

We observed the pulse shape of the output signals from the fast amplifier with 150 MHz oscilloscope (Tektronix 475). Figure 6 shows a photograph of the oscilloscope for the photodiode at the bias of 200V. The rise time of the pulse is abut 20 ns. As shown in the figure, there is the successive second pulse and even the third pulse probably due to ringing of the amplifier. The ringing may be caused by mismatching of amplifier parameters for the practical detector load at the liquid xenon temperature. To obtain the total amount of charge, the output was integrated by the charge sensitive ADC. Two different gate widths were used for integration; wide (200 ns including the all successive pulses) and narrow (40 to 60 ns depending on the bias to select only the first

pulse).

Typical pulse height spectra for the Al ions are shown in Figure 7. The energy resolution was 0.48% r.m.s. with the wide gate and 0.54% r.m.s. with narrow gate.

c) Full size 65 cm prototype cell for heavy ion tests

A full size 65 cm long prototype cell is being constructed at MIT to test the uniformity under realistic condition using heavy ion beams. Figure 8 shows a schematic. This chamber has 7 beam windows, spaced 10 cm apart. Inside the chamber, tapered reflector plates are installed. Using this test chamber with Si photodiodes, we will make tests for uniformity of the reflector and also the attenuation of the scintillation light over 65 cm. Because of their lower noise, photodiodes will also be used to measure the pulse shapes of liquid xenon scintillations due to heavy ions.

To investigate the uniformity of light yield in the unit cell chamber, we put the heavy ion beam into the 7 beam windows. Two photodiodes were set at the both ends of tapered reflector. The signals from two photodiodes were sent to CAMAC system to investigate the mutual light yields. However, the signals from both photodiodes were observed at the same time. Figure 9 shows the attenuation of UV light in liquid xenon for the one of the photodiodes. The light yield decrease much more rapidly as the distance between the beam entrance and the photodiode increase. We have two parameters concerning light yield: One is the attenuation length of scintillation in liquid xenon and the other is reflectivity of reflectors.

The SSC project requests more than 80% of the scintillation should be collected at both photodiodes independently of the beam entrance. Now, so, we are making reflectors whose reflectivity are more than 90% and at the same time investigating purification method of xenon so that the impurities in xenon should not absorb the scintillation light.

Concluding Remarks

We have successfully demonstrated that the combination of scintillating liquid xenon and photodiode can be high resolution (0.5% r.m.s) and fast response (20 ns) detector. However, the uniformity of light yield in the 65 cm long unit cell have not achieved yet. This problem has two aspects: One is the attenuation length of UV light in liquid xenon. The attenuation length depends on the impurity density in the liquid. The other is the reflectivity of the reflector. The results we obtained included both parameters. Therefore, we are measuring the attenuation length only in the " black box " by using cosmic μ-ons.

References

[1] T. Doke, Portgal Phys. 12 (1981) 9.

[2] T. Doke, K. Masuda, and E. Shibamura, Nucl. Instr. and Meth. A291 (1990) 617.

[3] A. Hitachi, T. Takahashi, N. Funayama, K. Masuda, J.Kikuchi, and T. Doke, Phys. Rev. B27 (1983) 5279

[4] M. Chen at al. Nucl. Instr. and Meth. A267 (1988) 43.

[5] Oxisorb is a trademarK of Messer Griesheim, Germany.

LSTAR XENON CALORIMETER
EXPLODED VIEW

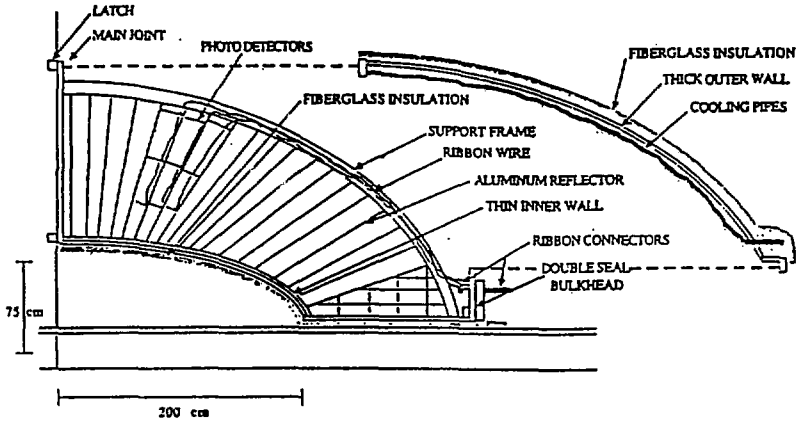

Figure 1 An exploded view of one quadrant of the xenon calorimeter with the cover removed.

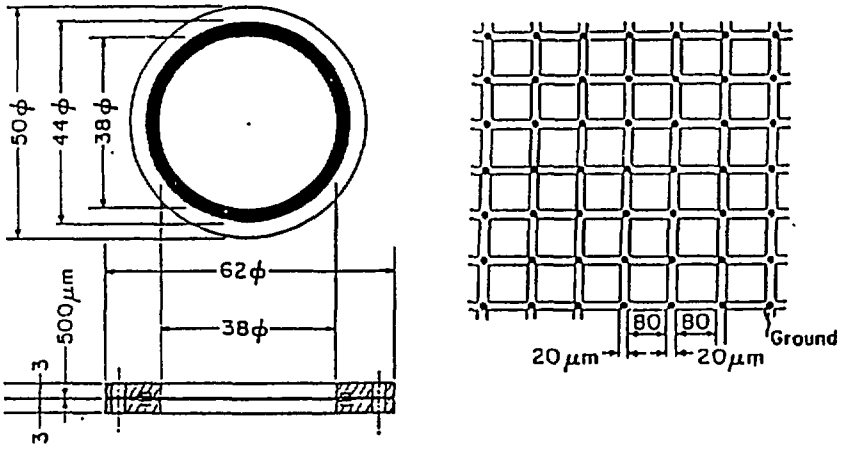

Figure 2 Schematic drawing of the silicon photodiode covered by gold mesh made by us and used for the heavy ion experiments.

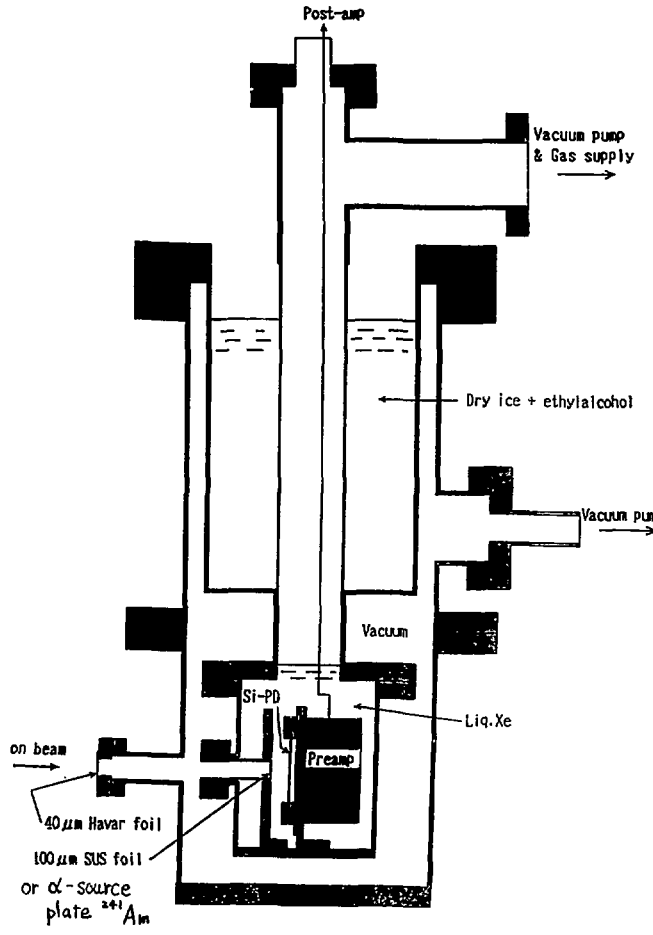

Fig.3. Schematic drawing of the liquid xenon cell.

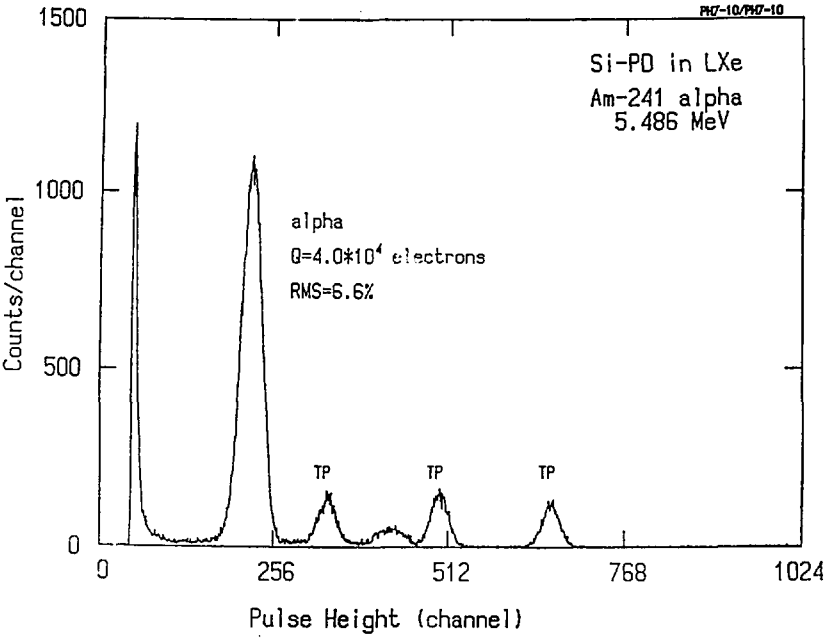

Fig. 4 Pulse height spectrum for the scintillation due to 5.5 MeV alpha particle in liquid xenon, measured by the 2" silicon photodiode.

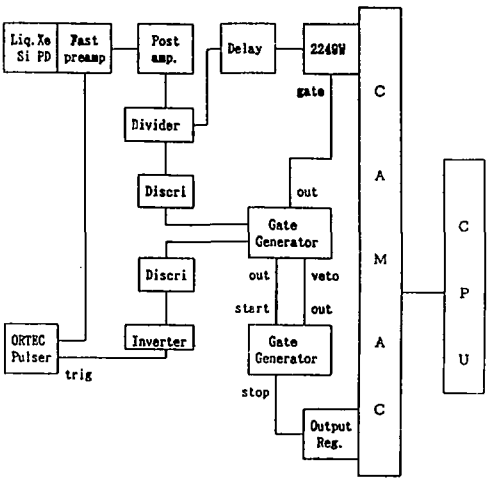

Fig.5 Block diagram of electronic circuits.

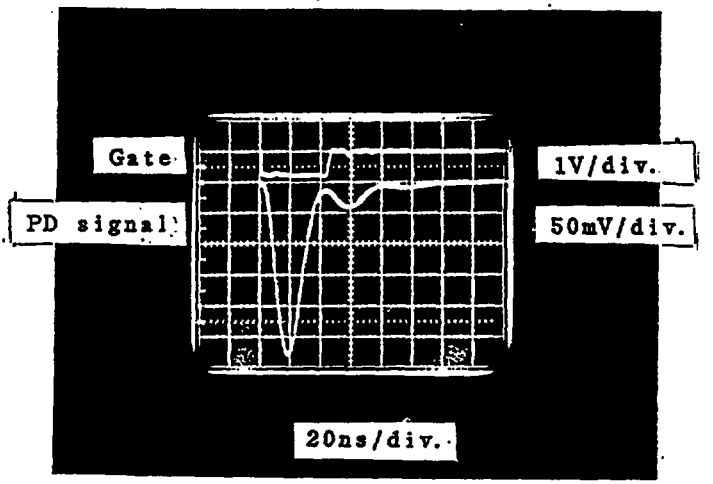

Fig.6 Typical oscilloscope photograph of the signal for liquid xenon scintillation by Al ions. Time base is 50ns/div.

Upper: gate signal originating from the linear signal of fast amplifier/photodiode. 1 V/div.

Lower: delayed linear signal from the fast amplifier/photodiode. 0.1 V/div.

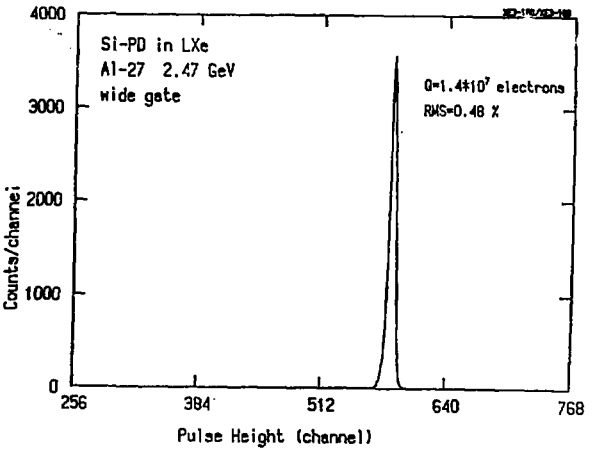

Fig.7 Pulse height spectrum measured for 92 MeV/n Al ions with a fast amplifier. The detector bias is 200 V. Gate width is 200 ns (wide). The resolution is 1.1 % fwhm.

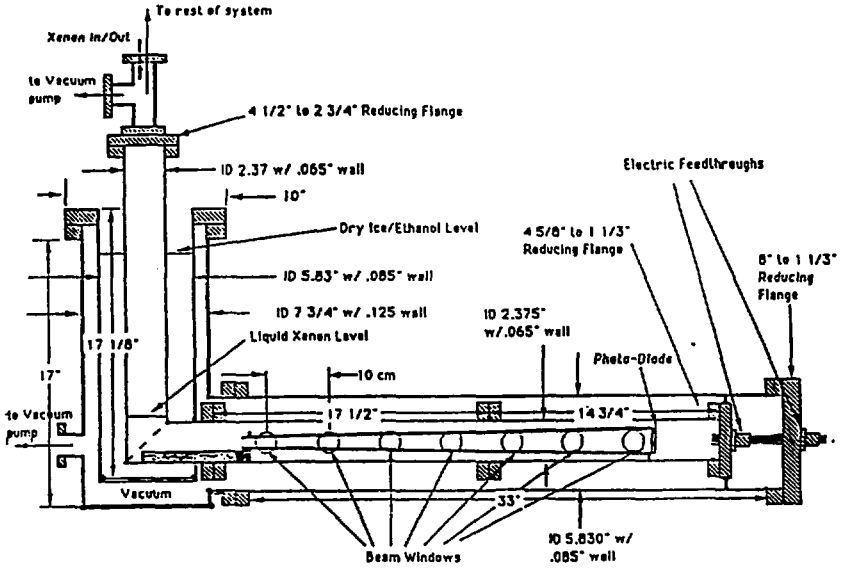

Figure 8 Schematic of a full size prototype liquid xenon cell to measure the uniformity using heavy ions, which can enter any of the seven windows. All distances are in mm.

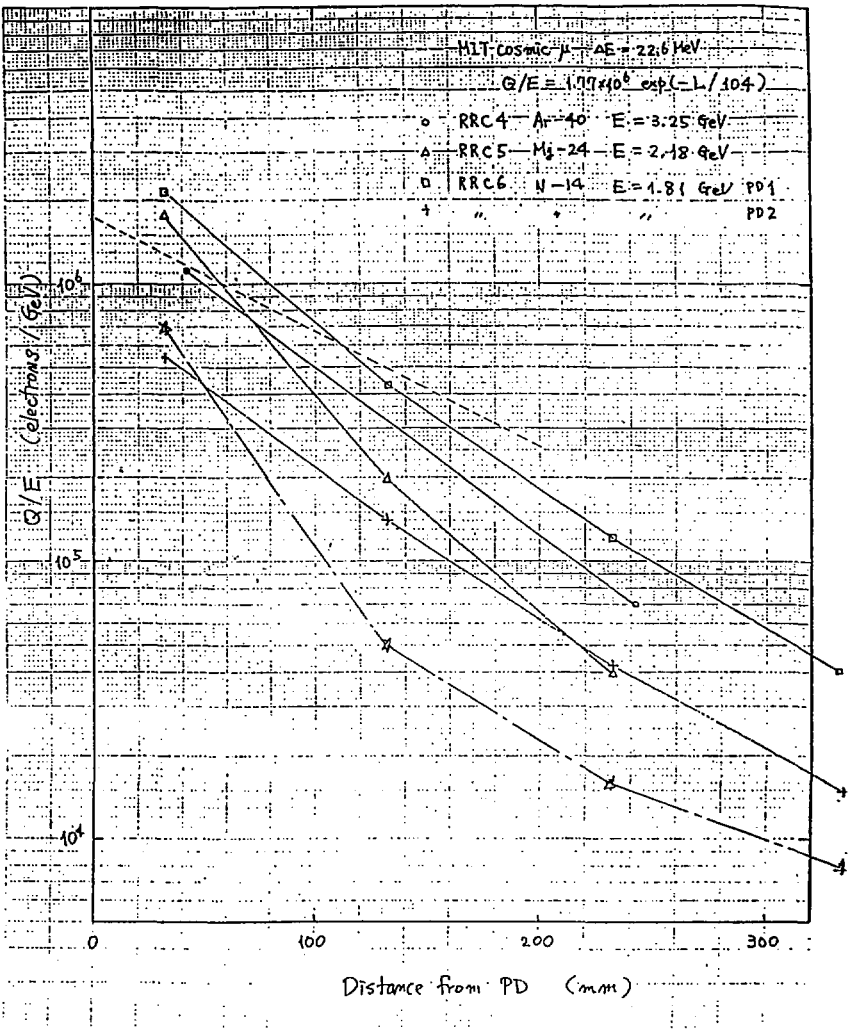

Figure 9. The attenuation of UV light in liq. Xe for cosmic muon and several ions incidence.

A DUAL TYPE GRIDDED IONIZATION CHAMBER AS LIQUID ARGON PURITY MONITOR II

Masayuki Ichige, Motoharu Utsumi, Jun Kikuchi,
Tadayoshi Doke
Science and Engineering Research Laboratory, Waseda University

Eido Shibamura, Kimiaki Masuda
Saitama College of Health

Tomiyoshi Haruyama, Yoshikuni Doi, Yoshio Yoshimura,
Mitsuhiro Miyajima, Hiromi Hirabayashi
National Laboratory for High Energy Physics (KEK)

1. Introduction

Presently, a new design of 1000 ton liquid argon time projection chamber is being made in the ICARUS project which aims to observe solar neutrinos at CERN[1,2]. In order to realize such a large type of detector, we have to design it so that most electrons produced by ionization can be collected even after a large drift gap. Here it is required to remove electronegative impurities which trap the drifting electrons. The impurity concentration has to be better than 1.5 ppb, of oxygen which corresponds to 1 meter attenuation length for drifting electrons. Here, the attenuation length of electrons is defined as the means length in which the number of electrons is reduced to 1/e. To monitor such a low level of concentration of impurities, it is important to develop both a purity monitor for liquid argon and a method to produce a large amount of ultra pure argon. Though it is generally difficult to measure impurity concentrations of order of ppb, some practical methods using ionization chambers have been reported. [3-6]

These purity monitors are divided into three types whose photo-electron production methods are different. The first type uses a very short UV laser pulse, the second cosmic rays and the third radio isotopes.

In our group, a dual type gridded ionization chamber which has two ^{207}Bi sources on the common cathode has been used for several years as a simple purity monitor. Recently, reproducible results were obtained and the purity was monitored precisely. Here we present the results of the the liquid argon purity monitor experiment by using a dual type gridded ionization chamber, as well as the argon purification system.

2. Ionization Chamber for Liquid Argon Purity Monitor

(1) Use of a very short UV laser pulse (CERN) [3, 4]

The lifetime or attenuation length of electron can be measured by the collection of drifting electrons emitted from the cathode surface by irradiation of Nd-Yag UV laser beam through a quartz fiber (Fig. 1, 2). The superiority of this method is that the charge production can be precisely controlled by the laser power, however, the laser generator is expensive and the optical system is complicated. The attenuation length in the electric field of 1kV/cm, which is the expected value to be used in the large detector, has not been obtained by this method, until now.

(2) Use of cosmic-rays (Harvard Univ.) [5]

In this metod, electrons produced by cosmic ray particle passing through the liquid argon chamber are collected by the anode of a gridded ionization chamber. The pulse shapes of the charge signal at the anode is recorded by a waveform degitiser (Fig. 3, 4). It can be expressed as a function of time which depends on the following parameters, the attenuation coefficient, the electron drift velocity and the number of electron-ion pairs

directly produced by a cosmic ray particle. By fitting the data to the function, we can get the best values of the parameters. But this method is inferior in accuracy and statistics, because of low rate of cosmic ray events.

(3) Use of RI, I (U. C. Irvine) [6]

In this method, a 50 liter chamber, which has a radio active source deposited on the cathode, the drift gap can be changed by a movable collector. The attenuation length is obtained from the variation of the charges collected with different drift gaps (Fig. 5). 1.7 meter of attenuation length was measured at the electric field 1kV/cm (Fig. 6), however the structure of the chamber is more complicated than that used in our method.

(4) Use of RI, II (Waseda Univ.) [7-10]

Our method uses a dual type gridded ionozation chamber to measure the attenuation length of electrons. The cross-sectional view of the chamber is shown in Fig. 7. This chamber consist of two gridded ionization chambers which have a common cathode. Each chamber has a different drift gap (3cm and 6cm). The ^{207}Bi sources are electrochemically deposited on both side of the cathode. Pulse height spectra in each chamber are measured (Fig. 8). We compare the pulse height of the 976keV internal conversion electrons to a test pulse. Thus we know the value of the collected charge produced by the 976 keV internal conversion electrons of ^{207}Bi. Then we can obtain the attenuation length of electrons by comparing both values of the collected charge of each collector. This method of monitoring the attenuation length is superior as it is simple and inexpensive.

3. Purity Monitor Experiment by Dual Type Gridded Ionization Chamber

(1) Experimental procedure

Argon gas (Research Grade A) from a bottle is purified by the following method, and condensed into the chamber. The purifier, uses molecular sieves (4A, 5A, 13X), a Ti-Ba getter and an Oxysorb filter (Fig. 9). After condensation, the High Voltage was applied to the common cathode, and the spectra of charge collected on the both collectors (C1, C2) were measured (Fig. 11-a, b). The peak channel from 976keV conversion electrons was measured and the value of the collected charge obtained by comparing with a test pulses.
In the dual type gridded ionization chamber, both collected charges are is given by the following formulas,

$$Q_1 = Qi \exp(-d_1/\lambda)$$

$$Q_2 = Qi \exp(-d_2/\lambda)$$

Q_1 : collected charge collected by C1
Q_2 : Collected charge collected by C2
d_1 : drift distance between K to G_1
d_2 : drift distance between K to G_2
Qi : initial charge
λ : attenuation length

where, Qi is the initial charge. Qi and λ are unknown factors.

(2) Results and discussion

We measured the attenuation length of electrons in liquid argon which was purified by molecular sieves, a Ti-Ba getter and an Oxysorb filter. The results are shown in Fig. 12. The initial charges Qi are also derived from the above formulas and these results are shown in Fig. 13. The saturation curves of initial charge are independent of the purification method.

If the impurity is assumed to be oxygen, we can calculate the oxygen equivalent impurity concentration using the following Hofmann's formula

$$\rho = \alpha E/\lambda$$

λ : attenuation length (cm)
ρ : oxygen equivalent inpurity concentration (ppm)
E : electric field (kV/cm)
α : constant 0.15+0.03 (ppm cm^2/kV) (for liquid argon)

Thus, we can estimate the electric field dependence of the attenuation length by using the value of drift velocity and the rate of attatchment cross-section. The estimated values are shown in Fig. 14, 15. When the impuritiy is assumed to 2 ppb Oxygen or 0.2 ppb N_2O, the electric field dependence of attenuation length is in good agreement with the experimental result as shown in Fig. 14 and 15. From such facts, it is concluded that the inpurity still remaining in our chamber behaves as N_2O.

4. Summery

The attenuation lengths of electrons in liquid argon purified by molecular sieves, a Ti-Ba getter and an Oxysorb filter was measured by using a dual type gridded ionization chamber. From the electric field dependence of the attenuation length, it is concluded that the type of remaining impurity is not an oxygen type, but N_2O type.

REFERENCE

(1) CERN-INFN-L'Aquila-Padova-UCLA Collab., ICARUS I:an optimized, real time detector of solar neutrinos, LNF-89/005(R) (1988)
(2) M. Cheng, D. Cline, J. Park and M. Zhou, to be published to Phys. Lett.
(3) G. Carugno et al., Nucl. Instr. and Meth. A292(1990)580
(4) A. Bettini et al., DFPD 90/EP/29 Padova(1990)
(5) E. Aprile et al., Nucl. Instr. and Meth. A241(1985)62
(6) P. J. Doe et al., IEEE Trans. NS28(1981)454
(7) M. Utsumi et al., Proc. of 3rd Workshop on Radiation detectors and Their Uses, KEK Report 88-5(1988)87
(8) M. Ichige et al., to be published to Bull. Sci. and Eng. Res. Lab. Waseda Univ. (in Japanese)
(9) M. Ichige et al., The 4th Workshop on Low-level Counting and space-based Use of Liquid Argon and Xenon Detectors, Tokyo(1990)
(10) E. Shibamura et al., to be submitted to Jpn. J. Appl. Phys.

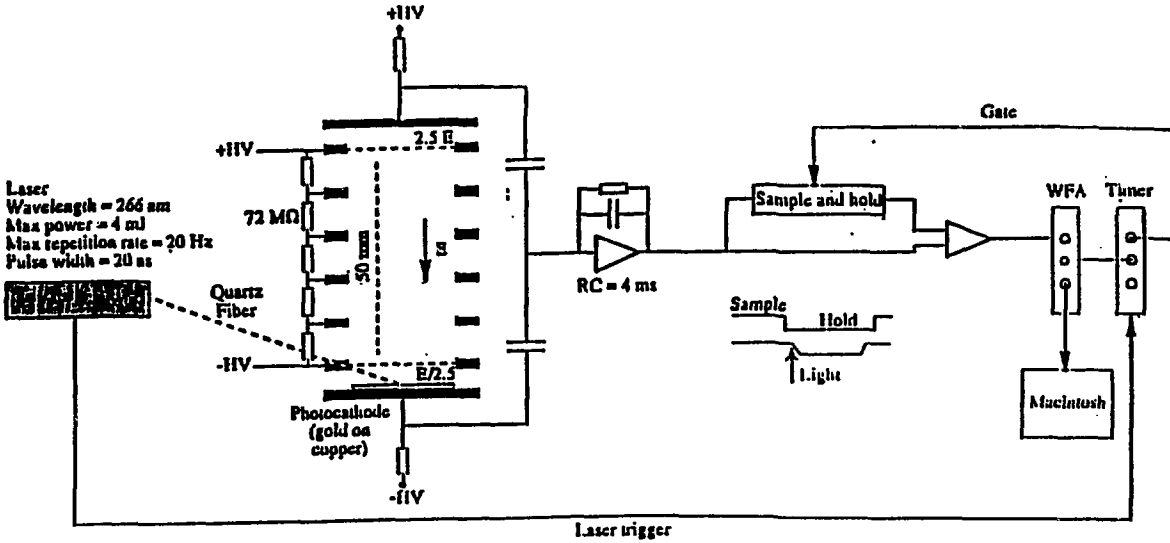

Fig. 1 The purity monitoring system by using LASER

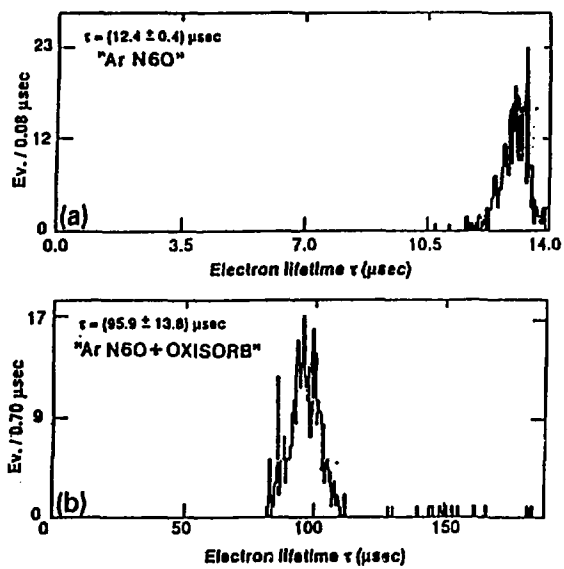

Fig. 2 The result of LASER Method. Electron lifetime at E=384V/cm
The attenuation length is calculated by the formura
$\lambda = v\,\tau$ (v:drift verocity, τ:lifetime)

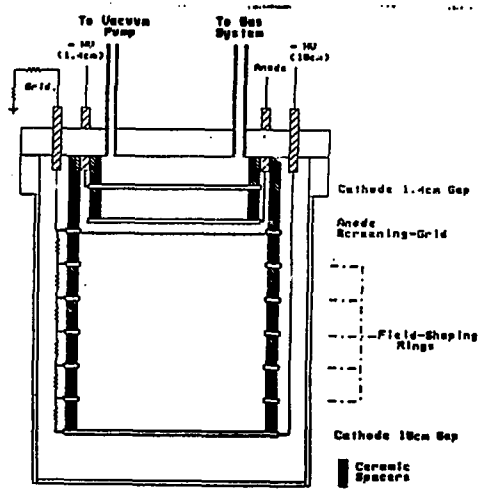

(a) Schematic cross-section of the chamber

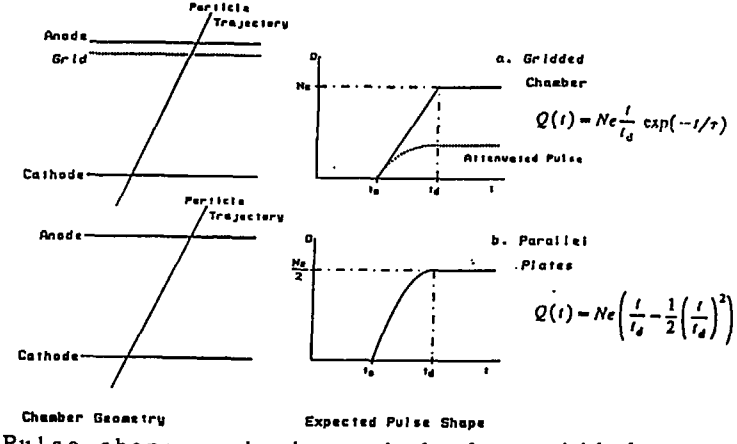

(b) Pulse shape analysis method of a gridded or a parallel plate chamber

Fig. 3 The purity monitoring method by cosmic ray particles

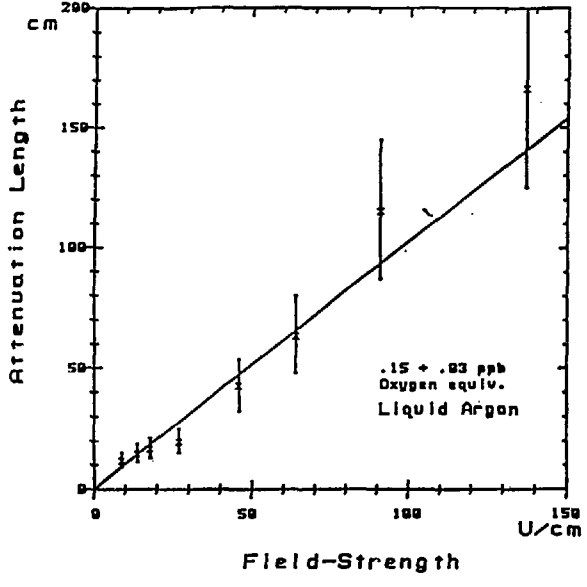

Fig. 4 The result of Cosmic ray method

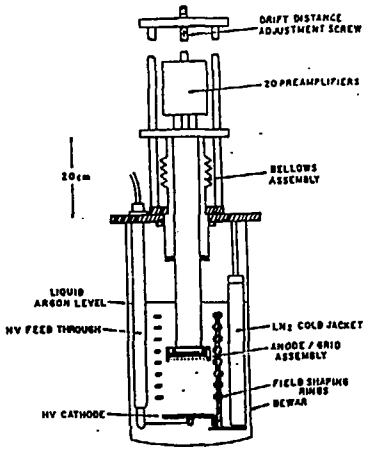

a. Schematic of the 50 liter test detector used for measuring attenuation lengths.

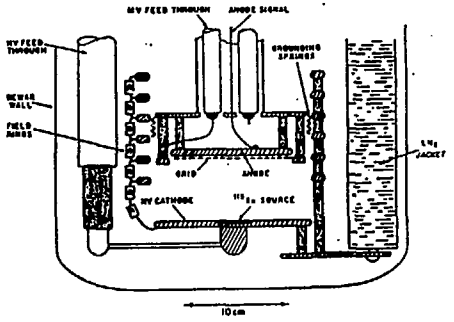

b. Details of the detector electrode assembly.

Fig. 5 The purity monitoring methodl by RI

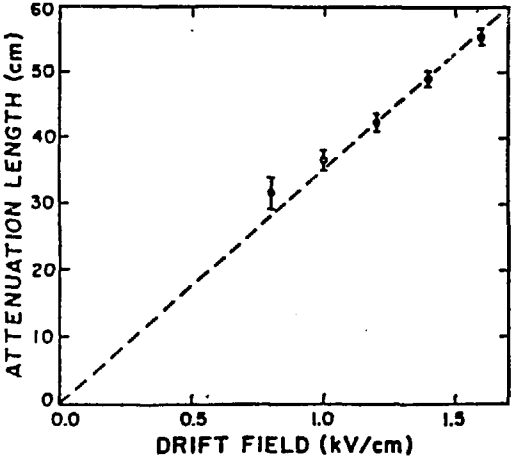

Fig. 6 The result of RI method

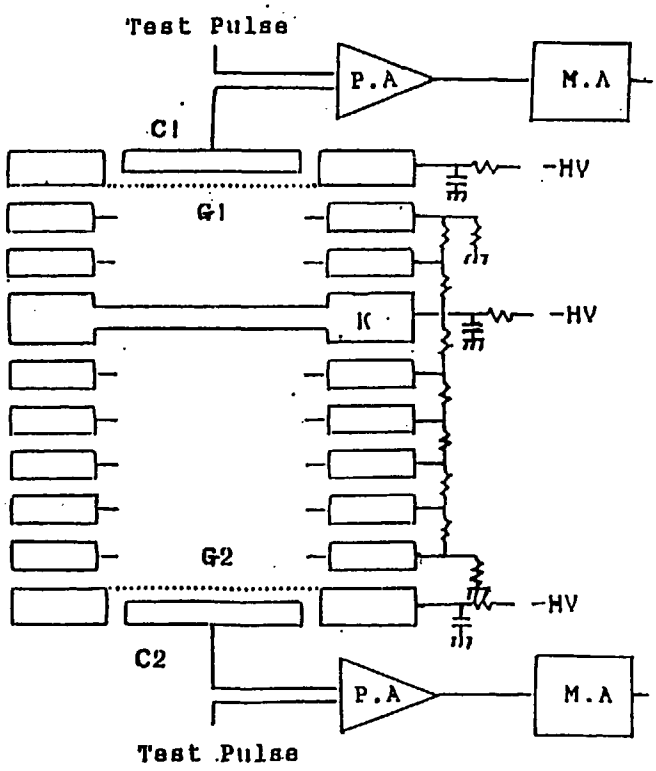

Fig. 7 The cross-sectional view of a dual type gridded ionization chamber

Effective inner diametere	:	40 mm
Grid (G1, G2) -Collector (C1, C2) gap	:	3 mm
Grid (G1) -Cathode (K) gap	:	27 mm
Grid (G2) -Cathode (K) gap	:	57 mm
Volume of liquid argon	:	900 cm^3
Grid		
Wire	:	Stainless steel
Wire diameter	:	20 μm
Wire interval	:	200 μm
Critical field ratio	:	1.92 %
Shielding inefficiency	:	1.2 %
Operating field ratio	:	3
207 Bi source		
Electrochemically deposited on both side of cathode		
γ-ray energy	:	1064 keV
K-shell internal conversion electron energy	:	976 keV
Intensity (976keV conv. electron)	:	20 cps

Table 1 Parameters of a dual type gridded ionization chamber

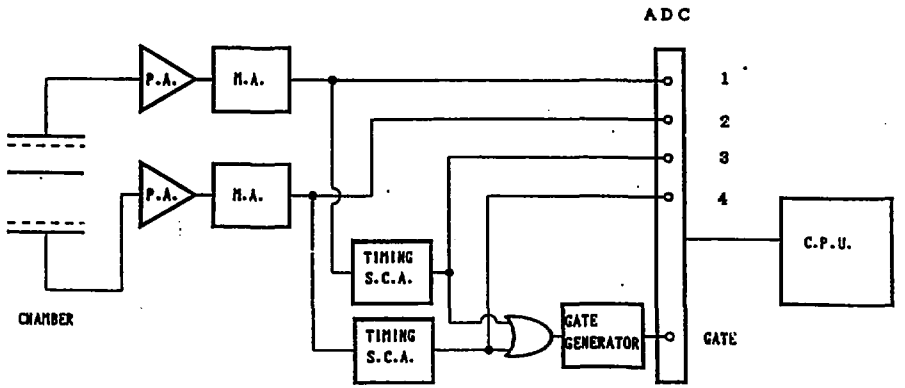

Fig. 8 Data taking system for a dual type gridded ionization chamber

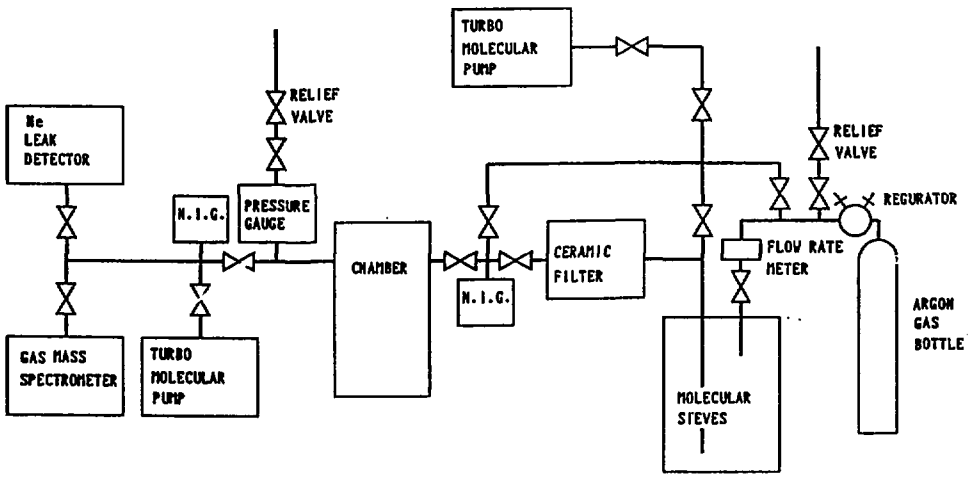

Fig. 9 Purification and evacuation system in the case of Molecular sieves as a purifier

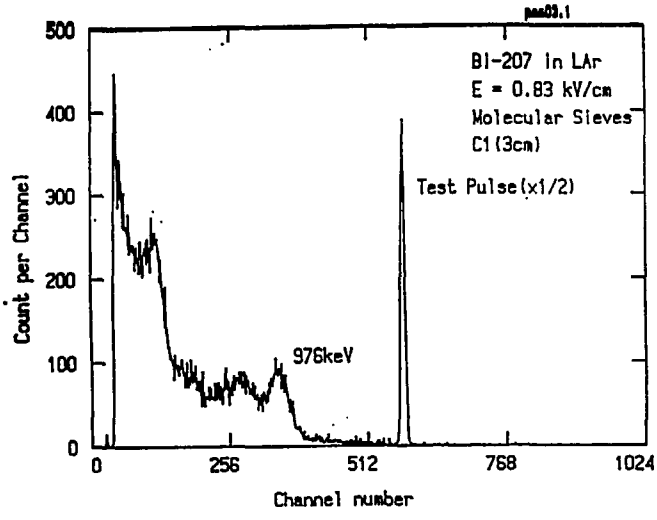

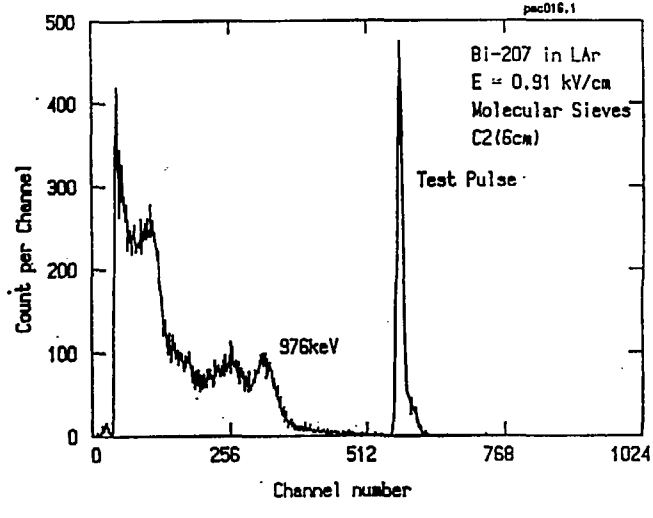

Fig. 10 Typical pulse height spectra of ^{207}Bi

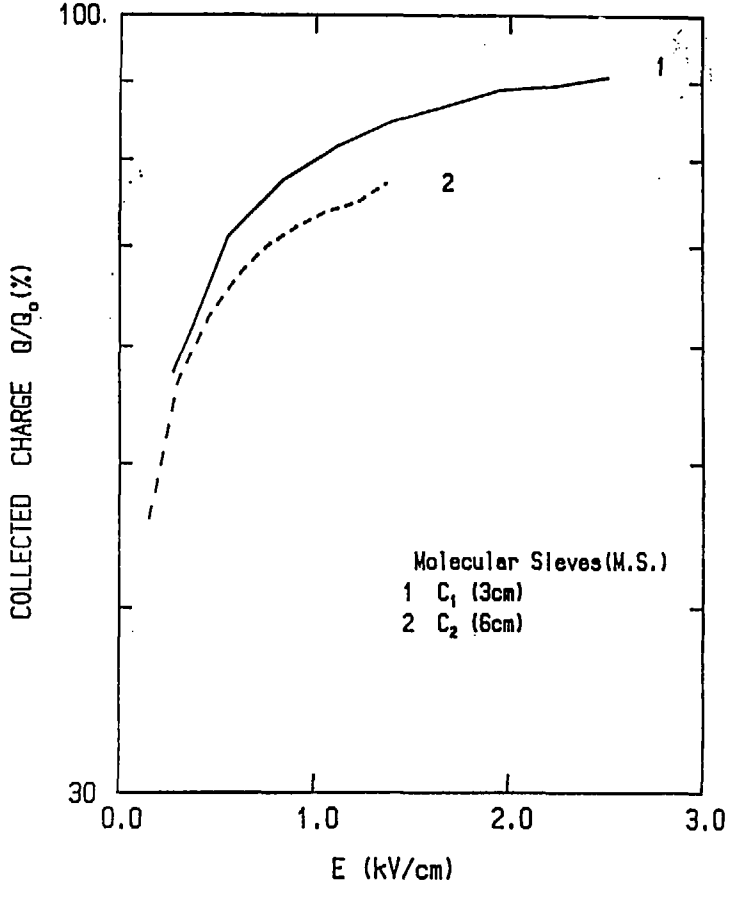

Fig. 11 Saturation curve of collected charge

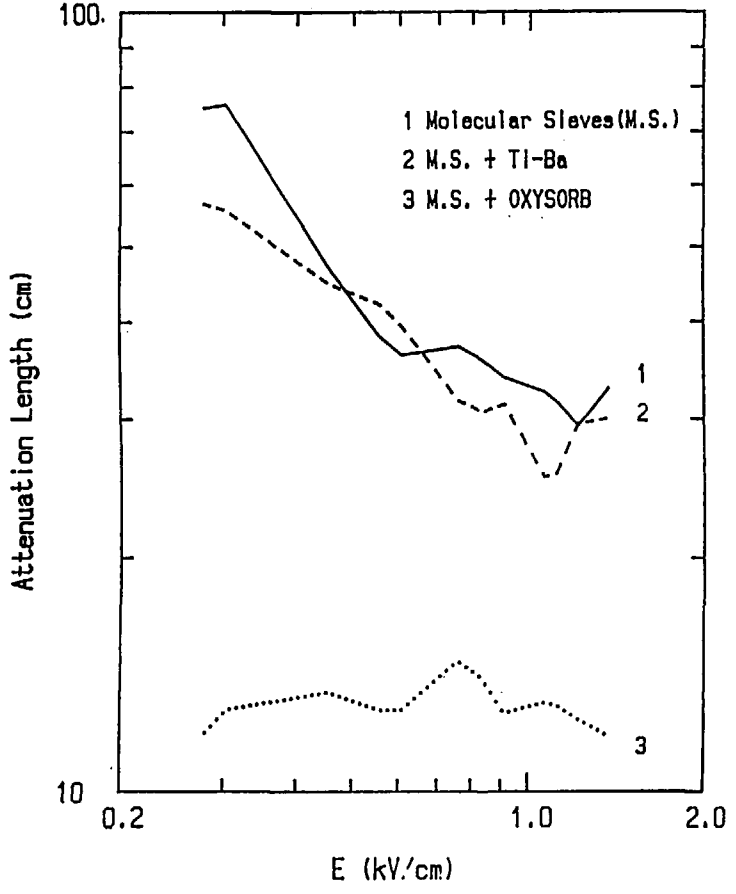

Fig. 12 Electric field dependence of attenuation length

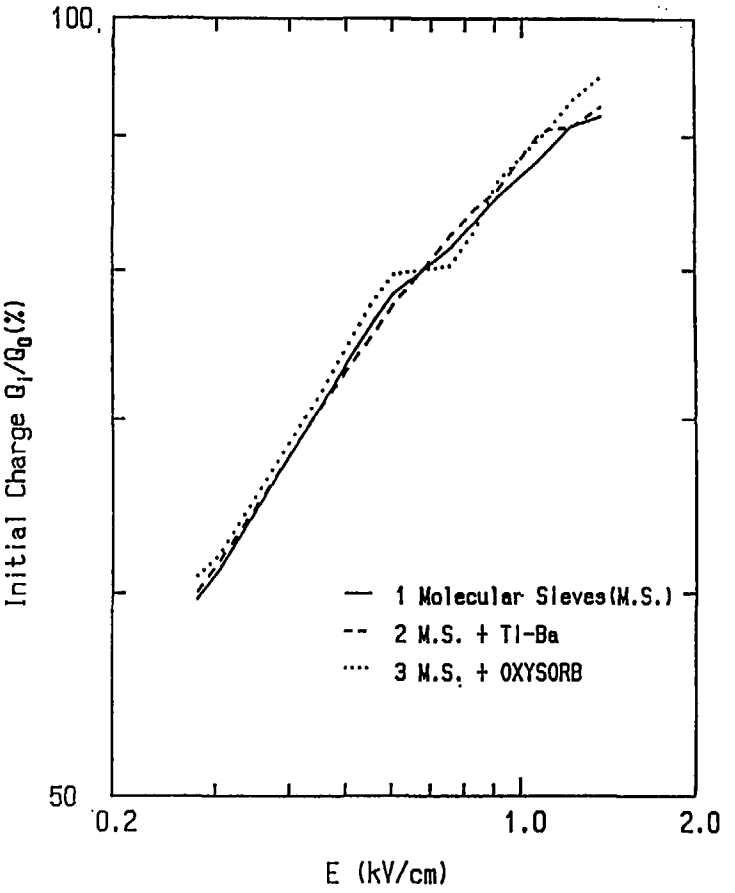

Fig. 13 Saturation curve of initial charge

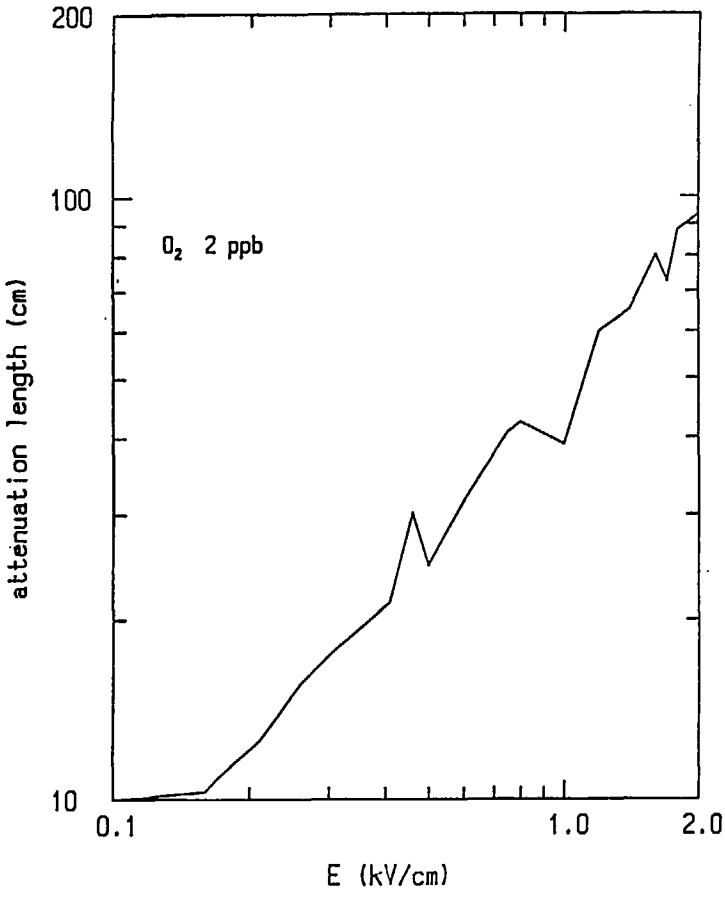

Fig. 14 Estimated attenuation length. The case of impurity is 2ppb Oxygen

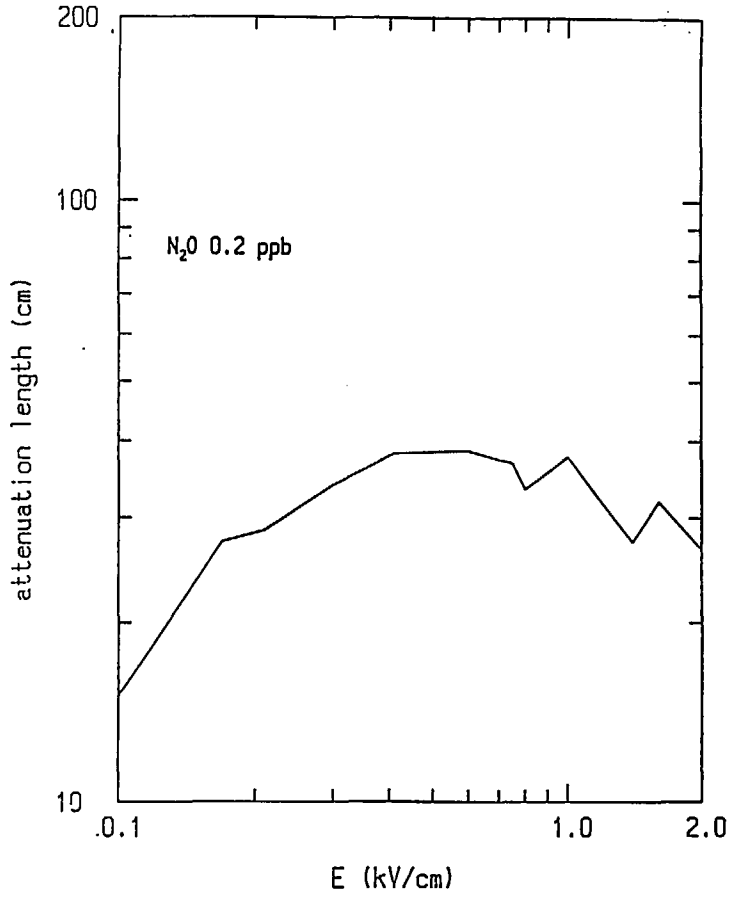

Fig. 15 Estimated attenuation length. The case of impurity is 0.2ppb N_2O

SOME TOPICS ON GAS COUNTER OPERATION

H.Ijiri, Y.Uozumi, S.Ikematsu, A.Nohtomi*, S.Widodo*, T.Sakae*
M.Matoba*, and N.Koori**

Graduate School of Engineering Sciences, Kyushu University,
Kasuga, Fukuoka 816, Japan

* Department of Engineering,Kyushu University,
Fukuoka 812, Japan

** College of General Education,Tokushima University,
Tokushima 770, Japan

INTRODUCTION

Gas discharge phenomena have been widely used for radiation detection in many types of the counter, for examples, single-wire type, multi-wire type, drift type and so on. Nowadays, they are used as a main detector in experiments on nuclear science and technology. The basic characteristics of the gas counter have been studied because it is useful for realizing the optimum condition in operation and also for investigating the gas discharge mechanism. We have been investigating the characteristics of gas counters for applying to the focal plane detector for the spectrograph RAIDEN of Research Center for Nuclear Physics, Osaka University. Several problems remained in this field to explain the mechanism of the gas counter operation are discussed as follows.

1) Some experimental data which relate to the generation of self-quenching streamer(SQS) in pure methane gas with low energy photon irradiation lead an inconsistent conclusion.
2) The data of gas amplification in avalanche can not be explained quantitatively for the change of the gas mixture.
3) Characteristics of the electron drift in the counter, which

use suitable gas mixture for large avalanche size, should be made clear for understanding the timing characteristics.

We discuss these three problems in the following section. The second and third problems will be mentioned very simply because a part of the results were already published.

1. GENERATION OF SQS IN QUENCHING GAS(CH_4) OF PROPORTIONAL COUNTER

In a large number of experiments on the transition of the self-quenching streamer(SQS) in a gas counter, two research groups have reported on investigations of SQS transition in pure quenching gases. According to the experiment by Koori et al.[1], the SQS transition was not observed in pure quenching gases with a cylindrical single-wire proportional counter irradiated by 5.9 keV X-rays. On the other hand, You et al.[2] reported that a weak but clear SQS transition was observed with 5.9 keV X-rays when pure methane gas or pure carbon dioxide gas was used in a multi-wire proportional counter with an anode wire of 76 micro meter in diameter. This problem is very important in understanding the mechanism of the SQS transition in gas counters.

So we have performed re-experiments to check whether the SQS transition occurs or not in pure quenching gas. In this experiment, a cylindrical single-wire proportional counter of simple structure was used because we considered that the electric field near the anode wire in the cylindrical gas counter where the avalanche generates is almost the same as in the multi-wire counter. The cylindrical gas counter used is made of a stainless steel pipe of 24 mm inner diameter with a nichrome anode wire of 80 micro meter in diameter. The general view of structure of this counter is shown in Fig.1. The counter is made to be able to be evacuated before experiment. The counter was filled with gas mixtures of methane and argon, and the SQS transition was investigated under experimental conditions where the fraction of argon in the gas mixture was changed from 0 to 10 %. It should be

noted that the purities of gases were better than 99.999 % for argon and 99.95 % for methane, respectively. X-rays used were 4.5 Kev Ti Kα X-rays from X-ray generator and ^{55}Fe X-rays. Figure 2 shows typical pulse height spectra observed at different anode voltages (4.3 kV to 4.6 kV) for (a) pure methane gas and (b) mixtures of the methane and argon (99:1). The numerals in the figure show avalanche sizes in pC units which are converted from the pulse height. In the case of (a), a peak corresponding to the SQS was not observed. However, it was observed clearly around 266 channel for higher anode voltages in the case of (b). Electron avalanche sizes obtained from measured pulse height are plotted against applied voltages in Fig.3. Then mixing ratios of the gases (CH_4:Ar) were changed by 100:0,99:1,98:2,95:5 and 90:10. This result shows that the addition of a small amount of argon in methane gas results in a drastic change in observed pulse height spectra. Our observation supports the experimental result by Koori et al.[1], and suggests that the existence of argon plays an important role in the generation of the SQS.

In conclusion in this section, it has been found that no jump phenomena caused by the SQS transition occur in the cylindrical gas counter with pure methane gas irradiated by keV X-rays. The results may suggest that a mixtures consist of more than two kinds of gases which have different ionization potentials generate the SQS strongly. And there may be two possible paths to reach the SQS or the Geiger discharge in accordance with the length of mean free path of release photons in the avalanche.

2. PREDICTION OF GAS MULTIPLICATION FOR MIXTURE GAS

Gas gain is generally expressed by α Townsend's first ionization coefficient α to treat the phenomena simply. Since the pioneering work by Rose and Korff was reported in 1941[3], many researchers have reported functional forms of α relating to electric field strength by using proper assumptions. The formulas of Diethorn[4] ,Williams and Sara[5], Zastawny[6] and Charles[7] have been known to represent experimental data on gas gain. The

theoretical and the mathematical relation between these formulas have been discussed by Aoyama[8] and Miyahara[9] et al. In these formulas, α is treated macroscopically and in a phenomenological way. Also there are some free parameters which have physical meaning slightly and must be chosen to fit the experimental data.

In the present work, a semi-microscopic formula for α will be developed by introduction of the simplified model of the inelastic and the ionization impact cross sections between electrons and gas molecules. The model characterizes the cross sections with three fixed parameters and first ionization potential of each gas. The results of calculation will be compared with experimental results on gas gain of some kinds of gas mixtures under some counter geometries. The calculation values of α with Ne and the values that determined experimentally are shown in Fig.4. These results are consistent comparatively. The details have been described in reference 11).

3. DRIFT CHARACTERISTICS OF A COUNTER WITH SUPPLEMENTAL ELECTRODES

We have developed a gas counter system for use in the experiments with magnetic spectrograph RAIDEN of RCNP, Osaka University. The filling gas of the counter is now changed from argon based gas to neon based gas in order to get large gas gain. By using the gas mixture, it is possible to operate the counter at low anode voltage stably. In this counter system, there is a problem that the counting rate characteristics are inferior to those of former system. Therefore, a counter with supplemental electrodes is investigated for improvement in the problem. Figure 5 shows the cross sectional view of the counter. This has double construction including two counters. These counters have a nichrome anode wire of 15 micro meter in diameter and nichrome supplemental wires of 50 micrometer in diameter. Drift characteristics of the counter are shown in Fig.6 for the Ne : CH_4 (7:3) + C_2H_5OH(5.1%) mixture. The counter was irradiated by Sr β -rays through a 10 micro meter thick aluminized mylar attached

on front and rear counter walls. In the figure, the drift time is shown for three cases (voltage of the supplemental electrodes is GND, -250V, and -500V). The improvement of the drift characteristics is very clear in the results at the region far from the anode position. Details of this topic are shown in reference 12).

References

1) N. Koori, T. Ueda, K. Ogawa, T. Sakae, H. Kametani and I.Kumabe, IEEE. Trans. Nucl. Sci. NS-33(1986)395.
2) T.J. You, H.F. Chen, B.Z. Yang and H.W. Tang, Nucl. Instr. and Meth. A252(1986)61.
3) M.E. Rose, and S.A. Korff, Phys. Rev. 59(1941)850.
4) W. Diethorn, US Atomic Energy Commission Report NYO-6628(1962).
5) A. Williams, and R.I. Sara, Int. Jour. Appl. Radiat. Isot. 1(1962)229.
6) A. Zastawny, Jour. Sci. Instr. 43(1985)179.
7) M.W. Charles, Jour. Phys. E5(1972)95.
8) T. Aoyama, Nucl. Instr. and Meth. A234(1985)125.
9) H. Miyahara, M. Watanabe, and T. Watanabe, Nucl. Instr. and Meth. A241(1985)186.
10) A. Von Engel, Ionized Gases (Oxford Univ. Press,London,1965).
11) Y. Uozumi, Doctoral Thesis Kyushu Univ., 1991.
12) S. Ikematsu, R. Yamaguchi, A. Kisanuki, S. Widodo, Y. Uozumi T. Sakae, and M. Matoba, Eng. Sci. Rep. Kyushu Univ. Vol.13, No.1(1991)37.

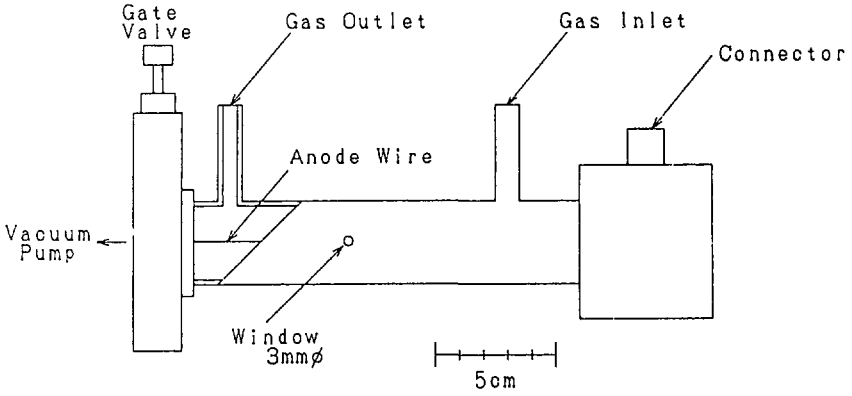

Fig. 1 Shematic view of the single-wire proportional counter.

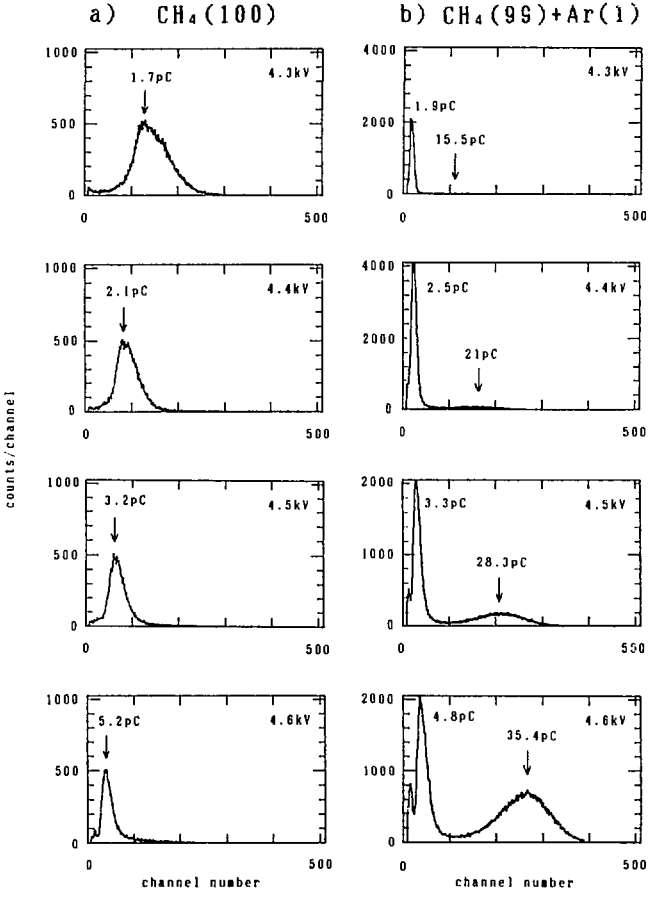

Fig. 2 Typical pulse height spectra obtained with the proportional counter for (a) pure methane gas and (b) mixtures of the methane and argon gas (99:1).

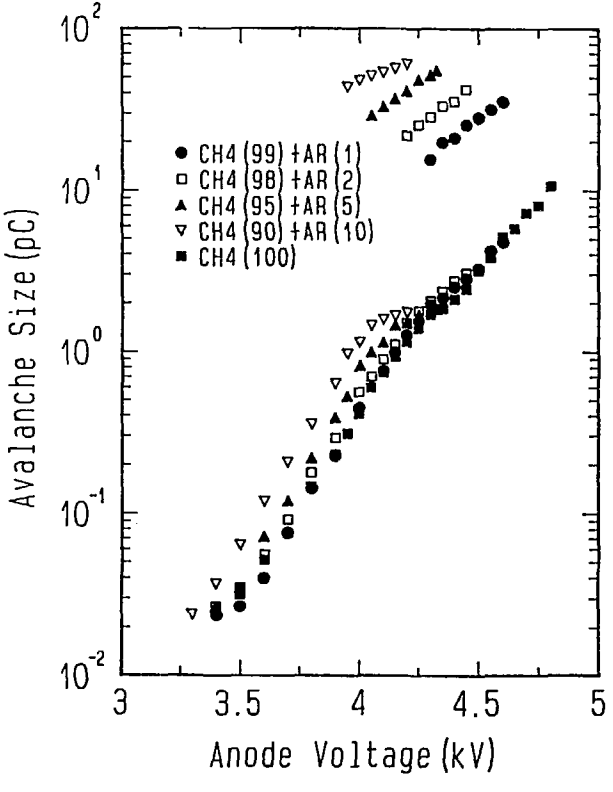

Fig. 3 Avalanche size as a function of the applied anode voltage for the different mixtures of CH_4-Ar.

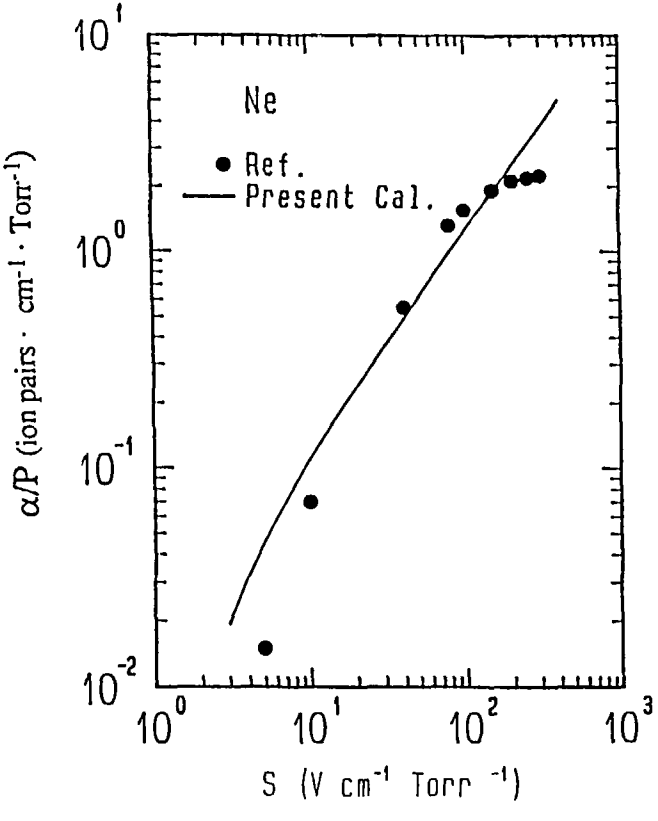

Fig. 4 Calculated values of α for Ne and experimental values in ref. 10).

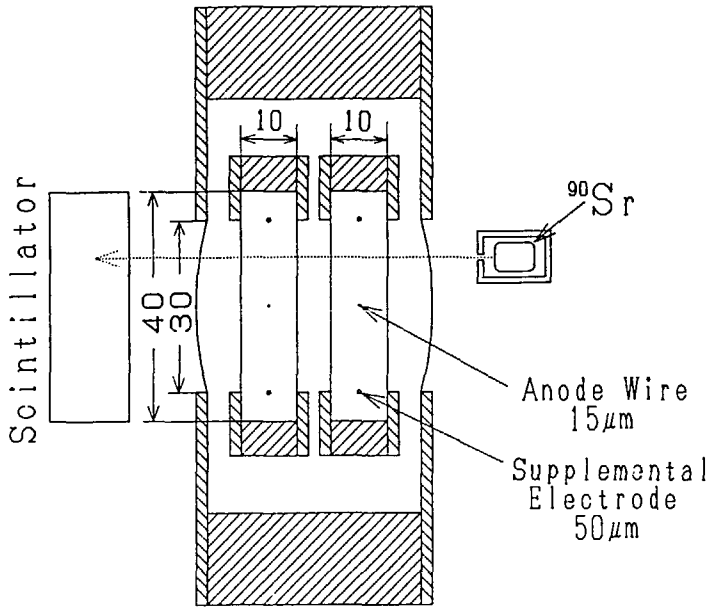

Fig. 5 Cross sectional view of the counter used.

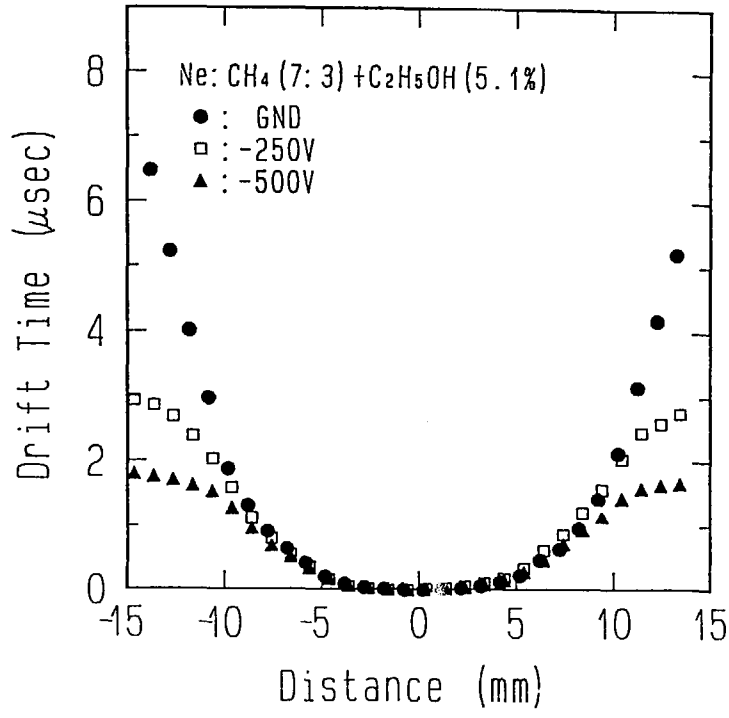

Fig. 6 Drift time of the electrons as a function of source position in filling gas mixtures Ne-CH_4.

Track-Depth Resolved Luminescence of 5 MeV/amu N-Ions Injected into Near-Liquid and Liquid Helium

Kazuie Kimura
The Institute of Physical and Chemical Research (RIKEN)
Wako, Saitama 351

Abstract A track scope was developed using an imaging quartz fiber and a position-sensitive photon counter. Using this scope, specific luminescence, dL/dx, luminescence efficiency, dL/dE, were measured as functions of range and stopping power regarding with N^{7+}-ion impinged dense gas and liquid helium. Also, measurements were done with variation of helium density. The peak positions of dL/dx, which shift to short ranges by plots of abscissa of the range or dE/dx, coincide by a plot of the tentative excitation density. An extra peak of dL/dE observed near the track termination cannot be explained by the high density effect or by usual scintillation theory. It suggests the importance of extra processes such as the direct excitation and charge exchange.

1. Introduction

One of the most characteristic irradiation effects of heavy ions in condensed matter is the high-density excitation of electrons in an outermost shell. The high-density effect is much larger than that estimated by dE/dx especially near termination of an ion and its maximum should be shifted to the track end. In addition, extra processes such as charge-exchange, which are not included explicitly in stopping power calculation [1,2], become important in the region aforementioned. What is actually caused in matter near the track termination is considered to be an important unknown problem to be resolved. Then, we developed a track-scope to measure depth-resolved UV- and VUV-emission which are the probes of excited states and their reactions[3].

2. Methods

The scope was composed of an imaging fiber-bundle of 1 m in the length, a stainless-steal slit of a cross section of 2 x 0.1

mm for beam entrance, and the sliding mechanisms to find the maximum beam flow and to look the full length of ion-tracks[3]. This fiber bundle was an experimental pilot production by Furukawa Electronic Co. LTD. A plane of the fiber bundle was attached to the plane of the beam-entrance slit, where a light-entrance plane of the fiber bundle was separated by 0.1 mm from the slit. (See fig. 1a.) Also, by a sliding mechanism along the beam flow, the fiber bundle could slide from 0 to 4.26 mm along the beam direction, that is, the scope could observe the ion track of the maximum length of 6.26 mm. The square image projected from the end of the bundle should be composed of 100 lines of 100 sectored luminescences of ion-tracks. This image was enlarged and focused on a photoplate of a 500 channel position-sensitive photon counter(OMA 1, Optical Multichannel Analyzer by Princeton Applied Research) by a lens system, and accumulated for an appropriate time interval.(See Fig.1b.) Considered a visual angle of 11.5 degree of the fiber, the distance of 0.1 mm between the fiber and the beam, and the

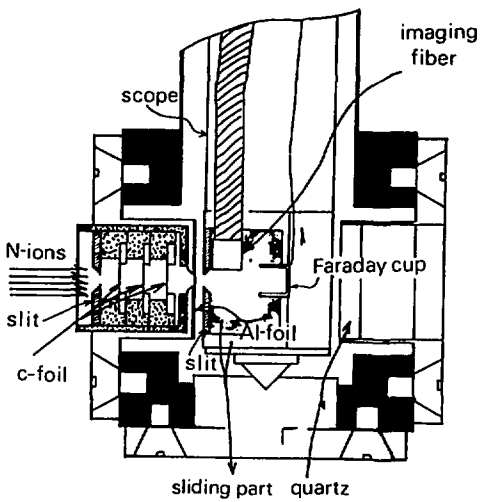

Fig. 1a. Relative arrangement of a cold part of a cryostat, an ion counter, beam slit system, and a scope composed of an entrance slit and an imaging fiber.

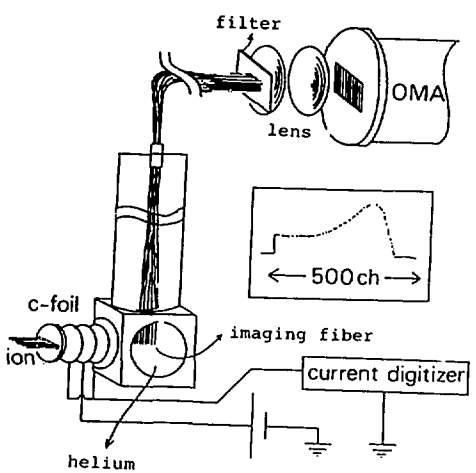

Fig. 1b. A track scope composed of an imaging fiber, an ion counter, a cryostat, a position-sensitive photon counter (OMA), and an on-line computer.

interval of 0.02 mm between the fibers, a depth resolution of this scope may be about 0.02 mm. Relative intensities of spectral peaks could be obtained by measurements using interference filters if any, since the peaks to be appeared can be predicted from previous works (Ref. 4, 5 and those cited in them) and discussions in a section of later discussion. A tentative measurement in VUV-range was done by comparing the luminescence with coating sodium salicylate on the entrance surface of the fiber bundle and without that.

Research grade helium gas by Takachio Chem. was accepted without further purification. Helium gas was pressurized or liquefied by adjustment of the pressure from about 1000 to 3000 Torr at a constant temperature around 7.5K. By the adjustment of the pressure and hence density, appropriate track-lengths could be obtained; helium was in liquid phase at the density higher than about 0.05 g/cm^3. Since we have no density data available to present extreme conditions, the helium density was estimated reversely from Northcliffe's table of range in a unit of mg/cm^2 as a function of ion energy, by using known ion energy and track lengths in mm measured experimentally.

N ions of 5.0 MeV/amu, accelerated by the 160 cm cyclotron in our institute, were cut by four beam slits to a 2 x 0.1 mm slit beam and led to the scope. N ions were degraded to 4.656 MeV/amu through the penetration of three carbon foils of 0.01 mg/cm^2 density, an aluminum foil of 1.619 mg/cm^2 density. N ions were further degraded through helium of a pass length of 0.95 mm from an aluminum-foil window to the bundle front-edge, according to the experimental helium-density.(See Fig.1a) This degradations were corrected using density data and Northcliffe's table to

obtain the net incident energy of ions ; the incident energy was 3.687 MeV/amu at the density of 0.0316 g/cm^3. N ions were counted using a C-foil detector mounted in a cylindrical hole in a front flange of a cold part of cryostat.

3. Results and discussion

Depth-resilved luminescence and dE/dx-dependent dL/dX and dL/dE

Specific luminescence , dL/dx , of N-ion-impinged helium was measured as functions of the track depth (in mm) with variations of helium density from 0.02 to 0.07 g/cm^3.(See Fig. 2.)

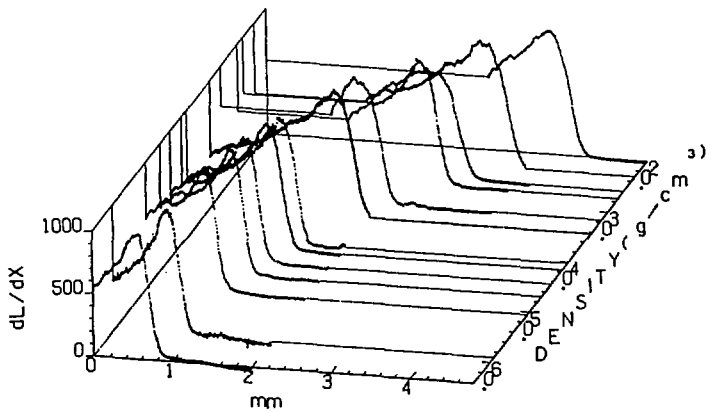

Fig. 2. Specific luminescence, dL/dx, vs the depth of N-ion track and its helium-density dependence. All the curves are drawn at the same height. The ordinate is expressed in arbitrary units.

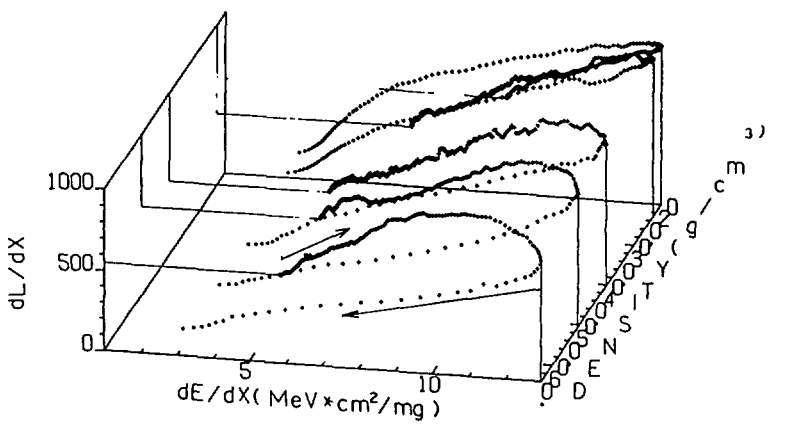

Fig. 3. dL/dx vs stopping power and its helium-density dependence. The right-hand ends of the abscissa correspond to the maximum stopping power. Arrows show the directions of ion propagation. Flows of ions are illustrated as reflected at the maximum stopping power.

The range (in g/cm^2) of incident N-ions, R, can be obtained from Northcliffe's table. This range R is considered to be a sum of the radiative range (corresponding to the length of luminescence multiplied by density) and the nonradiative range R_o where only elastic collisions occur. The latter R_o was a minimum value, 0.069 mg/cm^3 on the table corresponding to 0.0125 MeV/amu. Corresponding ionic velocity is about 1/3 of that of an electron in helium 1S orbital and therefore may be regarded as the limit of inelastic collisions. Based on these values, stopping powers, ranges , and ionic energies at given track depths were obtained by the interpolations of the table data. Although Fig. 2. was illustrated in an equiheight for the maximum dL/dx, the total luminescence or the area of dL/dx or the average dL/dx had the peak between 0.020 and 0.03 g/cm^3 , although figures are not given.

Figure 3 shows a plot of dL/dx vs. dE/dx as a function of the density. Since with ionic propagation, dE/dx varies as increasing, attaining to the maximum, and then decreasing, dL/dx as a function of dE/dx looks as reflected at the maximum dE/dx, 12.985 $MeV*cm^2/mg$.

The luminescence efficiency, dL/dE, obtained by dividing dL/dx by dE/dx, are given in Fig. 4 as a functions of dE/dx and the density. The dL/dE at the lowest helium density increases continuously with propagating ions, even after passing through the maximum stopping power, and decreases rapidly near stopping power of 5 $MeV*cm^2/mg$. At 0.023 g/cm^3 , dL/dE is nearly constant till a stopping power lowers near 5 $MeV*cm^2/mg$. At further higher helium density, dL/dE showed a plateau, a decrease, a

plateau again, and decreases below 5 MeV*cm^2/mg, sequentially. Such an increase or a plateau near the maximum stopping power is unpredictable phenomenon by usual scintillation experiments and theories. The dL/dE can be derived from simple and familiar Voltz theory [6]:

$$dL/dE = [\ (1-F)\exp\{-B(1-F)dE/dx\} + F\ ]q/W \qquad \langle 1 \rangle$$

where F is a ratio of dE/dx for production of fast secondary electrons to total dE/dx and F decreases rapidly towards the maximum dE/dx [7]; B, a constant dependent on target material; q, a quantum yield for luminescence; W, an average excitation energy. Equation 1 shows that in a region of increasing dE/dx with propagation of ions, dL/dE is sure to decrease rapidly. A correction of Eq. 1 for contribution of triplet-triplet reactions [6] cannot reverse the decreasing tendency with dE/dx. Present phenomena are therefore considered to originate from particular excitation and decay mechanisms which becomes important for low energy heavy-ion.

mechanisms of luminescence and enhancement of dL/dE

As reported previously, origins of luminescence are the transitions between Rydberg states of helium excimers in the present experimental systems, but are not excited atoms [4,5]. Emissions observed are due to transitions of $d^3 \rightarrow b^3$ (6396 A), $D^1 \rightarrow B^1$ (6590 A), $J^1 \rightarrow C^1$ (7040 A), and $H^1 \rightarrow C^1$ (7289 A) in VIS and UV regions; $C^1 \rightarrow A^1$ (9136 A) for near infrared ; $A^1 \rightarrow X$ (800 A) for VUV, in Herzberg's notation [8]. Of these transitions, $d^3 \rightarrow b^3$ was strongest in the present system. Namely, they are the transitions of the principal quantum

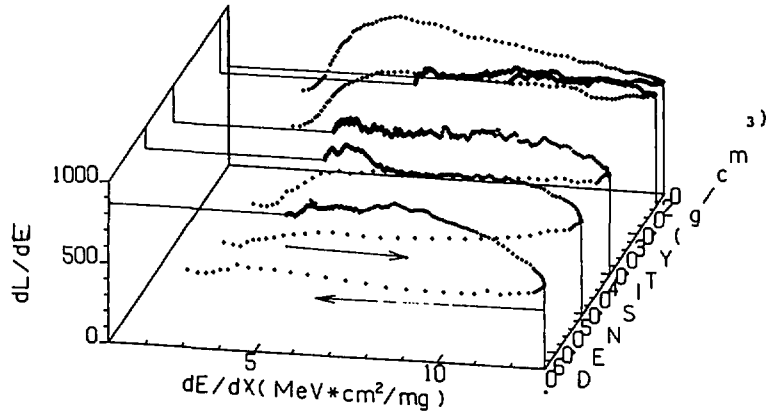

Fig. 4. Luminescence efficiency, dL/dE, vs stopping power and its helium-density dependence. The ordinate is in arbitrary units.

number smaller than 4, because large orbitals are inhibited in dense helium. The dL/dx of the VUV emission was V was apparently less than 1/10 of that of VIS emission.

Emissions of helium excimers are characterized by cyclic regenerations of higher level excimers by bimolecular reactions of the lowest triplet excimers, a^3 [4,5,9]:

$$a^3 + a^3 \longrightarrow d^3 , c^3 , D^1 , C^1 , + 2He \quad (1)$$

which were ascertained by following linearity:

$$I_d^{-1/2} = I_{d0}^{-1/2} + kt, \quad \langle 2 \rangle$$

where I_d and I_{d0} stand for emission intensities of d^3 at time t and at time 0, respectively. Although this linearity is destroyed in liquid states at pressure higher than 2 atm, the linearity is sustained at present condition [10]. The reaction 1 is decisively important for the observable emissions, since higher excimers relax to the lowest excimers, a^3 or A^1, and a^3 has lifetime as long as ms. For these reasons, a^3 can have a high concentration. Therefore, almost all emissions observed originate from excimers

formed by reaction 1 and hence their intensities are expressed by Eq. 2. Since $I_{d0}^{-1/2}$ is proportional to the reverse of initial concentration of a^3 [9], luminescence intensities are decided consequently by the concentration of a^3 in the present case. Reaction 1 is characteristic in helium and important, since it allows nonradiative a^3 to be converted into radiative excimers.

Enhancement and quenching of dL/dx and dL/dE

The quenching processes of higher-level excimers regenerated such as d^3 are not important, since the linear relation of Eq.1 is held in the present density. In general, most helium excimers suffer slightly quenching by their collisions, as shown previously [4,5]. It seems more likely that excited helium atoms or cations, formed initially or intermediately through reaction 1 (doubly excited states exceed ionization potential), are at too high density to find two ground-state atoms for excimer formation by three body process.

Excitation-density dependence of dL/dx and dL/dE

Now, the variation of dL/dx and dL/dE is discussed regarding with the excitation density instead for using dE/dx, since dE/dx means energy gain of a target in a cross section of width dx at the depth x but doesn't mean the excitation density. We suppose tentatively that the significant track is composed principally of a core part and a radius due to a halo part can be neglected. In case of the ion energy concerned here, less than a few hundred KeV/amu, ions can not eject many secondary electrons of

sufficient energy to excite helium atoms distant from the track core [7]. Since the track radius is approximated to be proportional to the particle velocity based on Brandt-Ritchie [3], the excitation density is proportional to (helium density) x $dE/(v^2 dx)$ or (helium density) x dE/(Edx).

Figure 5 is helium density dependence of dL/dx as functions of the above excitation densities estimated along the depth of the track. The peaks of dL/dx coincide at the same excitation density independently of the helium density. The enhancing and quenching mechanisms aforementioned may be also appropriate since they are dominated by the densities of excited states.

Figure 6 illustrates a remarkable finding that dL/dE peaks at higher excitation density or at deeper track-depths after the peak of dL/dx. The peak shifts towards higher excitation density with increasing helium density, which means the rise of new processes for enhancement of dL/dE, apart from the effect of high-density excitations. These peaks cannot be explained by scintillation theory, and have not been found in scintillation experiments. To explain the increases observed in the present study, therefore, some extra mechanisms must be taken into account. Increase in dL/dE means an increase in the conversion rate of the energy deposited to the luminescence or a decrease in W in Eq. 1. As for candidates for these mechanisms, direct excitation and charge exchange processes may be proposed. The former is efficient as luminescence process, since it can produce excited states without energy loss by sequential processes of ionization, recombination, and relaxation to radiative excited states. The latter is a process contained not in the calculation of stopping power.

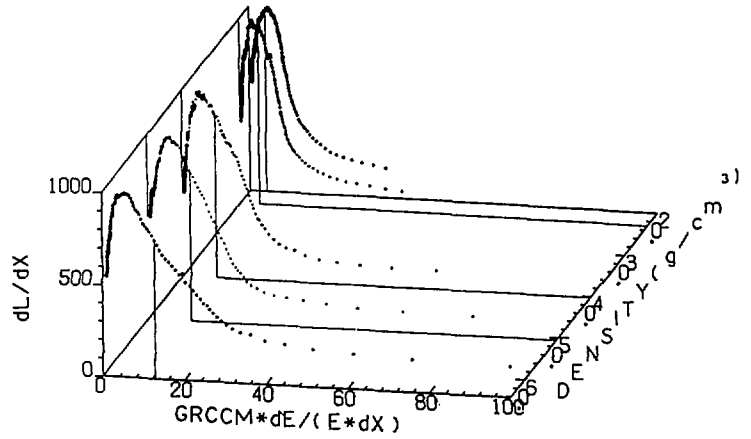

Fig. 5. dL/dx vs excitation density and its helium-density dependence. The excitation density was assumed to be described by (helium density)$\times(dE/dx)/E$. The notation, GRCCM, in the abscissa stands for the helium density. The perpendiculars from the curves to their bottoms shows the positions of the maximum stopping power. Both ordinate and abscissa are in arbitrary units.

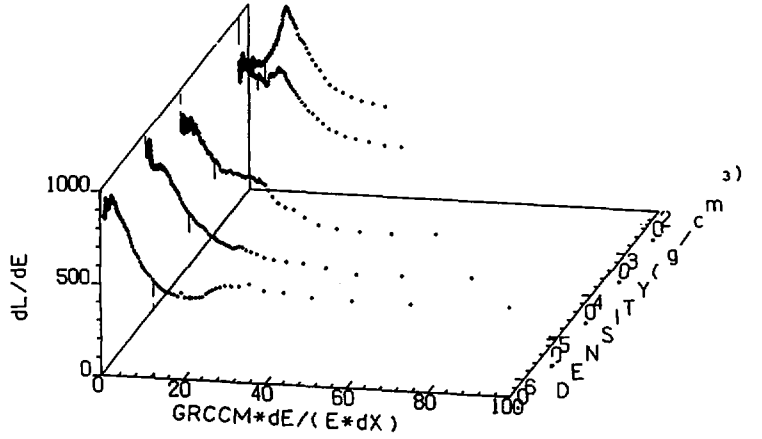

Fig. 6. dL/dE vs excitation density and its helium density dependence. Both ordinate and abscissa are in arbitrary units.

According to Lindhard and Scharff [13], stopping power is proportional to the velocity in low-ion-energy region such as our case and hence (dE/dx)/E is proportional to 1/velocity. Actually, a plot using 1/v showed that peak positions coincide closely. This result may support our proposal of charge exchange and direct excitation processes, since these processes are principally dependent on the velocity. Alternately, peaking may occur if there are errors of stopping power. Northcliffe calculated stopping powers based on Lindhard's theory in a

region of low energy ions. An unnatural bend is recognized in a low energy region of a plot of dE/dx vs. energy of Northcliffe's data. Although this bend didn't lead aforementioned peaking, further experiments may be required with remarks for applicability of Northcliffe's data and Lindhard's theory in low energy ions as the present system, along with the correction for extra processes aforementioned.

References

[1] L. C. Northcliffe and R. F. Schilling, Nuclear Data Tables(Academic, New York, 1970).
[2] J. F. Ziegler, " The Stopping and Ranges of Ions in Matter", (J. F. Ziegler ed.) Pergamon Press (1980).
[3] K. Kimura, Nucl. Instr. Meth. B53(1991)301
[4] K. Kimura, J. Chem. Phys., 84, (1986) 2002.
[5] K. Kimura, J. Chem. Phys., 84, (1986) 2010.
[6] R. Voltz, J. Lopes da Silva, G. Laustriat, and A. Coche, J. Chem. Phys. 45 (1966) 3306.
[7] F. D. Becchetti, C. E. Thorn, and M. J. Levine, Nucl. Instrum. Methods 138 (1976) 93.
[8] K. P. Huber and G. Herzberg, " Molecular Spectra and Molecular Structure. IV. Constants of Diatomic Molecules" Van Nostrand Reinhold, New York (1978).
[9] J. W. Keto, F. J. Soley, M. Stockton, and W. A. Fitzsimmons, Phys. Rev. A10 (1974) 887.
[10] to be published.
[12] J. Lindhard and M.Scharff, Phys. Rev., 124(1961)123.

A NEW CANDIDATE FOR THE RESIDUAL DEFECT IN A SILICON SURFACE BARRIER DETECTOR[1)]

Ikuo Kanno
Japan Atomic Energy Research Institute
Tokai-mura, Naka-gun, Ibaraki 319-11, Japan

INTRODUCTION

The pulse height defect (PHD) in a silicon surface barrier detector (SSB) has been a great interest in view of both experimental and theoretical efforts. The PHD has been considered separately as, (1) energy loss in the entrance window, (2) energy loss by nuclear stopping and (3) energy loss caused by other effects. The theme researchers have been concerned is the third defect, called residual defect.

The residual defect was attributed to the recombination of electrons and holes which were created by an incident particle and formed a plasma column. Numbers of works have been carried out to explain the residual defect by estimating the number of recombined electrons and holes.[2)-7)] The researchers, however, did not pay any attention how the plasma column was formed and eroded.

Models of formation and erosion of the plasma column were proposed by the present author[8)] for the consistent understanding of the residual defect and the plasma delay, another unfavorable feature of the SSB. With these models, the electric property of a plasma column was predicted to change from conductor-like to dielectricity-like, when it started to erode. Following these models, the author reported a model of charge collection process in the SSB[9)], applying Ramo's theory[10)].

This paper proposes another candidate for the residual defect. An application of the model of the charge collection process leads to the another origin of the residual defect than the recombination of the electrons and holes. A new candidate for the residual defect

is the incomplete charge induction by the electrons and holes inside the dielectric plasma column. With this consideration, the depletion layer thickness dependence of the residual defect, which was firstly reported by Schmitt *et al.*[11] and has not been reproduced by the models of recombination, is easily explained. The experimental results of the residual defect which were measured by two SSBs with 362Ωcm and 2100Ωcm in resistivity for ^{58}Ni ions were presented and were analyzed by the model of incomplete charge induction.

THEORETICAL

A schematic drawing of depletion layer of an SSB and a plasma column are shown in Fig. 1.

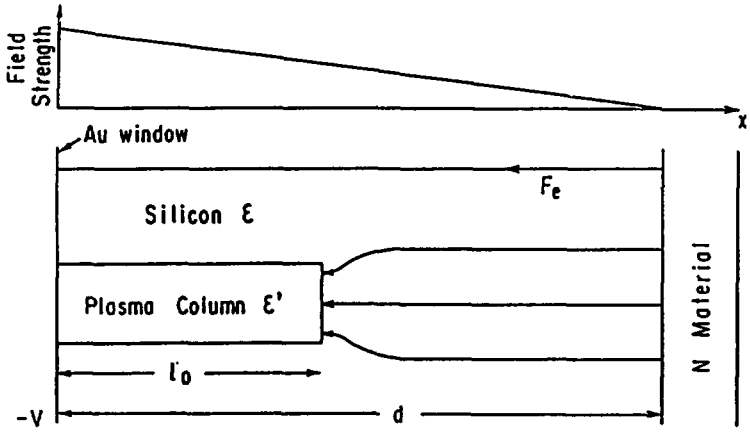

Fig.1 Schematic drawing of SSB and plasma column

According to the Ramo's theorem, the induced charge ΔQ is proportional to the distance of electron and hole movements Δx,

$$\Delta Q = e\frac{\Delta x}{d}. \tag{1}$$

When the electron and hole reach the positive and negative ends of the depletion layer after moving the distance d, the unit charge e is induced. The depletion layer thickness d

is given as a function of bias voltage V and the resistivity of an SSB, λ,

$$d = (2 \times 10^{-12} \mu_e \lambda V)^{\frac{1}{3}}, \tag{2}$$

where, μ_e is the electron mobility.[12)-14)]

The plasma column is assumed to have cylindrical configuration with homogeneous electron-hole density inside it. As described in the introduction, the plasma column has the dielectric property at the time of erosion. The negative and positive charges are induced at the top and bottom surfaces of the dielectric plasma column. They screen the movement of carriers inside the plasma column from the positive and negative electrodes. The distance of electrons and holes moving inside the plasma column is not effective to induce charges on the electrodes. In the followings, the distance of electrons and holes moving inside the plasma column is calculated.

An electron inside the plasma column moves toward the positive end of the depletion layer according to the equation[9)],

$$x_e(t) = d - (d - x_0) exp(-G(t)/\tau), \tag{3}$$

while the top position of the plasma column approaches to the electron[9)],

$$l_t(t) = d - (d - l_0) exp(\mu_h G(t)/\mu_e \tau). \tag{4}$$

Here, μ_h is the hole mobility and $G(t)$ is a function of time t.[9)] From these two equations, the point that the electron escapes from the plasma column x_e is calculated as,

$$x_e = d - (d - x_0)^{\frac{\mu_h}{\mu_e + \mu_h}} (d - l_0)^{\frac{\mu_e}{\mu_e + \mu_h}} \tag{5}$$

Integrating Eq.(5) for the initial point of the electrons x_0, the total distance of electrons moving until they escape from the plasma column ΔX_e is obtained as,

$$\Delta X_e = S\rho\left[l_0 d - \frac{1}{2} l_0^2 + \frac{\mu_e + \mu_h}{\mu_e + 2\mu_h} d^2 \left\{ \left(1 - \frac{l_0}{d}\right)^2 - \left(1 - \frac{l_0}{d}\right)^{\frac{\mu_e}{\mu_e + \mu_h}} \right\}\right]. \tag{6}$$

Here, S and ρ are the cross section and electron-hole density of the plasma column. Similarly, the total distance of holes moving until they escape from the column ΔX_h is calculated as,

$$\Delta X_h = S\rho\left[\frac{1}{2} l_0^2 - l_0 d + \frac{\mu_e + \mu_h}{2\mu_e + \mu_h} d^2 \left\{ 1 - \left(1 - \frac{l_0}{d}\right)^{\frac{2\mu_e + \mu_h}{\mu_e + \mu_h}} \right\}\right]. \tag{7}$$

The total distance of electrons and holes ΔX which does not contribute to the charge induction is described as,

$$\Delta X = \Delta X_e + \Delta X_h$$

$$= S\rho d^2 \left[\frac{\mu_e + \mu_h}{\mu_e + 2\mu_h}\left\{\left(1 - \frac{l_0}{d}\right)^2 - \left(1 - \frac{l_0}{d}\right)^{\frac{\mu_e}{\mu_e+\mu_h}}\right\} + \frac{\mu_e + \mu_h}{2\mu_e + \mu_h}\left\{1 - \left(1 - \frac{l_0}{d}\right)^{\frac{2\mu_e+\mu_h}{\mu_e+\mu_h}}\right\}\right]. \quad (8)$$

The total distance D after the whole electrons and holes inside the plasma column arriving at the electrodes is calculated as,

$$D = S\rho l_0 d. \quad (9)$$

The effectively induced charge quantity Q_c is obtained as,

$$Q_c = Q_0 \frac{D - \Delta X}{D}, \quad (10)$$

where Q_0 is the number of electron-hole pairs created by an incident charged particle.

In Eq.(10), the number of induced charge is derived for the "completely dielectric" plasma column. The plasma columns formed by charged particles with various mass numbers, atomic numbers and energies have, however, the electron-hole densities which range to some orders of magnitude. The screening of the inner movement of carriers from the electrodes is expected to change according to the carrier density of the plasma column. The "screening factor" should be multiplied to ΔX to calculate the appropriate collected charge.

The screening factor f is assumed to have the following conditions, (1) for the completely dielectric plasma column $f = 1$, (2) for the plasma column with carrier density ρ less than critical density ρ_c, $f = 0$. We define the screening factor f as,

$$f(\rho) = c(\rho - \rho_c)^k, \ \rho > \rho_c$$

$$= 0, \qquad \rho < \rho_c. \quad (11)$$

Here, c is a normalization constant and k the exponent. The critical carrier density will be determined referring to α particles and other light particles which have been reported to have small residual defect[2].

The residual defect Δ_r is obtained as,

$$\Delta_r = wQ_0 f(\rho)\frac{\Delta X}{D}, \quad (12)$$

where w is the energy to create a pair of electron and hole. The collected charge ratio Q_c/Q_0 is calculated as,

$$\frac{Q_c}{Q_0} = 1 - f(\rho)\frac{\Delta X}{D}. \qquad (13)$$

Here, calculated results of collected charge ratio are presented assuming the screening factor as, 0.25, 0.5,0.75 and 1. Collected charge ratios are shown in Fig.2 for the plasma columns with the lengths of (a) $10\mu m$ (almost equal to the range of the fission fragment of $\sim$ 0.5 MeV/amu) and (b) 20μm ($\sim$ 1 MeV/amu) as a function of the depletion layer thickness. The bias voltage dependence of the collected charge ratios are given in Fig.3 for the SSBs of 350, 700 and 2100Ωcm in resistivity.

EXPERIMENTAL

Experiments were carried out using the Tandem Accelerator of Japan Atomic Energy Research Institute. Nickel ions were injected to an SSB with energies of 109.0 and

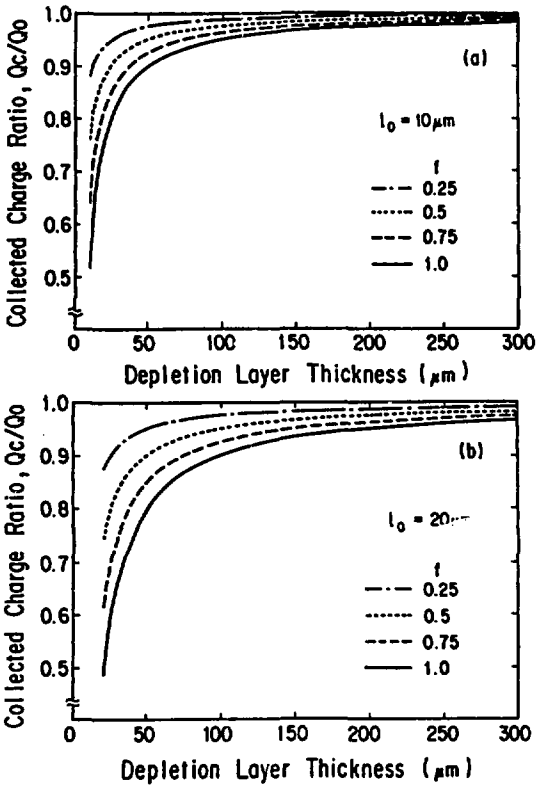

Fig. 2 Collected charge ratios as a function of depletion layer thickness with plasma column length (a) 10μm and (b) 20μm. The screening factors are indicated in the figuras.

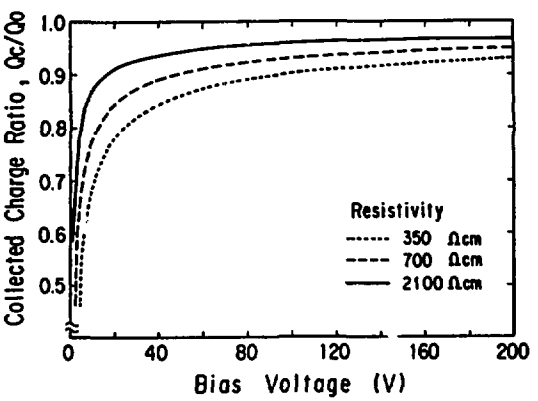

Fig. 3 Collected charge raios as a function of bias voltage with plasma column length of 20μm for detector resistivity of 350, 700 and 2100Ωcm. The screening factor is taken as unity.

160.0MeV. In the experiments, two SSBs were employed (ORTEC F-series, effective area 300mm^2). The resistivities of the SSBs were 362 and 2100 Ωcm, respectively. Measurements were carried out at ten bias voltages up to 90 and 200V for the SSB of 362 and 2100Ωcm, respectively. The measured peak channels of the pulse height are shown in Fig. 4 as a funciton of depletion layer thickness. The full width at half maximum of the pulse height is almost the same size as the symbols.

For the determination of the energies spent to produce electron-hole pairs E_0, the window defect Δ_w and the nuclear stopping defect Δ_n were calculated. The nuclear stopping defect was calculated following the method of Wilkins *et al.*[2] The window defect and the plasma column length (range of charged particle) were calculated by the code OSCAR[15], which employed the semi-empirical formula of Ziegler *et al.*[16] In Table 1, window defect and nuclear stopping defect are presented as well as lengths of plasma columns.

Table 1 Energies deposited in SSB

E_i (MeV)	Δ_w (MeV)	Δ_n (MeV)	E_0 (MeV)	l (μm)
109.0	0.4	0.9	107.7	18.0
160.0	0.4	0.9	158.5	24.5

For the determination of the screening factor, the linear response of pulse height analyzer is employed,

$$E = ay + b, \tag{14}$$

where E is the energy of nickel ion measured by an SSB, y the channel number of pulse height peak, a and b are constants which must be determined. Here we rewrite Eq.(13) as,

$$E_{i,k} = E_{0i}(1 - f_i \cdot g_{i,k}), \tag{15}$$

where subscript i and k indicate the energy of incident particle ($i = 1, 2$), and the data point ($k = 1, N$, N:number of data points). The variable $g_{i,k}$ is a function of plasma column

length l and the depletion layer thickness d as,

$$g_{i,k} = g(l_i, d_k)$$

$$= \frac{d_k}{l_i}\Big[\frac{\mu_e+\mu_h}{\mu_e+2\mu_h}\Big\{\Big(1-\frac{l_i}{d_k}\Big)^2 - \Big(1-\frac{l_i}{d_k}\Big)^{\frac{\mu_e}{\mu_e+\mu_h}}\Big\} + \frac{\mu_e+\mu_h}{2\mu_e+\mu_h}\Big\{1-\Big(1-\frac{l_i}{d_k}\Big)^{\frac{2\mu_e+\mu_h}{\mu_e+\mu_h}}\Big\}\Big]. \quad (16)$$

The correlation between the pulse height $y_{i,k}$ and the energy is written as,

$$E_{i,k} = E_{0i}(1 - f_i \cdot g_{i,k}) = a_i y_{i,k} + b_i. \quad (17)$$

With two data points of the same particle, the constants a and b are determinted as,

$$a_i = \frac{g_{i,l} - g_{i,k}}{y_{i,k} - y_{i,l}} f_i E_{0i},$$

$$b_i = \Big\{1 + \frac{g_{i,k}y_{i,l} - g_{i,l}y_{i,k}}{y_{i,k} - y_{i,l}} f_i\Big\} E_{0i},$$

$$(k, l = 1, N, l \neq k), \quad (18)$$

Equating a_1 and a_2, b_1 and b_2, screening factors are derived as,

$$f_i = \frac{(y_{i,k} - y_{i,l})(E_{0j} - E_{0i})(g_{j,n} - g_{j,m})}{E_{0i}\{(g_{j,n} - g_{j,m})(g_{i,k}y_{i,l} - g_{i,l}y_{i,k}) - (g_{i,l} - g_{i,k})(g_{j,m}y_{j,n} - g_{j,n}y_{j,m})\}},$$

$$(i, j = 1, 2, j \neq i), (k, l = 1, N, l \neq k), (m, n = 1, N, n \neq m). \quad (19)$$

Calculation should be carried out with the data taken at high electric field strength to avoid the effects which would be induced under weak electric field strength, such as trapping and recombination of carriers. For this purpose, the experimental data at the largest four depletion layer thickness with the SSB of 362Ωcm in resistivity were employed. In Eqs. (18) and (19),

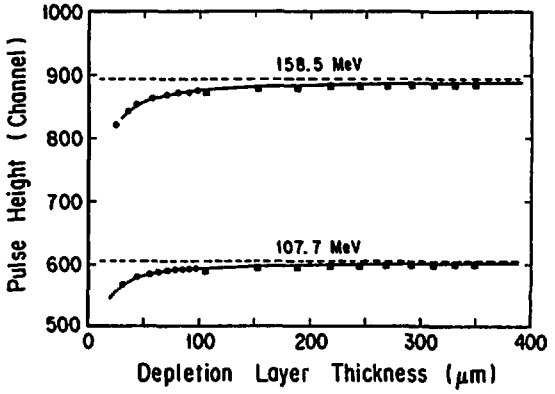

Fig. 4 Pulse heights of nickel ions. Experimental data are shown in symbols (with • 362Ωcm, ▪ 2100Ωcm SSB). The meanings of solid and dashed lines are explained in text.

every combination of (k,l) and (m,n) was calculated. The calculated results were simply averaged, because the full width at half maximum of each data is almost the same. The constants a and b were determined as, 0.18MeV/channel and 1.07MeV.

The screening factors of the plasma column which were produced by nickel ions with energies of 107.7 and 158.5MeV were obtained as 0.21 and 0.16, respectively. The energies which should be observed by the SSBs are calculated by Eq.(15), transferred to pulse heights by Eq.(17) and are shown in Fig.4 by solid lines. The dashed lines in Fig.4 indicate the pulse heights which correspond to the energies E_0 in Table 1.

DISCUSSIONS

The charge collection ratios are presented for the plasma column lenghts of 10 and 20μm in Fig.2(a) and (b). At the depletion layer thickness 100μm (362Ωcm SSB with bias voltage 100V), the charge collection ratios are 0.99 and 0.98 for the plasma column lengths of 10μm and 20μm, respectively, with the screening factor 0.25. The difference between the collected charge ratios is rather small, however, it becomes greater for the case of greater screening factor, *i.e.*, in the measurement of heavy ions with low energy. Thicker depletion layer is preferred when the detected charged particles range various mass numbers and energies, for the accurate determination of their energies.

The dependences of the residual defect on the resistivity of SSB and on the bias voltage have been a difficult problem to be solved for the model of recombination effect. The principle of the model of recombination is that the number of recombinations is greater/less in the weaker/stronger electric field strength in the depletion layer. The maximum electric field strength F_{max} is determined by the bias voltage and the depletion layer thickness,

$$F_{max} = \frac{2V}{d} \propto \left(\frac{V}{\lambda}\right)^{\frac{1}{2}}. \tag{20}$$

With this point of view, the pulse height measured with the SSB of lower/higher resistivity should be higher/lower, applying the same bias voltage. This prediction has been contradicted to the experiments.[17] The model of incomplete charge induction explains this

experimental result, easily. With the same bias voltage, the thickness of the depletion layer is greater in the SSB of higher resistivity. The distance of the carriers moving inside the plasma column becomes smaller portion of the depletion layer thickness and the collected charge ratio becomes greater.

The difference between the dashed line and the experimental point in Fig. 4 has been called the residual defect. As shown in Fig. 4, the experimental result of pulse height, *i.e.* the residual defect is excellently reproduced by the model of incomplete charge induction. The experimental results obtained by the SSB of 2100Ωcm resistivity look slightly lower than the theoretical curves, however, they are in the error bars which are almost the same size of the symbols. Figure 4 indicates the validity of the model of incomplete charge induction. It does not prove, however, that the recombination of electrons and holes does not play an essential role. The author thinks that the direct evidence of which the main cause of the residual defect is, the recombination or the incomplete charge induction, will be obtained by experiments employing a calorimeter. The thermal output of the SSB will vary with the bias voltage if the recombination is the main cause of the residual defect, on the other hand, it will stay almost the same in the case of the incomplete charge induction being valid.

CONCLUSION

The candidate for the residual defect in an SSB was proposed. The new origin of the residual defect was the incomplete charge induction by electrons and holes inside a plasma column, which had dielectric property. With this model, the dependences of the residual defect on the applied bias voltage and on the resistivity of the SSB were clearly explained, which have not been reproduced by the model of recombination of electrons and holes. A method of analysis employing this model was also proposed. The experimental results of the residual defect of ^{58}Ni ions of 107.7 and 158.5MeV in energy were reported and were successfully explained by the model of incomplete charge induction. Applying this model, the energy of charged particle would be determined more accurately than before.

ACKNOWLEDGMENT

The author would like to express his acknowledgment to Prof. I. Kimura of Kyoto University for his fruitful discussion. He is also grateful to Dr. Y. Kaneko, Japan Atomic Energy Research Institute (JAERI), for his encouragement. In the experimental set-up and accelerator operation, the author is very thankful to Drs. H. Ikezoe, Y. Nagame and T. Ohtsuki, and operation staffs of Tandem Accelerator of JAERI.

REFERENCES

1) I.Kanno, J. Nucl. Sci. and Technol. **28** (1991) 87.

2) B.D.Wilkins, M.J.Fluss, S.B.Kaufman, C.E.Gross and E.P.Steinberg, Nucl. Instr. and Meth. **92** (1971) 381.

3) E.P.Steinberg, S.B.Kaufman, B.D.Wilkins and C.E.Gross, Nucl. Instr. and Meth. **99** (1972) 309.

4) E.C.Finch, Nucl. Instr. and Meth. **113** (1973) 41.

5) E.C.Finch, M.Asghar, M.Forte, G.Siegert, J.Greif, R.Decker and " Lohengrin Collaboration", Nucl. Instr. and Meth. **142**(1977) 539.

6) E.C.Finch, M.Asghar and M.Forte, Nucl. Instr. and Meth. **163** (1979) 467.

7) N.J.Hansen, Nucl. Instr. and Meth. **96** (1971) 373.

8) I.Kanno, Rev. Sci. Instr. **58** (1987) 1926.

9) I.Kanno, Rev. Sci. Instr. **61** (1990) 129.

10) S.Ramo, Proc. IRE, **27** (1939) 584.

G.Bertolini and A.Coche, "Semiconductor Detectors", North Holland, Amsterdam (1968).

11) H.W.Schmitt, W.M.Gibson, J.H.Neiler, F.J.Walter and T.D.Thomas, Proc. IAEA Conf. on the Phys. and Chem. of Fission, Saltzburg, (1965) 531.

12) P.A.Tove and K.Falk, Nucl. Instr. and Meth. **12** (1961) 278.

13) P.A.Tove and K.Falk, Nucl. Instr. and Meth. **29** (1964) 66.

14) N.J.Hansen, Progress in Nuclear Energy, vol. 4 (pergamon, Oxford, 1964).

15) K.Hata and H.Baba, JAERI-M 88-184 (1988).

16) J.F.Ziegler, J.P.Biersack and U.Littmark, "The Stopping and Range of Ions in Matter", Vol.1, Pergamon Press (1985).

17) T.Kitahara, H.Geissel, Y.Laichter and P.Armbruster, Nucl. Instr. and Meth. **196** (1982) 153.

THE ENERGY SPECTRA AND MEAN ENERGIES OF EMITTED FROM THE METALLIC ELEMENTS IRRADIATED BY ^{60}Co γ-RAYS.

MASAMOTO NAKAMURA AND YOH KATOH
Tokyo Metropolitan College of Allied Medical Sciences

1.INTRODUCTION

Many studies on mono-energy electron beam transmission through materials have been reported up to the present, but on the contrary, studies on the transmission of secondary electron produced in irradiated materials have rarely been carried out. It is thought that this is due to the prospect that all problems of electron transmission through materials can be resolved by applying results in the case of the above electron beam transmission, but the prospect is right only in principle. The problem of secondary electrons produced in irradiated materials has many physical and geometrical complexties which never arise in the case of the electron beam normally impinging against the material layer.

Within Gamma irradiated materials, the production points of secondary electrons are distributed in the whole parts of the materials, the movement directions of produced electrons have angular distributions and recoil electrons have energy distributions as in Compton's scattering. For such reasons, the infomation obtained in the case of the mono-energy electron transmission through materials can not be directly used in order to resolve the problem of secondary electrons produced in Gamma irradiated materials.

Because various applied fields using X-ray or γ-ray irradiation exist actually, the preparation of secondary electron data directly used in such applied fields is so important. The authors have then continued studying on secondary electron behaviors in materials and have keenly felt the need of the quantitative studies which are rarely carried out.

In this paper, the changes of the electron energy spectra with the sample thicknesses of a right element, Al, and a heavy

element, Pb, and the atomic number dependence of the mean energies of secondary electrons emitted from various elements with electron equilibrium thicknesses for the emitted electrons are reported, including the spectra of secondary electrons from the surfaces of various elements irradiated by ^{60}Co and ^{137}Cs γ-rays which have already been published.[1),2)]

2. EXPERIMENT

A sector type double focusing β-ray spectrometer was used for measurement of the energy spectrum of electrons emitted from the surface of the metallic element irradiated by γ-rays as showen in Fig. 1. Characteristics of the spectrometer were as follows. A reference radius ρ, a defrection angle Φ, distance between the source point and magnetic pole boundary t, dispersion D and magnification M were ρ=150mm, Φ=180°, t=280mm, D=4 and M=-0.61, respectively. The momentum spectrum measured with ^{137}Cs β-ray source was shown in Fig. 2. Gamma rays from a γ-ray source passed through a 100mm long lead collimetor, were incident perpendicularly upon the sample surface after penetration through a wall of the scattering chamber. Secondary electrons emitted from the chamber wall were eliminated by a small magnet placed between the wall and the sample. The small magnet was covered twic by μ metal so as to cut off magnetic stray field about the sample less than 5G.

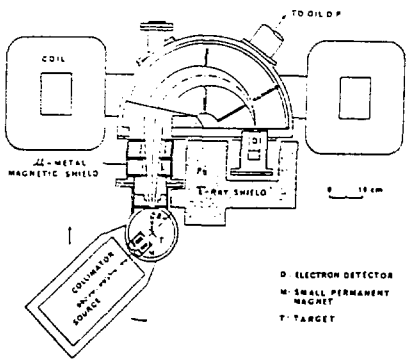

Fig. 1

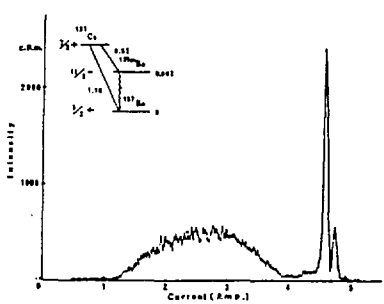

Fig. 2

The γ-ray beam area was given as $8 \times 13 mm^2$ by the lead collimetor attached to the wall side of the small magnet. The entrance slit of the spectrometer was a circular aperture which subtended 10° at a point on the sample. Therefore, if measurments of the energy spectra are made at each anglar step of 10° from γ-rays beam direction to 90° and the spectrum obtained was integrated over the energy and solid angle, the number of all electrons emitted forward from the sample surface is evaluated. For this purpose, the sample held at the sample position in the spectrometer was turned around the vertical axis in the sample holder togather with the beam system.

The quantity measured by a β-ray spectrometer is a momentum spectrum of electrons as shown in Fig. 2, so it is turned into the energy spectrum by using the well known relation of the momentum to the energy, in consideration of the width of the exit slit and the dispersion of the spectrometer. The intensity of the energy spectrum is then expressed by the number of electrons per energy width of one kev. Secondary electrons emitted from the baffles and the wall of the spectrometer irradiated by scattered γ-rays were measured under the condition of no sample as background and subtracted from the measured spectrum.

The exit slit width was determined to be $8 \times 10 mm^2$ in consideration of the γ-ray beam width on the sample and magnification of the spectrometer. A GM counter with $1.5 mg/cm^2$ thick mica window was used for an electron detector and its counting rate for electrons with the energy less than 95keV decreased and electrons below about 75keV could not be detected. The signals from the GM counter were recorded by a X-Y recorder after passing through an amplifier and a rate meter together with the intensity of magnetizing current of the β-ray spectrometer.

The energy resolving power of the β-ray spectrometer was 1.6% and the degree of vacuum was 6.7×10^{-3} Pa during this experiment.

Samples of C, Al, Cu, Mo, Sn, W and Pb were selected so as to cover the whole atomic number range of the elements and their thickness were chosen to insure secondary electron equilibrium in the sample irradiated by ^{60}Co γ-rays. In this experiment $R_{max} = 0.59$ g/cm^2.

Intensity of ^{60}Co γ-ray beam was determined by analysis of photopeak data obtained with the γ-ray spectrometer having a $1\frac{1}{2}$in. x1in. NaI(Tl) scintillation crystal, and intensity of 1.33MeV γ-ray beam was 1.99×10^{5} photons/cm^{2} · sec and that of 1.17MeV γ-ray beam is the same as the value for 1.33MeV γ-ray beam becuse of characteristics of ^{60}Ni nuclei for gamma decay. For the Cs source used, the activity was extremly high (20GBq), the beam intensity was then not measured.

3.EXPERIMENTAL RESULTS

Plate samples comprising C, Al, Cu, Mo, Sn, W and Pb were irradiated with Co -rays and the energy spectra of the secondary electrons forward emitted from each plate sample are shown in Fig. 4 and 5. The spectral intensity is represented as the number of electrons per photon and per 1keV width. Fig. 3 shows the energy spectrum of Al sample for each angle. In this figure, for each scattering angle, the energy of the Compton ricoil electron emitted at each angle by 1.33MeV γ-rays is shown by arrows. The spectra of an angle of 50°, 70° and 90° were omitted because these figures are complicated. Beyond an emission angle of 60°, most electrons are emitted at small angles from the atom

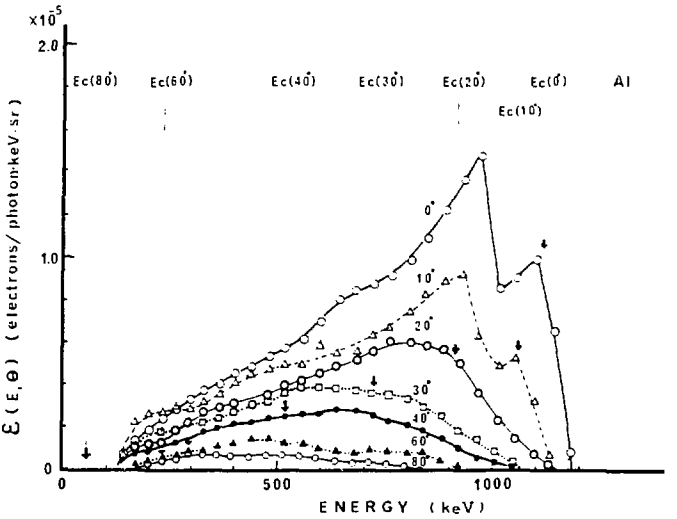

Fig. 3

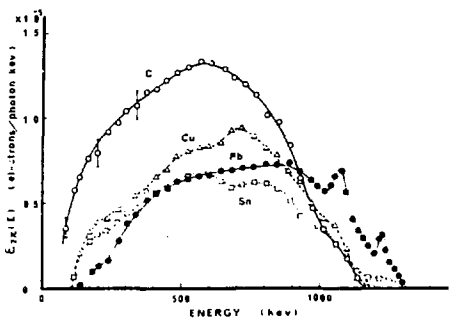

Fig. 4

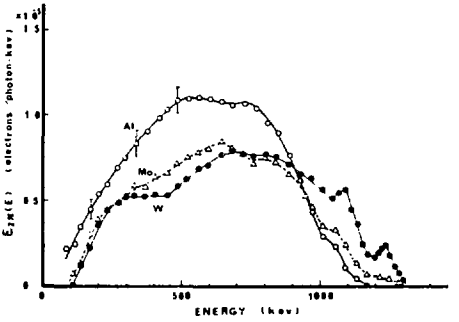

Fig. 5

by Compton scattering, and they reach the surface. Therefore, the emission angle of these electrons was shown to be greater than 60°. Fig. 6 shows the results for Al and Pb samples irradiated by the ^{137}Cs γ-rays. The sample thickness is 280mg/cm^2, which equals the maximum range of the photoelectron produced by 662keV γ-rays. In the irradiation by ^{60}Co γ-rays, the W and Pb samples, which have large Z values, show photo peaks. In contrast, in the irradiation by ^{137}Cs γ-rays, the Pb sample shows not only the peak for the K orbital electron but also for L orbital electron. When the sample thickness is the same as the maximum range of the emitted electron, a photo peak is observed. It can therefore be presumed that the shape of the spectrum does not change even if the sample thickness increases. The reason is that the secondary electron generated in a position deeper than the maximum range does not contribute to surface emission. However, it can be expected that, when tha sample thickness increases to the point where absorption of γ-rays cannot be neglected, the spectral intensity will decrease without any change in spectral shape. The contribution of the sample thickness to the energy spectrum was compared with the empirical formula[2], that is, the formula representing the quantum efficiency (number of electrons emitted by a photon) in the forward 2π direction with the thickness of the maximum range of

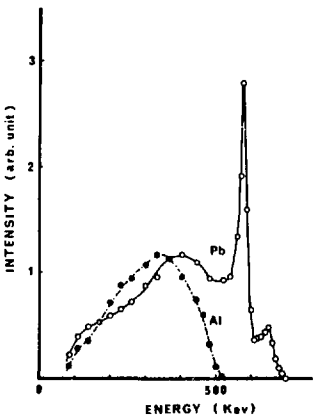

Fig. 6

the secondary electron, obtained by other workers.[3,4] The results were in good agreement.

For a sample of which the thickness differs from the electron equilibrium thickness, the spectrum was measured using 1mm thick (0.27g/cm²), 0.5mm thick (0.135g/cm²) and 0.3mm thick (0.081g/cm²) Al, and 0.22mm thick (0.24g/cm²) and 0.07mm thick (0.079g/cm²) Pb. The results are shown in Figs. 7 and 8.

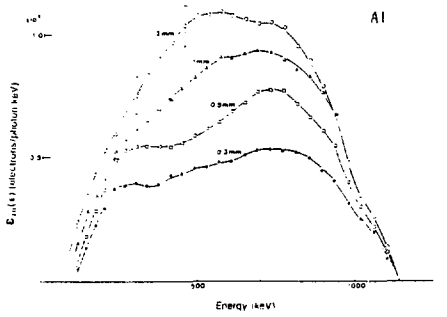

Fig. 7

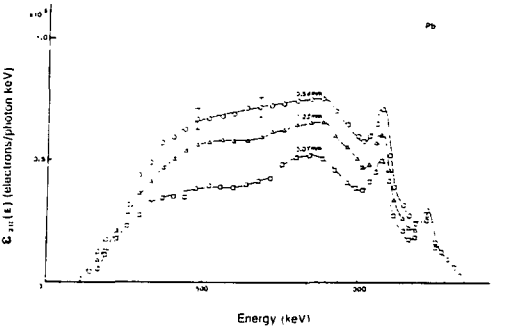

Fig. 8

When the sample thickness became thinner the spectral shape changed. The reason may be considered to be as follows; among all Compton electrons, the proportion of electrons that are multiply scattered and emitted from the surface at a large emissiton angle with decreasing energy decreases as the sample thickness becomes thinner. This result agrees with Minato's Monte Carlo calculation[3] within the range of error.

To estimate the effect of the recoil secondary electron, it is necessary to evaluate the ratio of the emitted electrons per incident photon, that is, the quantum efficiency of the recoil secondary electron and the mean energy of all the electrons emitted. We have already reported the quantum efficiency. In this paper, the mean energy is calculated using the energy spectrum (E) of the total forward-emitted secondary electron.

The mean energy <E> of the secondary electron is determined by the following formula if $\varepsilon_{2\pi}(E)$ is known.

$$\langle E \rangle = \frac{\int_0^{E\max} E \cdot \varepsilon_{2\pi}(E)\,dE}{\int_0^{E\max} \varepsilon_{2\pi}(E)\,dE}$$

In the calculation, the energy interval is divided and the divisional quadrature method is applied.

$$\langle E \rangle = \frac{\sum_i E_i \cdot \varepsilon_{2\pi}(E_i) \Delta E_i}{\sum_i \varepsilon_{2\pi}(E_i) \Delta E_i}$$

Over the whole range, the energy interval is divided into equal energy width (E), and the following equation is obtained.

$$\langle E \rangle = \frac{\sum_i E_i \cdot \varepsilon_{2\pi}(E_i)}{\sum_i \varepsilon_{2\pi}(E_i)}$$

The result of calculations and the quantum efficiency $\varepsilon_{2\pi}(Z)$ are shown in Table 1, and the dependence of the mean energy on atomic number is shown in Fig. 9. For the mean energy $\langle E \rangle$ of the surface-emitted secondary electron; in samples with an atomic number of Z up to 20, the value $\langle E \rangle$ increases as Z rises; in sample of $20<Z<50$, $\langle E \rangle$ virtually remains the same; and where $50<Z$, $\langle E \rangle$ increases again. Such behavior can be explained from the spectral shape for each sample. In the case of sample with small Z, such as C and Al, the secondary electron comes from Compton scattering, and the energy range of the emitted electron is from 0 to the Compton-edge. A characteristic of the energy spectrum in this region is that the low energy component decreases as Z rises. Accordingly, the mean energy increases with Z. In the case of $20<Z<50$, the secondary electron derived from the photoelectric effect is observed in the energy spectrum. However, the contribution of photoelectrons to the number of emitted electrons is extremely small, and it can then be considered that the Z^5 effect of the cross-section of the photoelectric effect is not important. Additionally, the shape of

Table 1

Element	C	Al	Cu	Mo	Sn	W	Pb
Atomic number	6	13	29	42	50	74	82
Thickness [g/cm^2]	1.01	0.54	0.45	0.72	0.58	0.58	0.62
Quauntum efficiency* ε_2 (Z) [Electrons/Photon]	9.4×10^{-3}	7.86×10^{-3}	6.23×10^{-3}	5.46×10^{-3}	5.23×10^{-3}	5.66×10^{-3}	6.20×10^{-3}
Mean energy [keV]	563.4	585.8	631.5	631.1	634.2	694.3	734.3

*from Reference 2

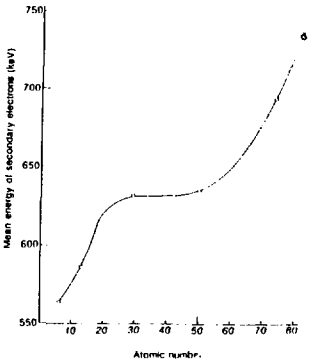

Fig. 9

the energy spectrum shows little change and then the mean energy is almost constant. In the case of 50<Z, the photoelectric peak gradually becomes noticeable and the above Z^5 effect is important. Consequently, it is considered that the high energy electron component increses with Z which results in an increase in mean energy.

In this study, the precision in detecting an electron below 100keV was low because of the difficulty in distinguishing it from the background. We intend to overcome this problem.

4.SUMMARY

The energy spectra and the mean energies of forward emission electron from Gamma ray irradiated metallic elements have been measured using a double focusing β-ray spectrometer. The Gamma ray sources used were ^{60}Co and ^{137}Cs.Sample measured were C, Al, Cu, Mo, Sn, W and Pb. Their thickness were chosen about equal to the maximum range of a 1.33MeV photoelectrons so as to ensure electron equilibrium.

The mean energies of secondary electron spectra for C, Al, Cu, Mo, Sn, W and Pb sample were 563, 586, 632, 631, 634, 694 and 734keV, respectively. The energy spectra have been measured for the Al and Pb sample of which the thickness differ from the electron equilibrium thickness for ^{60}Co γ-rays irradiation. When the sample thickness became thinner the spectral shape changed.

5.REFERENCE

1) M. Nakamura and B. Kikuchi, Jpn. J. Appl. Phys. 17, 1463 (1978)

2) M. Nakamura, J. Appl. phys. 54, 3141 (1983)

3) S.Minato, Radia. Res. 56, (1973) 1, Rept. Gov. Ind. Res. Nagoya 22, 23-45 (1973)
4) P. A. Ebert and A. F. Lauzon,IEEE Trans. Nuci. Ns-13, 735 (1966)

Si(Li) X-RAY SPECTROMETER ATTACHED TO ELECTRON MICROSCOPE COOLED BY LIQUID NITROGEN AT THE TIME OF USE

JEOL LTD E. Watanabe, M. Taira
INS Univ. of Tokyo K. Husimi

1. Introduction

There are following two key techniques in developing this spectrometer

(1) to obtain a stable Si(Li) detector with no degradation of chracteristics when keeped in a room temperature environment

(2) to evacuate residual out-going gases from the detector housing

The evacuation of gas has a practical importance for maintaining the detector stable. We have solved this problem by pumping out gases using the vacuum pumping system attached to the electron microscope before cooling the detector with liquid nitrogen.

Therefore, we will mainly discuss the problem of Li ion drifting pointed out by the above key technique (1).

2. Use of a high purity P type silicon crystal as the starting material

(1) Improvement of room temperature stability of the Si(Li) detector

It has been thought that degradation of characteristics of the Si(Li) detector is caused by thermal diffusion of Li ions. Based on this reason, we have thought that use of a high purity silicon is suitable to the starting material of the detector, which minimizes the amount of drifted Li ions in the detector.

We have found by using SEM that the Li drifted silicon is not intrinsic as believed up to now but N type material[1,3]. We have also found that a high resistivity P type silicon compensated by donor impurities such as residual phosphorous ions is not suitable for the starting material, because such donor impurities play a role of limiting factor of Li ion drifting[2]. This problem will be discussed in the following section.

(2) Lithium acceptor compensation and donor acceptor compensation

A high purity P type silicon is not always suitable for the starting material of Li ion drifting, if it contains much of donor impurities. This is understood as follows.

The impurity distribution and the electric field strength in the Li ion

compensated layer is shown in Fig. 1. With increase of Li drifted layer, the field intensity in front of the Li diffused surface become weak and finally it becomes zero. After arriving at this condition, no more Li ion drifting can proceed.

The donor concentration N_d' of the Li drifted region shown in Fig. 1 is supposed to be less than N_d of the starting material. This is due to the fact that a part of acceptor ions makes pairing with the nearest neighbour of donor ion, so that these acceptor ions can no more become partners of Li ion compensation.

Let us consider a sphere with a radius R around each donor as shown in Fig. 2. We assume that the negative charge of the acceptor contained in this sphere is neutralized by the positive charge of the residual donor located at the center of the sphere. The average number of acceptor contained in this sphere is $(4\pi/3)R^3N_a$, where N_a is the acceptor density of the starting material. If this value is less than 1, it means the probability that one sphere with acceptor is found in several spheres with out acceptor. Let us consider spheres with the radius R around all of the donors, then $(4\pi/3)R^3N_aN_d$ is the average number of acceptor which is found near the donor within the distance R. Donors are lost in amount of this value by this donor acceptor compensation. Then,

$$\begin{aligned} N_d' &= N_d - (4\pi/3)R^3N_aN_d \\ &= N_d \cdot \{ 1 - (4\pi/3)R^3N_a \} \\ &= N_d \cdot \phi(R, N_a) \end{aligned}$$

The survival rate of donor $\phi(R, N_a)$ is shown in Fig. 3 as a function of N_a. With increase of acceptor density N_a, the rate $\phi(R, N_a)$ becomes small and finally it vanishes when the acceptor density becomes $N_{a0} = 3/(4\pi R^3)$.

In the case that the acceptor density of the starting material is larger than N_{a0}, all of the donor ions are compensated by the acceptor ions. So that the Li drifted layer obtained by using such kind of silicon becomes intrinsic material.

On the other hand, in the case that the acceptor density of the starting material is lower than 10^{12}/cc, acceptor ions and donor ions are separeted by a distance of more than $10^{10\frac{2}{3}}$ lattice constant. There is no interaction between such acceptor ions and donor ions far separated each other, therefore Li ions make pairing with acceptor ions. The Li drifted layer becomes N type material caused by the remaining donor ions.

As the conclusion, it is important to use the material with low donor concentration when the high purity P type silicon is used as the starting material of the Li drifted silicon detector.

3 Degradation of vacuum caused by out-going gases in the detector housing

Out-going gases from the detector housing accumulate on the surface of the detector when it is cooled. This causes a lowering of the detector characteristics. Fig.4 shows an example of degradation of vacuum in the detector housing through sevsral temperature cycles.

4 Conclusions

(1) It has been thought that oxygen in silicon is the cause to hinder the drifting of Li ions, but this is completely overcome by the recent progress of the silicon purifying technique.

(2) We have found that the true cause of trouble in the Li ion drifting is the remaining donor such as impurity phosphorus in the material. This becomes eminent when a high purity P type silicon is used.

(3) We have obtained Li drifted silicon detector which does not degrade the characteristics even being stocked in a room temperature environment by using the high purity P type silicon.

(4) The Li drifted silicon detector thus obtained has a good energy resolution in a relative low bias voltage like 500V. This is the reason that we does not used the high purity silicon without Li drifting.

(5) The Li drifted layer has N type conductivity due to residual doner ions. A part of donor ions is thought to be compensated by acceptor ions contained enough in the P type material. But details of this donor-acceptor compensation are needed to be made clear.

(6) The out-going gas in the detector housing is evacuated by the vacuum pumping system attached to the electron microscope before cooling. by liquid nitrogen. This is another essential technique to realize the spectrometer cooled by liquid nitrogen only at the time of use.

References

1) E.Watanabe et al. IEEE Trans. Nucl. Sci. NS-35 p 33 (1988)

2) E.Watanabe et al. IEEE Trans. Nucl. Sci. NS-36 p177 (1989)

3) T.Miyachi, private communication

Figure captions

Fig. 1 Impurity and electric field distribution in a Li drifted layer

Fig. 2 A model of the donor-acceptor compensation

Fig. 3 Survival rate of donor as a function of acceptor density N_a

Fig. 4 Degradation of vacuum in a sealed off detector housing through up down temperature cycles

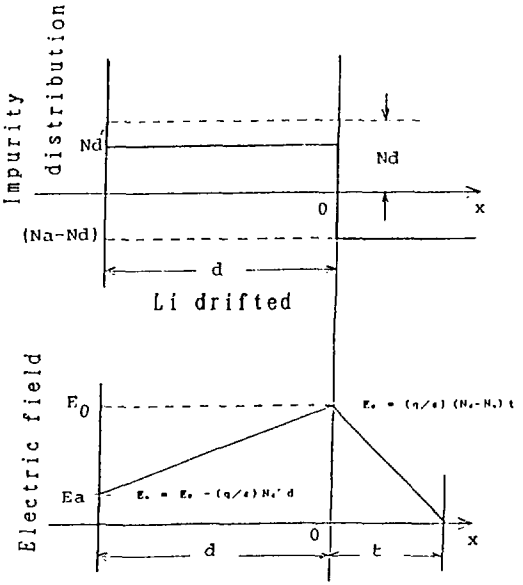

Fig. 1

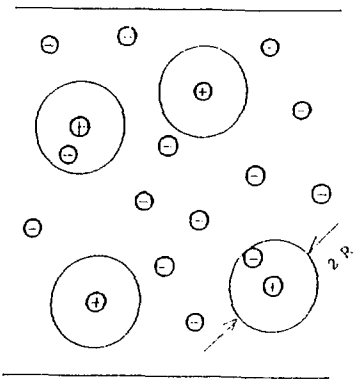

Fig. 2

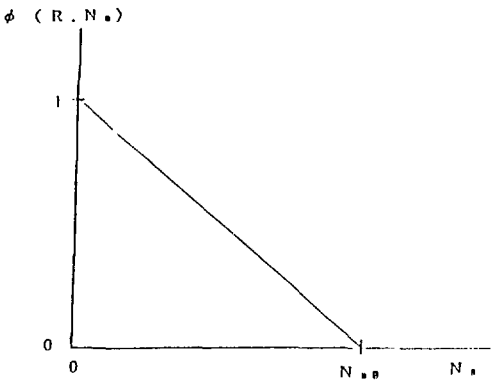

Fig. 3

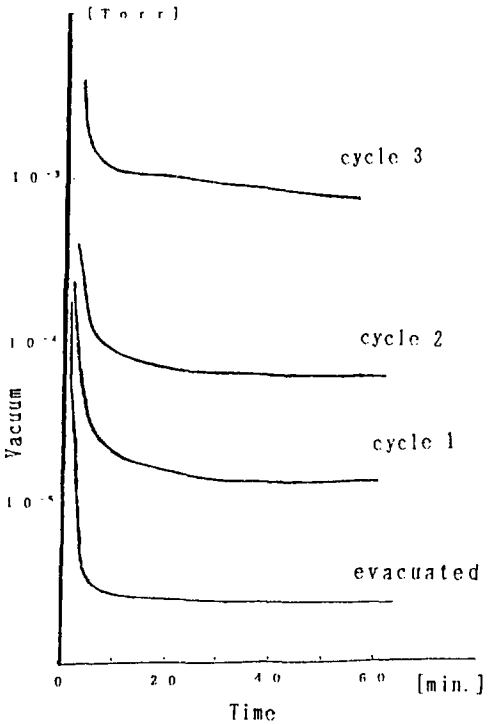

Fig. 4

DEVELOPMENT OF AN ELECTRONICALLY BLACK NEUTRON SPECTROMETER USING BORON-LOADED LIQUID SCINTILLATOR

Takahiko AOYAMA, Kiyonari HONDA and Chizuo MORI
Department of Nuclear Engineering, Nagoya University
Nagoya 464-01, Japan

Katsuhisa KUDO and Naoto TAKEDA
Electrotechnical Laboratory, Tsukuba, Ibaraki 305, Japan

1. INTRODUCTION

Energy measurement for ultra low-level neutrons requires the use of highly sensitive neutron detectors which can derive energy spectra directly from pulse height distributions without unfolding. One of the detectors would be the scintillation neutron spectrometer used by S.E. Jones et al.[1] to confirm the emission of 2.45 MeV neutrons from "cold nuclear fusion". Although they used the combination of organic scintillator /moderator and ^{6}Li-doped glass scintillator as the detector, the spectrometer devised by D.M. Drake et al.[2] using BC454 boron-loaded plastic scintillator would have a better energy resolution and a higher detection efficiency for the same detector size.

The present paper describes the development of an electronically black, totally absorbing neutron spectrometer using BC523 boron-loaded liquid scintillator as the detector. This spectrometer is expected to have a higher energy resolution than the BC454 scintillation spectrometer because of a higher light output and a larger hydrogen/carbon ratio of the BC523 scintillator.

2. PRINCIPLE AND METHODS

The detector used for the measurements is a 12.7 cm

diameter by 7.62 cm long liquid scintillator made of BC523 (Bicron Corporation) and coupled to a Hamamatsu R1512 photomultiplier tube (PMT). BC523 is a 5% natural boron-loaded liquid with isotopic abundances of 80.2% ^{11}B and 19.8% ^{10}B, resulting in a ^{10}B content of about 1% by weight. The density and hydrogen/carbon ratio of BC523 quoted by Bicron are 0.916 gm/cm^3 and 1.738, respectively. Its light output is 65% of anthracene, as compared to 48% for BC454 boron-loaded plastic scintillator[3].

The principle of the spectrometer is described as follows. A fast neutron that enters the detector can be quickly thermalized in a few nanoseconds, primarily by proton recoil interactions with the hydrogen in the scintillator, and produces a prompt signal that provide a measure of its initial energy. The thermalized neutron is finally captured by ^{10}B in the scintillator if it is not scattered away from the scintillator, emitting a definite size of light output by the reaction of $^{10}B(n,\alpha\gamma)^7Li$. Detection and measurement of the reaction products provide a second pulse that signifies the capture of a neutron. The time for the delayed capture occurs on a time scale of microseconds. Hence, if we practice height analysis for the prompt recoil pulse only when the delayed capture pulse with definite size appears, we can measure the total energy lost by a neutron through multiple elastic scattering, the energy of the incident neutron.

Figure 1 shows the schematic diagram of the spectrometer. Energy signal was derived from the dynode of the PMT and timing signal was from the PMT anode through built-in emitter-follower pre-amplifiers. Timing electronics consists of a fast filter amplifier that outputs to a single-channel analyzer (SCA) with energy window set to respond to the delayed capture signal generated by the reaction $^{10}B(n,\alpha\gamma)^7Li$ (about 60 keV effective electron energy in the liquid). The amplifier signal also is sent to a SCA operating with the integral mode that triggers a gate/delay generator used to define the width and the delay time of the coincidence gate pulse following the prompt recoil pulse. The delay time was adjusted not to generate coincidence signal for a single

event which triggers both SCAs. The SCA and gate/delay signals must be in coincidence to signify a valid neutron capture event in a given gate pulse width after the prompt signal. These valid signals were used to open the ADC gate and the prompt recoil pulses were height analyzed.

Neutrons for the measurement were obtained from a ^{252}Cf (50 μCi) isotopic source and from D(d,n)^{3}He reaction using Cockcroft-Walton type and Van de Graaff type accelerators in the standard irradiation field of the Electrotechnical Laboratory. The neutron spectrum from ^{252}Cf is essentially a continuum ranging to many MeV, and neutrons generated from accelerators were monoenergetic from 2.4 to 5.0 MeV. For runs with the ^{252}Cf source, since the liquid is also sensitive to γ-rays, a lead shield of 10 cm was interposed between the source and the detector to reduce the intence γ flux from the source. For all the measurements, the neutrons were directed along the axis of the detector, normal to the surface opposite the PMT.

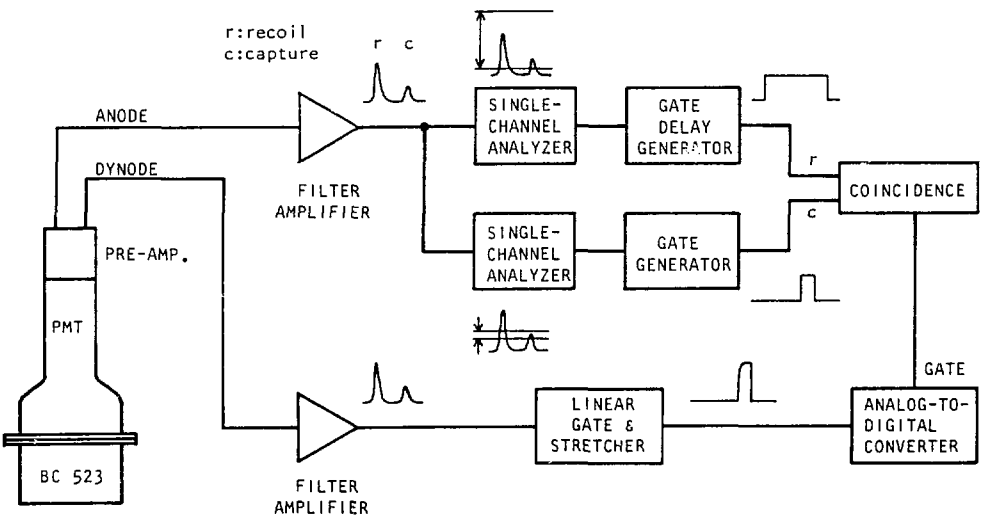

Fig. 1. Schematic diagram of the neutron spectrometer.

3. CHARACTERISTICS AND PERFORMANCE

3.1. MEAN CAPTURE LIFETIME

The primary function served by the boron in BC523 is to provide a detectable signal for nearly thermalized neutrons. The cross section for $^{10}B(n,\alpha\gamma)^{7}Li$ follows a 1/v law for neutron energy $E \lesssim 200$ keV. The resulting absorption probability is therefore exponential with time constant,

$$\tau = (N \sigma v)^{-1}, \qquad (1)$$

independent of neutron energy. Here N is the number density of ^{10}B nuclei in BC523 scintillator, $\sigma \propto v^{-1}$ is the cross section for $^{10}B(n,\alpha)^{7}Li$, and v is the speed of the neutron. Evaluating eq.(1) using $N=5.29\times10^{20}cm^{-3}$, $\sigma=3837\times10^{-24}cm^{2}$ at $v=2.200\times10^{5}cm\ s^{-1}$, we obtain $\tau=2.24$ μs.

Time dependence of delayed capture pulse after prompt recoil pulse was measured using the ^{252}Cf source. The data were acquired in 0.67 μs time bins for delays of prompt pulses from 1 to 9 μs. The result of the measurement, shown in Fig. 2, was obtained by subtracting a constant component by accidental coincidence which was independent of the delay time. Figure 2 reveals that coincidence counting rate decreased exponentially with delay time with a time constant of 2.20 μs, which was consistent with the calculated mean capture lifetime of 2.24 μs.

The measured value of the mean capture lifetime can be used to determine an optimum width of the coincidence gate pulse. The width should be kept as small as possible to minimize accidental coincidence counting rate. On the other hand, the width should be large enough to obtain a large neutron detection efficiency. Since delayed capture pulses of 90% and 99% appear in 2.3 and 4.6 times the mean capture life time respectively, the optimum width for coincidence gate pulses might be selected between these times considerating the intensity of background γ-rays. Setting the gate pulse width at 8.33 μs, i.e. 3.8τ, as an example, we obtained an

accidental coincidence rate of 0.14 cps for background γ-rays in our laboratory without any γ-shielding, which was 7.6×10^{-4} times smaller than the background counting rate of 180 cps observed with the same detector without coincidence operation.

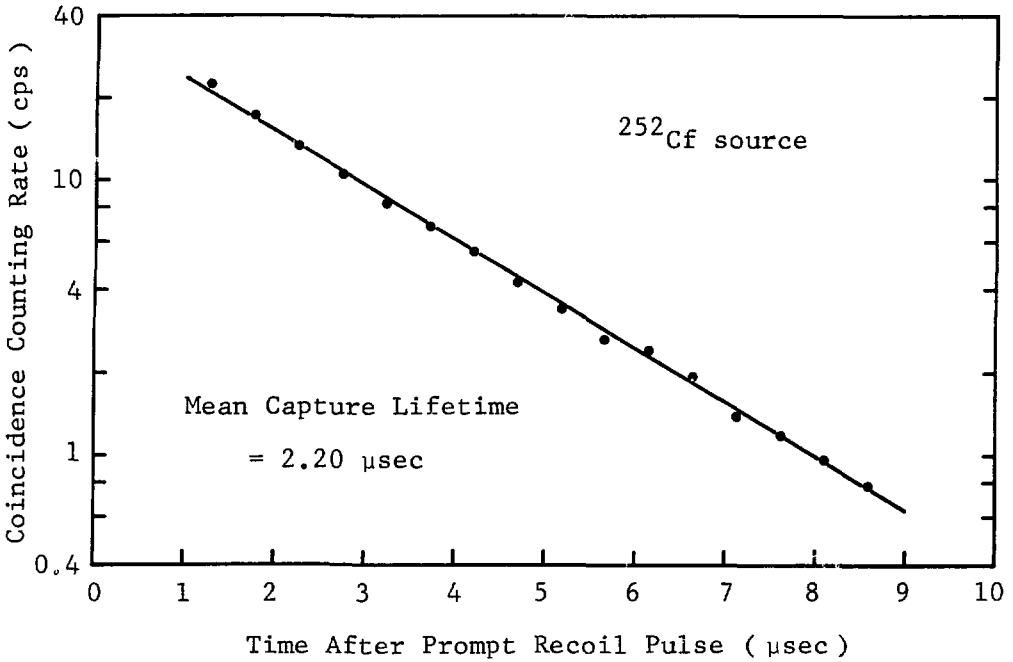

Fig. 2. Time dependence of delayed capture pulse.

3.2. NEUTRON ENERGY RESPONSE

Pulse height distributions for monoenergetic neutrons and for neutrons from the ^{252}Cf source were measured setting the coincidence gate pulse width at 8.33 μs.

Figures 3(a) and 3(b) show pulse height distributions for 2.4 and 5.0 MeV monoenergetic neutrons respectively. It is seen from these figures that the distributions for monoenergetic neutrons did not have single peaks as would be expected but had double peaks. This might be attributed to the difference of light output by recoil protons whether total energy is lost by a single elastic collision or by multiple scattering.

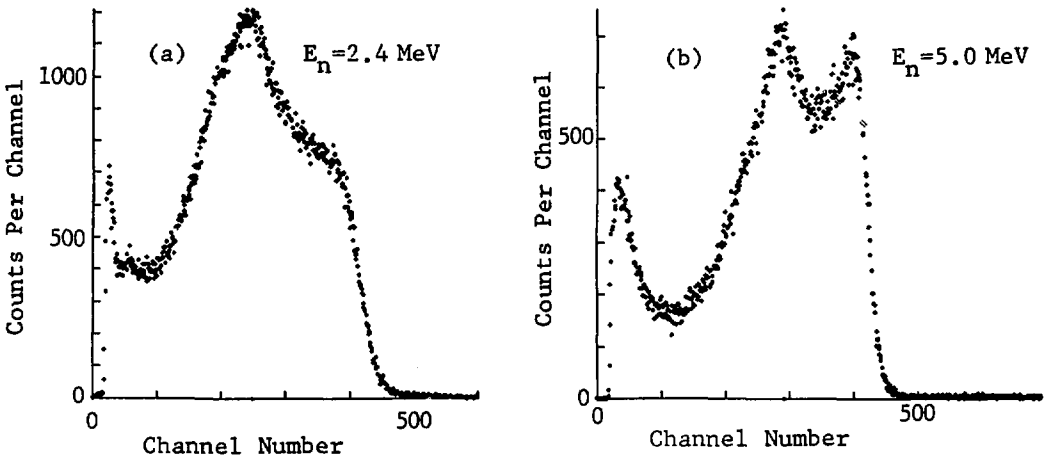

Fig. 3. Pulse height distributions for (a) 2.4 and (b) 5.0 MeV monoenergetic neutrons.

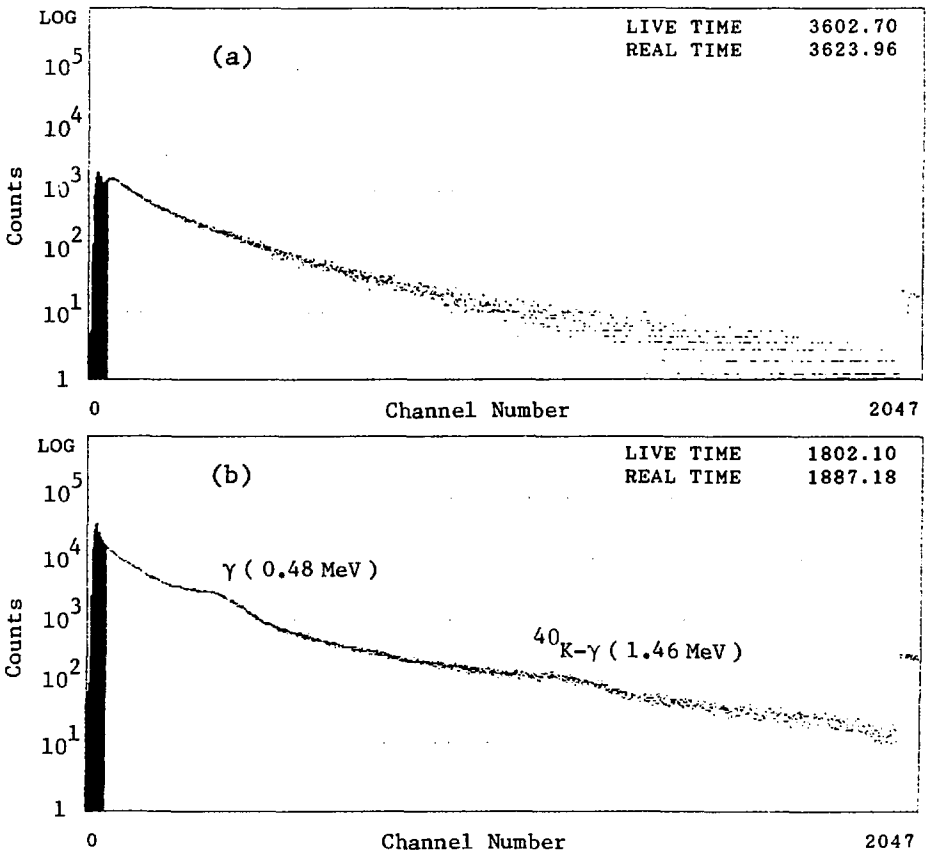

Fig. 4. Pulse height distributions for a ^{252}Cf neutron source obtained (a) with and (b) without using the ADC gate.

Low-energy upturns of the main peaks in Figs. 3(a) and 3(b) could be explained by the existence of low energy secondary neutrons and by accidental coincidence of fractionary energy loss events. Intrinsic efficiencies of the neutron spectrometer for monoenergetic neutrons were measured to be 2.9% and 1.2% for 2.4 and 5.0 MeV neutrons respectively.

Figures 4(a) and 4(b) show pulse height distributions for the ^{252}Cf source, where Fig. 4(b) was obtained without using the ADC gate as in Fig. 1. In Fig. 4(a), we can find neutron energy spectrum as expected for ^{252}Cf [4], while in Fig. 4(b), Compton edges by γ-rays emitted from neutron capture reaction by ^{10}B (E_γ=482 keV) and from environmental ^{40}K (E_γ=1.46 MeV) were observed. Since the detection efficiency decreased with increasing neutron energy, and considerable secondary neutrons entered into the detector, observed counts in Fig. 4(a) decreased more rapidly than the exponential decrease with increasing neutron energy.

4. CONCLUSIONS

We developed an electronically black neutron spectrometer using boron-loaded liquid scintillator BC523.

Pulse height distributions obtained for monoenergetic neutrons were slightly complicated having double peaks. The present spectrometer, however, might be possible to derive neutron energy spectra without unfolding from pulse height distributions for the case where strict energy spectra are not required as for low-level environmental neutron measurements.

REFERENCES

1) S.E. Jones, E.P. Palmer, J.B. Czirr, D.L. Decker, G.L. Jensen, J.M. Thorne, S.F. Taylor and J. Rafelski, Nature 338(1989)737.

2) D.M. Drake, W.C. Feldman and C.Hurlbut, Nucl. Instr. and Meth. A247(1986)576.

3) E.A. Kamykowski, Nucl. Instr. and Meth. A299(1990)105.
4) G.F. Knoll, Radiation Detection and Measurement, 2nd ed. (Wiley, New York, 1989) p.21.

AN IMPROVEMENT IN LOCATING THE COMPTON EDGE IN THE PULSE HEIGHT SPECTRA OF ORGANIC SCINTILLATION DETECTORS

Mikio YAMASHITA
Electrotechnical Laboratory

INTRODUCTION

The Compton edge, which is the characteristic pattern appearing in the pulse height spectrum in measuring gamma-rays with organic scintillation detectors such as plastic and liquid scintillation detectors, can represent the energy of gamma-rays of interest, and therefore is conveniently used as a reference point to calibrate the pulse height in terms of energy, as it is often referred to as energy calibration of pulse heights. However, since the Compton edge is always smeared to a varying degree depending upon the inherent scintillation efficiency and the energy resolution of the measuring system, it has been a longstanding problem to determine its position with an uncertainty of much less than a few precent in relevant experiments in which high-accuracy energy calibration of pulse heights is of essential importance. In this connection, we have long before proposed a novel method of locating the Compton edge in the pulse height spectrum that is based on deconvolution of the measured spectrum, along with a brief review of existing methods to treat the problem.[1]

The new method relies on the idea that the very feature of step edge which the Compton adge would originally have possessed could be extracted from the measured pulse height spectrum by carrying out a series of deconvolutions with appropriate Gaussian functions assumed to allow energy resolutions.

However, from a practical point of view, the method has

awaited further improvements,especially with respect to the algorithm to allow the deconvolution to be accurately and efficiently carried out. Fortunately, with the advent of low-cost but high-performance personal computers in the past few years, it has become possible to implement the necessary deconvolution with reasonable accuracy on a personal computer.

This paper aims to demonstrate a recent progress in the relevant algorithm primarily developed for personal computers, along with some examples of deconvoluting the pulse height spectra.

ANALYSIS BY THE DECONVOLUTION METHOD

1.Principle

The measured pulse height spectrum g(E)is expressed in terms of convolution integral between the energy loss spectrum f(E) of Compton electrons in the scintillator and the resolution function R(E) as follows.

$$g(E) = \int_0^{E_{max}} f(T)\ R(E-T)dT \qquad (1)$$

Here, E_{max} is the maximum energy in the energy loss spectrum, which is taken as corresponding to the energy of the Compton edge E_c as long as the scintillator is small enough to permit multiple scatterings of gamma-rays to be neglected. And the resolution function may be described as a Gaussian function, while the real energy resolution is hard to determine and therefore remains unknown.

However, since a number of statistical processes are assumed to be responsible for the observed line-broadening effect, the energy resolution R_0 might be expressed as a quadratic sum of the resolutions R_i $(i=1,2,\cdots,m)$ of the individual processess as

$$R_0^2 = R_1^2 + R_2^2 + R_3^2 + \cdots\cdots + R_m^2 \qquad (2)$$

And the hypothetical pulse height spectra to be observed after each of the statistical processes could be described as folows.

$$g_1(E) = \int_0^{E_{max}} f(T)\ R_1(E-T)dT \qquad (3)$$

$$g_2(E) = \int_0^{E_1} g_1(T)\ R_2(E-T)dT \qquad (4)$$

$$g_3(E) = \int_0^{E_2} g_2(T)\ R_3(E-T)dT \qquad (5)$$

- - - - - - - - - - - - - - -

$$g_m(E) = \int_0^{E_{m-1}} g_{m-1}(T)\ R_m(E-T)dT. \qquad (6)$$

Here $E_1, E_2, \ldots, E_{m-1}$ are the upper limits of energy of the spectra $g_1(E), g_2(E), \ldots, g_{m-1}(E)$, respectively, while $g_m(E)$ is equivalent to the measured spectrum.

Each statistical process involved in these equations may be arbitrarily chosen, provided they fulfill on the whole the condition of Eq.(2). Therefore, carrying out deconvolution of Eqs.(3) through (6) one by one starting with Eq.(6) with particular values assigned to the energy resolutions, one can expect the deconvoluted spectra $g_{m-1}(E)$, $g_{m-2}(E)$ to get closer and closer to the original spectrum $f(E)$. From a practical point of view, as the deconvoluted spectra have been deconvoluted one after another to the extent where they involve the energy resolutions of less than a few percent, we could regard with a high level of confidence the pulse height (in terms of channel number) corresponding to half the height of the apparent Compton edge as indicating the true Compton edge.

2. Implementation of Deconvolution

In earlier prlication[1] we described some examples of deconvoluting the pulse height spectra by the conventional

deconvolution method[2] based on successive approximation. With this method, the deconvoluted spectra often exhibit harmonic oscillations and negative distributions, strongly depending on the statistical nature involved in the raw data, and therefore the final results have proved less satisfactory. This difficulty, however, can be overcome to a considerable extent by carrying out the deconvolution using a successive approximation method that meets the constraint of non-negativity.

Assuming the pulse height spectrum given in the range from 1 to n channels, Eq(1) is rewritten in a discrete form as follows.

$$G(E_i) = \sum_j R_{ij} F(E_j), \quad (i=1,n;\ j=1,n) \qquad (7)$$

Then if Eq(7) is expressed in the form of matrix as $\mathbf{G}=\mathbf{RF}$, the deconvolution is carried out according to the following procedures[3]:

$$\text{1st Approximation: } \mathbf{F}_1=\mathbf{G}_0=\mathbf{G}, \text{(Measured Spectrum)} \qquad (8)$$

$$\text{kth Approximation: } \mathbf{F}_k=\mathbf{F}_{k-1}\ (\mathbf{G}_0/(\mathbf{RF}_{k-1})) \qquad (9)$$

Here the resolution function R is a Gaussian function as defined by the following equation.

$$\mathbf{R} = R_{ij} = A_j \exp\{-5.546(i-j)^2/(2R^2j^2)\}, \qquad (10)$$

$$(i=1,n;\ j=1,n)$$

where A_j is the normalization constant, R the energy resolution in terms of percent/100.

This method of deconvolution allows the deconvoluted spectrum to converge to an almost constant spectrum with successive approximations of k=10 15. With a modern personal computer like the one of PC-9801 type, the necessary calculations for a single convolution could be completed within an hour or so.

EXAMPLES OF ANALYSIS

Fig.1 shows a pseudo-Compton pulse height spectrum of 0.66 MeV gamma-rays (R=0.4;Spectrum A)and the deconvoluted spectrum (Spectrum B),together with the original unsmeared spectrum (Spectrum C). It is seen that the position corres ponding to half the height of the Compton peak in Spectrum B coincides with the Compton edge in Spectrum C.

Fig.2 shows a theoretical pulse height spectrum with no statistical broadening of 1.275 MeV gamma-rays to be measured with a 25 mm dia.x 5 mm plastic scintillator (Spectrum C),the same spectrum but with an energy reso- lution of 40 % (Spectrum B). It is shown that there is a good agreement between the position of half the Compton peak height and the original Compton edge.

Fig.3 shows a measured pulse height spectrum of 0.662 MeV gamma rays with a 12 mm dia.x 30 mm NE102A plastic scintillator (Spectrum A),and a deconvoluted spectrum (Spectrum B). It is possible to calibrate the pulse height in terms of absolute energy on the assumption that the position of half the Compton-peak height in Spectrum B represents the true Compton edge, and then evaluate the absolute amount of energy absorbed in the scintillator. On the other hand, we can experimentally determine the absorbed energy in the scintillator by the completely different method which we have recently developed.[4][5] A comparison, therefore, was made between the total ab- sorbed energies evaluated by the two different methods,and it is found that there is a good agreement between them.

This result of comparison should imply that the energy calibration of pulse height based on taking the position of the half the Compton-peak height in Spectrum B as the Compton edge is reasonably accurate.

CONCLUDING REMARKS

From the results of these and other experiments, we are

inclined to conclude that, with organic scintillators of such a small size that multiple scattering of gamma-rays is insignificant,the Compton edge in the pulse height spectrum can be accurately located by the described method with an uncertainty of one percent or less.

REFERENCES

(1) M.Yamashita, Ionizing Radiation 8(3), 115(1981).
(2) A.F.Jones and D.L.Misell, J. Phys. A3, 462(1970).
(3) J.F.Mollenauer, University of California Lawrence Radiation Laboratory Report UCRL-9748(1961).
(4) M.Yamashita, KEK Report 90-11, Proc. 5th Workshop on Radiation Detectors and Their Uses p140(1990)
(5) M.Yamashita, Rev. Sci. Instrum. 61, 2255 (1990).

Fig.1 Pseudo-Compton pulse height spectra of 0.66 MeV gamma-rays(R=0, 0.4) and the deconvoluted spectrum.

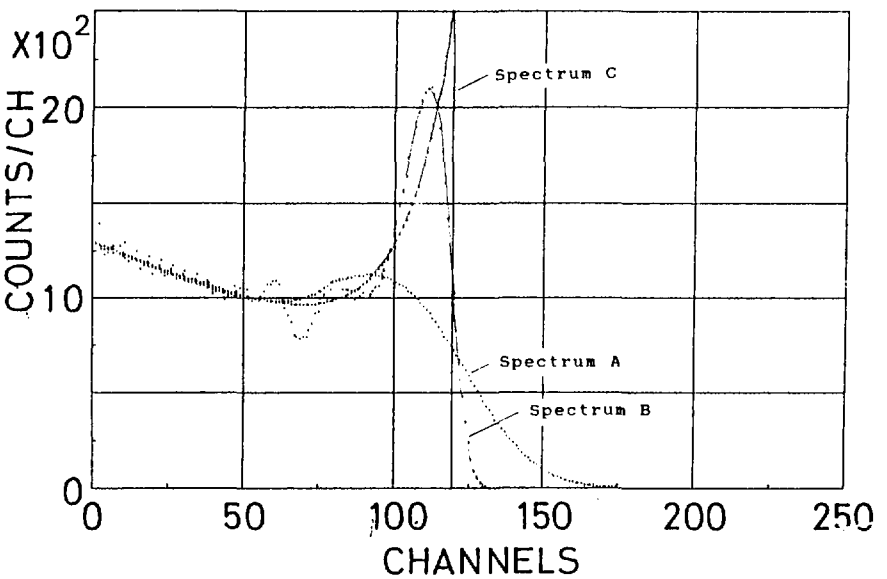

Fig.2 Monte Carlo-calculated pulse height spectra of 1.275 MeV gamma-rays (R=0,0.4) with a 25 mm dia x 5 mm plastic scintillator,and the deconvoluted spectrum.

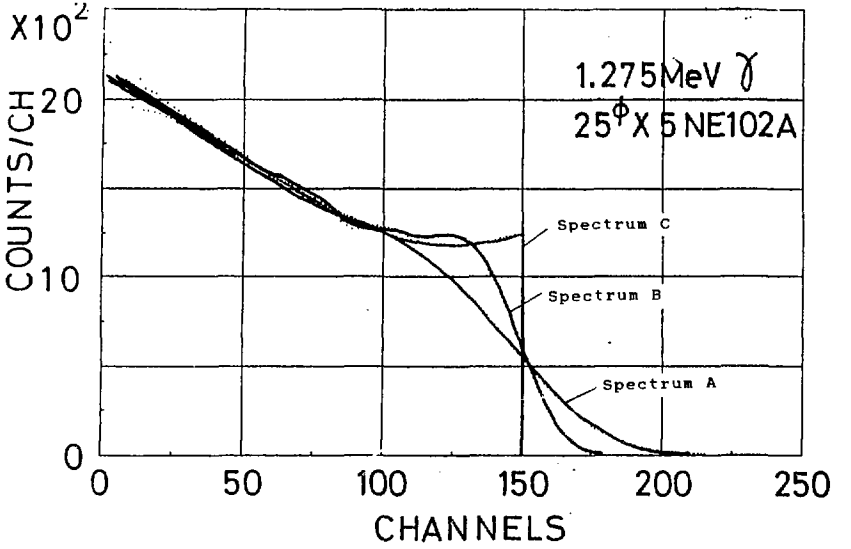

Fig.3 Measured pulse height spectrum of 0.662 MeV gamma-rays with a 12 mm dia x 30 mm plastic scintillator, and the deconvoluted spectrum.

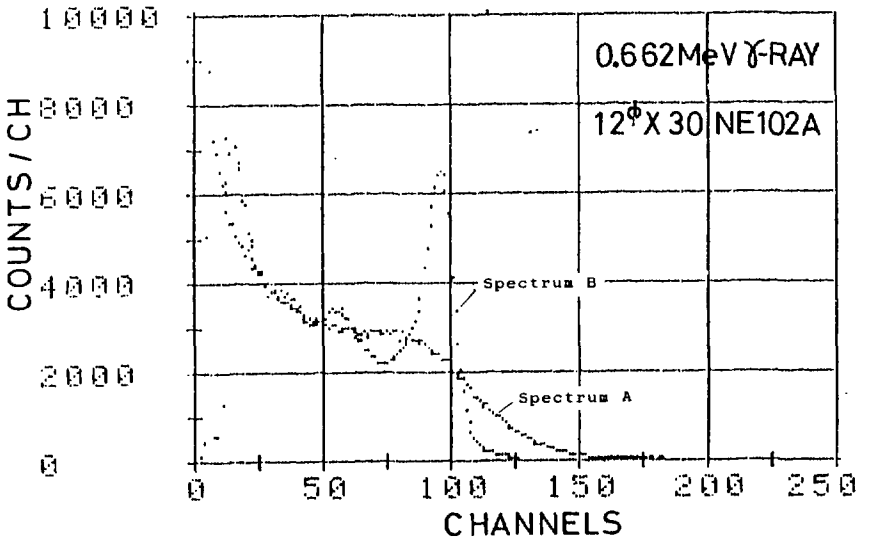

DETECTION OF TRACE AMOUNTS OF SPONTANEOUSLY FISSIONING NUCLIDES BY MEASURING TIME INTERVALS BETWEEN DETECTION PULSES

H. Gotoh, M. Haruyama, T. Kawamura and M. Takase
Japan Atomic Energy Research Institute
Tokai-mura, Naka-gun, Ibaraki-ken, 319-11, Japan

1. INTRODUCTION

Wastes from reprocessing process emit neutrons through spontaneous fissions or through (α,n) reactions. A great part of spontaneous fissions emits plural number of neutrons, whereas all (α,n) reactions emit single neutrons. This difference of neutron emission gives us a means of separating these two reactions. The method utilising this nature is called "passive neutron method".

The authors made a large scale of detection system which can accommodate a 200ℓ drum and conducted a series of experiment utilising simulated drums of reprocessing wastes. Here we introduce the detection system and the method of detection, report the outline of experimental results and discuss the results from physics view point.

2. DETECTION SYSTEM

Figure 1 shows the bird's eye view of the detection system constructed by the authors.[1] A space of 65cm×65cm×100cm is surrounded by a wall of graphite with 30cm thickness and then by a wall of polyethylene with 10cm thickness. The graphite wall moderates neutrons emitted from the specimen placed in the chamber. The polyethylene wall reflects back the thermal neutrons moderated in the graphite wall. Forty ^{3}He proportional counters of

25mm diameter and of 1,000mm length containing 4 atm. ^{3}He gas were arranged in the graphite wall equally spaced.

3. DETECTION METHOD

The method, which the authors adopted, measures all the time intervals between neutron detection pulses and differs from those used widely. This method collects the maximum information, contained in data taken with a multi-channel type data accumulation system, useful to discriminate between fission neutrons and (α,n) neutrons.

He-3 counters were operated at a voltage a little higher than the recommended value. Outputs from He-3 counters were differentiated and integrated with small time constants by preamplifiers. These realised a smaller resolving time of 350ns.

Figure 2 shows an example of distribution of time intervals taken for ^{240}Pu.[1] These data are analysed into a sum of two exponential distributions. Experience teaches us that data are represented by an exponential distribution when neutrons are emitted only by (α,n) reactions and that data are analysed into two or three exponential distributions when some part of neutrons are supplied by fission. Here we shall call the integrated count of the exponential distribution with the largest time constant "random count", (the sum of) the integrated count(s) of exponential distribution(s) except the distribution with the largest time constant "coincidence count", and the sum of these two counts "total count". The neutron detection efficiency is obtained by dividing the difference between the total count and the background count by the product of the counting time and the neutron emission rate.

4. EXPERIMENTAL RESULTS

Several kinds of non-radioactive materials were chosen to simulate wastes produced in the reprocessing process of spent fuel. Specimens of 200ℓ drum size were fabricated using these materials. Specimens were made disintegrable to insert radioactive samples into reserved positions in drums. The neutron detection efficiency was calculated by obtaining random counting rates and coincidence counting rates for various locations inserting spontaneously fissioning sources like plutonium produced in the reprocessing process of light water reactor spent fuel. Neutron detection efficiency for homogeneously containing wastes was calculated by integrating these neutron detection efficiencies. The detection limits of radioactivity for various matrices were calculated by using these neutron detection efficiency.

The neutron detection efficiency for a neutron source placed in the center of the measuring chamber without any matrix was about 16%.[1] The experimental results of the neutron detection efficiency for a neutron source placed in a drum filled with light water will be mentioned in the next section.

5. DISCUSSIONS

The authors are endeavoring in detailed analysis in order to generalize the experimental results obtained. Here we introduce some results obtained already.

(1) CALCULATION OF NEUTRON DETECTION EFFICIENCY WITH THE MONTE CALRO METHOD

The neutron detection efficiency for a neutron source placed in a 200ℓ drum filled by water was measured using a ^{252}Cf neutron source of about 2μCi. Table 1 lists the experimental results. The table also lists the calculated results by a Monte Carlo program MCNP with the fractional standard deviations. Figure 3 compares the experimental results and the calculated ones. Both results satisfactorily agreed with each other.

(2) RELATION BETWEEN COINCIDENCE COUNTING EFFICIENCY η AND NEUTRON DETECTION EFFICIENCY ε

Suppose that one spontaneous fission which emits ν neutrons was taken place and that n neutrons among ν were detected ($2 \leq n \leq \nu$), then $n-1$ coincidence counts would be recorded. If we denote the neutron detection efficiency by ε and the probability that one spontaneous fission emits ν neutrons by $f_\nu (0 \leq \nu \leq \nu_{max}; \Sigma f_\nu = 1)$, then we get the relation:

$$\eta = \sum_{\nu=1}^{\nu_{max}} [f_\nu \{\nu \varepsilon - 1 + (1-\varepsilon)^\nu\}] . \qquad (1)$$

Figure 4 compares the experimental results and the calculated results using the relation (1) for ^{252}Cf and ^{240}Pu. We used the f_ν values in reference 2). The experimental results on ^{240}Pu agreed very well with the prediction of eq.(1). Although those on ^{252}Cf agree well with the prediction in the low efficiency region, those exceeded the prediction in the high efficiency region. This discrepancy is discussed in the next section.

(3) CALCULATION OF THE DISTRIBUTION OF DETECTION TIME INTERVALS

We can calculate the distribution of time intervals between detection pulses, if we get the probability $\neg p(t)$ that the next detection pulse does not arrive by the time t ($0 \leq t$). The distribution can be compared directly with experimental data. The distribution $\neg p(t)$ is derived under the assumption that the life of neutrons is given by an exponential distribution with an average value τ:

$$\neg p(t) = \exp\left\{-t\left(r_r \varepsilon + r_f \left[1 - \sum_{\nu=0}^{\nu_{max}} \{f_\nu (1-\varepsilon)^\nu\}\right]\right)\right\} \times$$
$$\times \exp\{r_r \tau \varepsilon (1 - e^{-t/\tau})\} \times$$
$$\times \exp\left(r_f \tau \sum_{\nu=1}^{\nu_{max}} \left[f_\nu \sum_{i=1}^{\nu} \{{}_\nu C_i \, (1-\varepsilon)^{\nu-i} \, \varepsilon^i \, \frac{1}{i} (1 - e^{-it/\tau})\}\right]\right) \times$$

$$\times \left(Q_0 + \sum_{j=1}^{\infty} [Q_j \{1 - \varepsilon (1 - e^{-t/\tau})\}^j]\right), \qquad (2)$$

where $Q_j (j=0,1,\cdots)$ are the distribution of the number of neutrons remaining in the system immediate after the time a detection pulse was registered ($\sum Q_j=1$). The distribution Q_j can be obtained by solving a system of recursive relation. The variables r_r and r_f are respectively the emission rate of (α,n) neutrons and the spontaneous fission rate. Although the expression (2) seems complex, calculation shows the distribution can be fitted by a sum of at most three exponential functions.

In Fig. 5, the prediction curve calculated by eq.(2) is drawn with the experimental data and the prediction curve by eq.(1). The former prediction fits the experimental data in the whole range. In the derivation of eq.(1), it is assumed that the counting rate of random counts is adequately smaller than the inverse of the thermal neutron dieaway time of the system. The counting rates for the ^{252}Cf source(about 2μCi) in the high efficiency region were comparable with the inverse of the dieaway time of 900μs.

REFERENCES

1) H. Gotoh et al, NEACRP-A-1079(1990)

2) E. Norman et al, BNL-NCS-35513(1985)

TABLE 1 Detection Efficiency of Neutrons Emitted in Water

Distance from the Center (cm)	Detection Efficiency of Neutrons		
	Experiment	Calculation	Fractional Standard Deviation (%)
0	0.0062	0.0054	7.0
2	0.0064		
4	0.0069	0.0060	6.7
6	0.0079		
8	0.0096	0.0082	6.1
10	0.0122		
12	0.0157	0.0139	4.4
14	0.0209		
16	0.0280	0.0250	3.2
18	0.0385		
20	0.0514	0.0490	2.4
22	0.0689		
24	0.0851	0.0807	1.8
26	0.1030		
28	0.1079	0.1110	1.6
30	0.1129		
32	0.1129	0.1114	1.5

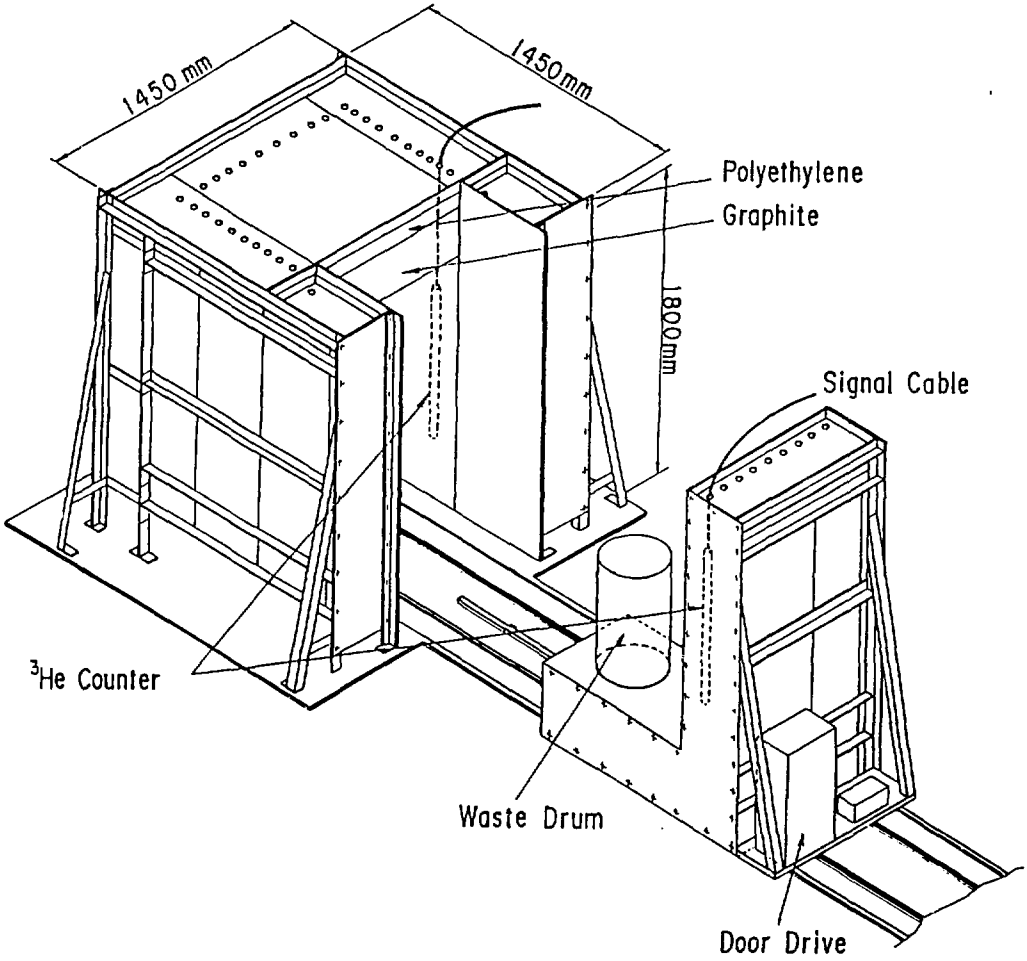

Fig.1 A Bird's Eye View of the Detection Assembly for the Passive Neutron Method

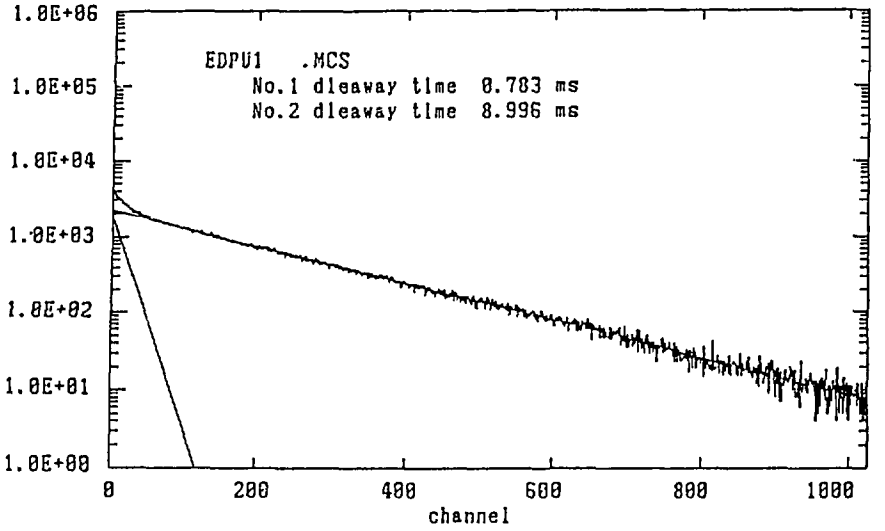

Fig.2 Time Interval Spectrum and Its Analysis into Two Exponential Functions

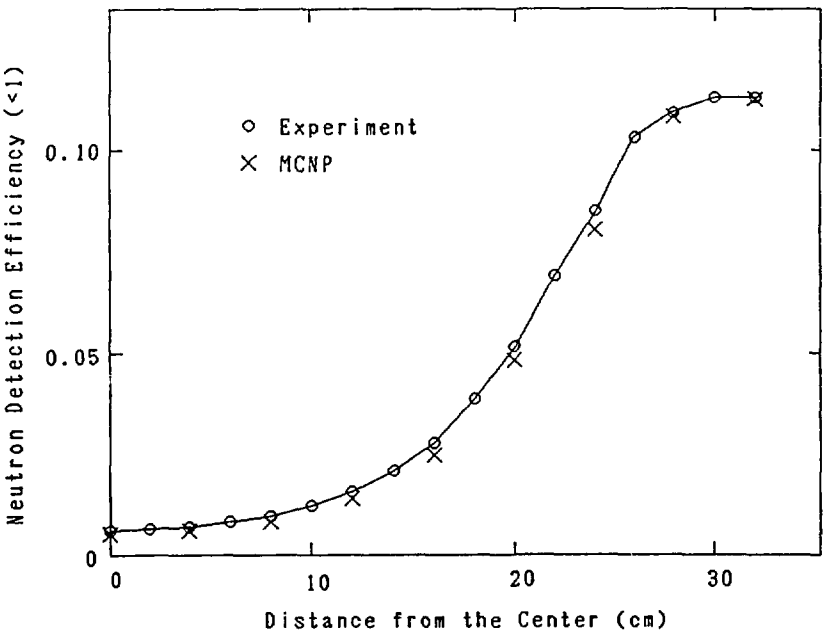

Fig.3 Neutron Detection Efficiency for a Cf-252 Source in a 200ℓ Drum Filled with Light Water

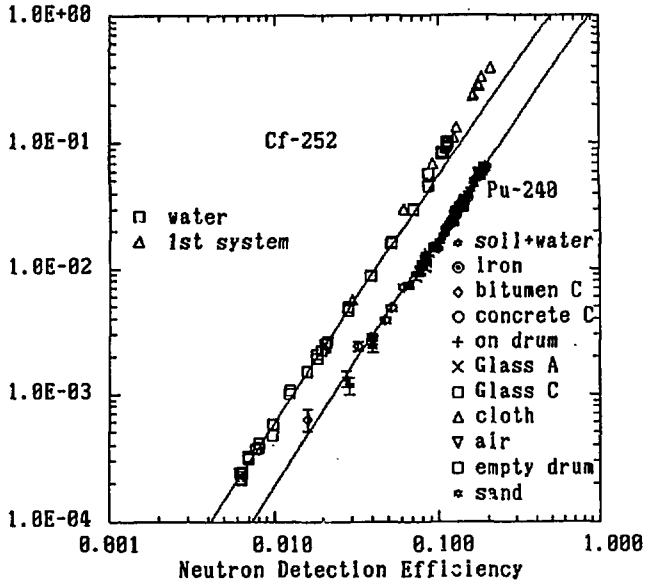

Fig.4 A Scatter Diagram of Coincidence Counting Efficiency vs Neutron Detection Efficiency for Pu-240 and Cf-252

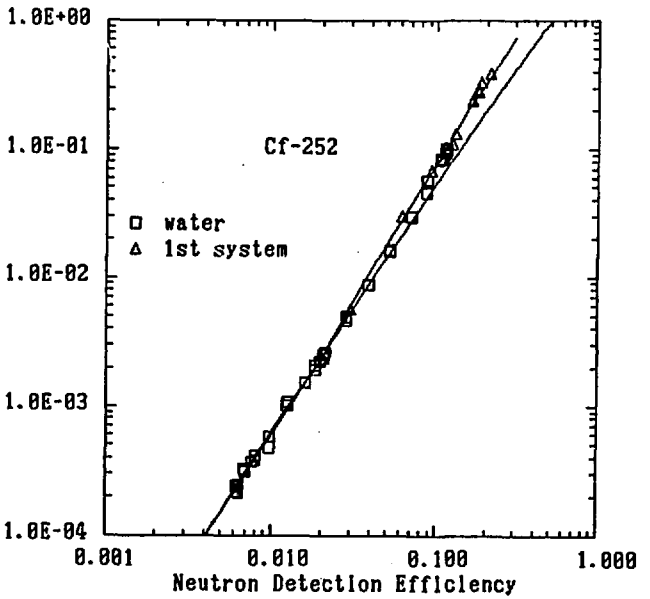

Fig.5 Comparison Between Theoretical Prediction and Experimental Data of Coincidence Counting Efficiency as a Function of Neutron Detection Efficiency for Cf-252

NONDESTRUCTIVE DETECTION METHOD OF TRACE AMOUNT OF FISSILE MATERIALS BY USING A NEUTRON GENERATOR

M. Haruyama, H. Gotoh, T. Kawamura and M. Takase

Japan Atomic Energy Research Institute
Tokai-mura, Naka-gun, Ibaraki-ken, 319-11, JAPAN

1. INTRODUCTION

Wastes containing transuranic elements(TRU) will be produced from the reprocessing plants after working in the country near future. These wastes will be classified and be disposed with the level of α radioactivity. This situation necessitates the development of nondestructive measurement techniques for the discrimination of these waste. A great part of those wastes will contain some amount of fissionable nuclides such as Pu-239. In order to measure fissile materials contained in these wastes, we have built an active neutron assay system and then carried out measurement experiments.

We introduce here the principle of the nondestructive detection method of fissile materials and the results obtained in the measurement experiments using 14 Mev neutrons produced by neutron generators.

2. DETECTION SYSTEM

We have constructed an active neutron detection system in order to develop the measurement technique for fissile materials contained in waste drums. This assay system was built as an experimental instrument a few yeas ago. The assay system was composed of a detecting assembly, a neutron generator, electric

circuits, a multi-channel scaler(MCS) and a control console. The detecting assembly was composed of graphite and polyethylene as moderator, the head of a neutron generator and He-3 detectors. Figure 2 shows a bird's eye view of the detecting assembly.

A cavity for measurement is surrounded by moderators, i.e. the inner wall of graphite with 20 cm thickness and the outer wall of polyethylene with 10 cm thickness. The head of the neutron generator was installed at one corner of the cavity, and also, cadmium shielded He-3 detectors for fast neutrons were installed inside the cavity. We tested two types of neutron generators, KAMAN's and SODERN's. The former is a pulse transformer type and the latter is a direct current high voltage type.

The electric circuit is very fast. Particularly, the resolving time of 350 ns was obtained for the total counting system. Properly, this assay system has an excellent tolerance against high γ ray background up to 500 R/h without shielding. If it makes sacrifice of counts a little bit, it is possible to use the system up to 1000 R/h sufficiently. The control console was composed of control circuits and a small computer. It is possible to control all parts of the assay system for measuring experiment.

3.DETECTION METHOD

The active neutron method is the way of detecting fissionable nuclides like Pu-239 and Pu-241 nondestructively by using an external neutron source. The way discussed in this paper uses a neutron generating accelerator as the external neutron source. Fissile material in a waste drum was irradiated with thermal neutrons originated from pulsed neutrons generated by the accelerator. Fission reaction (n,f) is induced by thermal neutrons which was moderated from 14 MeV neutrons generated by the accelerator. As a result, prompt fission neutrons are emitted. The prompt neutrons are detected by He-3 detectors shielded with cadmium. The explanation of data analysis on the active neutron method is shown in Fig. 1. It is possible to get data of

distribution of counts as a function of the elapsed time after pulse injection (time spectrum). The dwell-time per channel was set to 19 μsec and about 20 ms was consumed to sweep 1,024 channels. In order to obtain data, it is necessary to accumulate counts on each channel of the MCS, repetitively triggering by neutron pulses. The curve① shown in Fig.1 is 14 Mev fast neutrons generated from the accelerator. The generating time length is within 10 μsec. The generated fast neutrons reduce as shown by the exponential curve② seen in Fig. 1, because all fast neutrons change to thermal neutrons within about 700 μsec. The thermalized neutrons are appearing like as curve③. The curve④ is prompt neutrons of fission reactions induced by thermal neutrons.

4. MEASUREMENT EXPERIMENT

We prepared several kinds of 200 l drum-size specimens simulated reprocessing wastes without activity and a kind of encapsulated Plutonium (Pu-239: 96.7%) samples as fissionable transuranic materials for use of measurement. Kinds of specimen were concrete with hulls and caps, ordinary concrete, bitumen with co-precipitation sludge, sand and cloths. Table 1 shows specific of several kinds of simulated specimens. The detail of the specification of it is weight were described in the table.

In measuring experiment, we formed simulated wastes by combining the nonradioactive specimens and the plutonium samples The plutonium samples were placed at reserved positions in all kinds of the specimen drums. That drum was installed in the cavity of the detecting system and then was irradiated by several thousands of neutron pulses(10^6~10^7 neutrons/pulse). The total number of generated neutrons was about 5×10^{10} for one measurement, and the time spent in a measurement was about 17 minutes.

We can obtain raw data of time spectrum of fast neutrons like as shown in Fig. 3. This time spectrum graws as if a sum of two exponential components and one constant component. The detection efficiency of fast neutrons was about 1.9 percent for the cadmium

shielded neutron detectors. The exponential component with faster decay is induced by neutrons from the generator, and the slower component is attributed to prompt neutrons which are emitted by induced fissions. Therefore, we can obtain the net counts of prompt neutrons by separating the time spectrum into a sum of two exponential components and a constant one with the nonlinear least squares method.

Also, Fig. 4 shows that the thermal neutrons were measured by the detector of thermal neutron monitor which was installed in one corner of the cavity of the detecting system.

The thermal neutrons were measured at the same time with fast neutrons perfectly. As you know, the dieaway times of thermal neutrons and prompt neutrons have almost a same trend.

5. DATA ANALYSIS AND RESULT

The net count of prompt neutrons from fission induced by neutron pulses of the generator was obtained as a time spectrum of fast neutron component. Data analysis was carried out by a nonlinear least squares method using a micro-computer. After several iteration for fitting, the result of analysis was obtained. As results, integrated counts of prompt neutrons by fissions and its dieaway time, integrated counts of fast neutrons by the generator and its slowing-down time, integrated counts of background, and the respective standard errors were obtained at the same time automatically.

The response of the detecting system, the net counts against the amount of Pu sample, was examined over a wide range of the amount of Pu sample as fissile material (from 2 mg to 2,000 mg) for various kinds of matrices of simulated wastes. Figure 5 shows the relationship between the net counts and the Pu sample mass. The response characteristic curves were drawn through measured points of net counts versus Pu amounts for several matrices.

We have confirmed that the response characteristic curve have a good linearity over a wide range of Pu mass and have the

different detection sensitivity according to each matrices of wastes, cloth, sand, ordinary concrete, concrete with hull and end-caps, bitumen with co-precipitation sludge, borosilicate glass and empty drum, respectively. The matrix with the highest sensitivity is cloth among all kinds of matrices tested and the one with the lowest sensitivity is bitumen.

The detection limits of the detecting system for a various kinds of matrices of wastes were obtained by the analysis of measured data and the values were defined as 3 times of the standard errors of the total net counts. Table 2 shows the detection limits for all kinds of matrices and empty drum.

The values of mass of detection limits are given as the amount of Pu-239 for uniform activity distribution and for homogeneous matrices. The values of concentration of detection limits were obtained as the ratio of Pu mass to its total weight. The value of specific activity of detection limits were calculated with the total activities divided by the total weights.

We have confirmed that the values of detection limit are sufficiently lower than the recommended value of 30 nCi/g for surface storage.

6.CONCLUSION

We have obtained available results about the linearity response against the amount of Pu-239 and about the detection limits. In near future, we will make a more sensitive detection system of fissile materials, and also will promote a development program on the techniques of data analysis. We want to establish the method that can estimate the amounts of fissile materials contained in waste drums.

REFERENCE

1) H.Gotoh et al, NEACRP-A-1079(1990)

Table 1 Contents and Weight of Simulated Specimens

Name of specimens	materials contained in drum *	total weight (kg)
cloth	cloth	60
sand	river sand	340
concrete C	ordinary concrete only	458
concrete A	concrete with hulls and end caps	550
glass C	ordinary glass (special vessel ※)	384
bitumen A	bitumen and coprecipitation sludge	323
empty drum	air	30

* 200 L Drum
(Diameter:56.5cm , Hight:88.0cm , Thickness of SUS-304 wall:1.5mm)

※ cylindrical vessel for Borosilicate glass waste
(Diameter:43.0cm , Hight:97.0cm , Thickness of SUS-304 wall:6.0mm)

Table 2. Detection Limits of Fissionable Materials by Active Neutron Method (Homogeneous Waste)

Kinds of simulated waste	Mesusureing time (min)	Mass of detection limits ※ (mg)	Concentration of detection limits ※ (bpm)	Specific Activty of detection limits ※ (nCi/g)
empty drum	6.7	2.4	80.0	5.0
cloth	16.7	1.3	21.7	1.3
concrate C (ordinary)	16.7	9.0	19.7	1.2
concrate A (with hulls and end caps)	16.7	17.0	30.9	1.9
bitumen A	16.7	22.0	68.3	4.0
sand	16.7	2.9	8.53	0.45

※ Value of Detection limits was defined as 3 times of standard error(σ)
Using Pu(Pu-239:96.7%) sample as fissionable material.

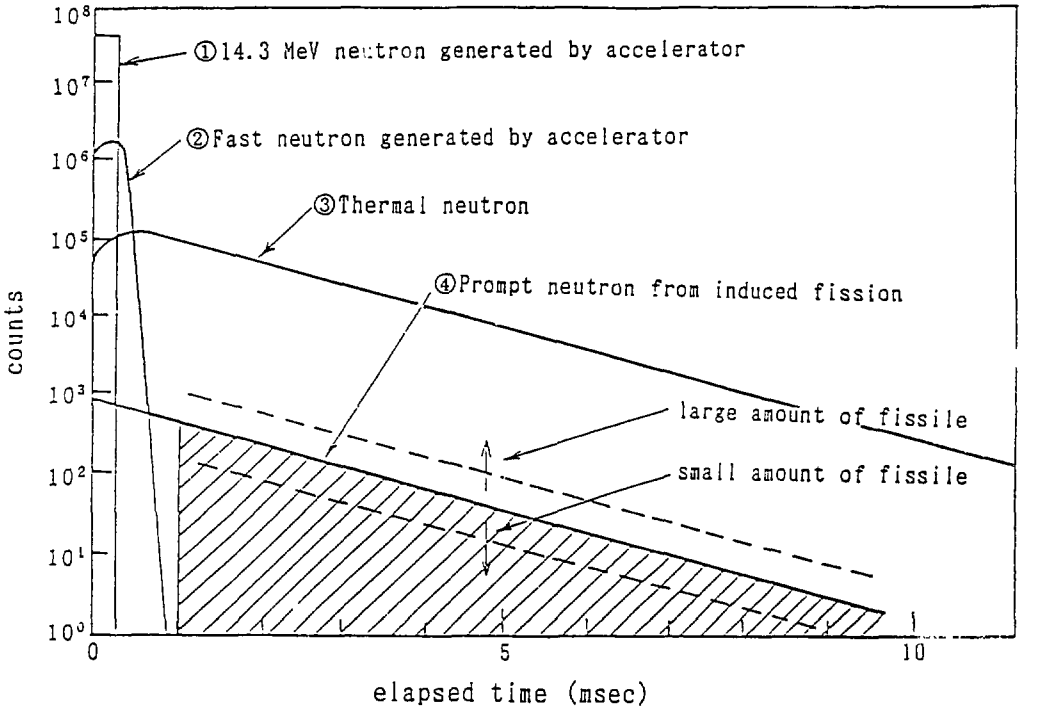

Fig.1 Explanation of Data Analysis on Active Neutron Method

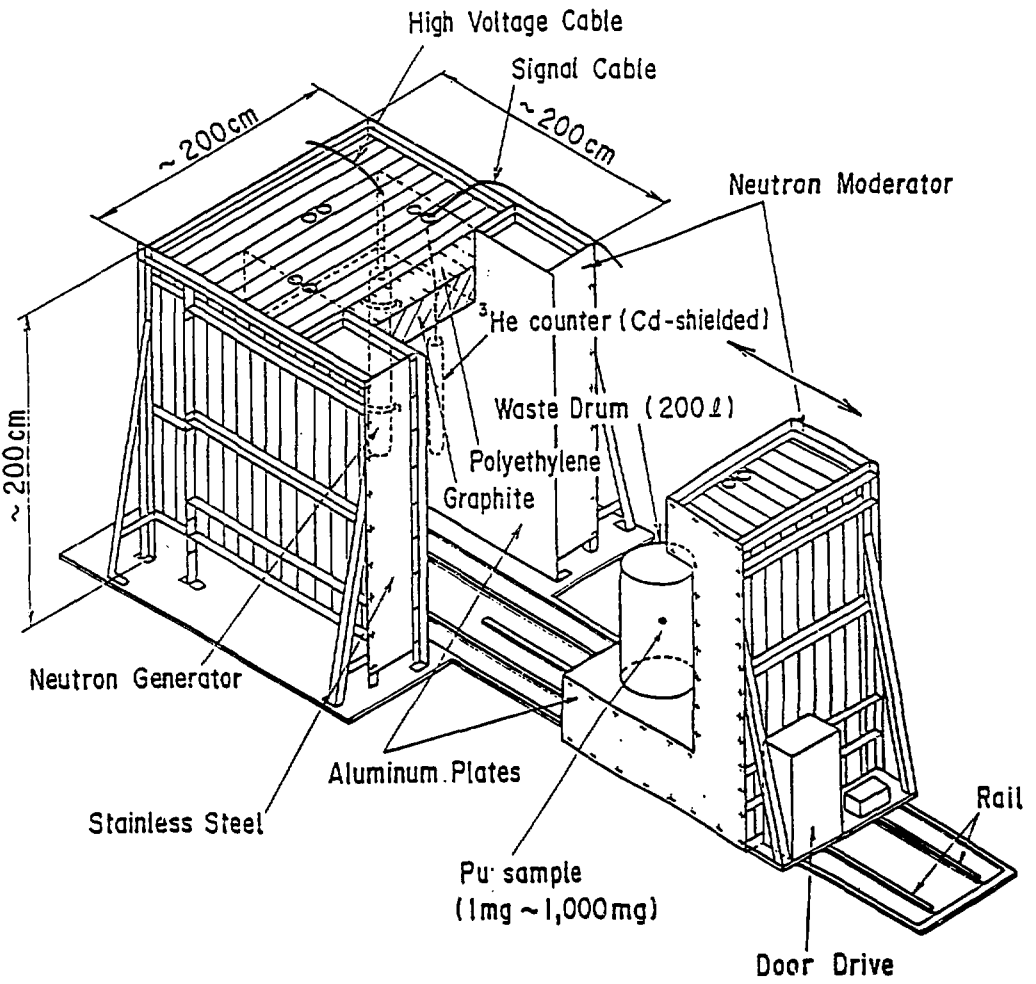

Fig. 2. Bird's Eye View the Neutron Moderating and Detecting Assembly for the Active Neutron Method

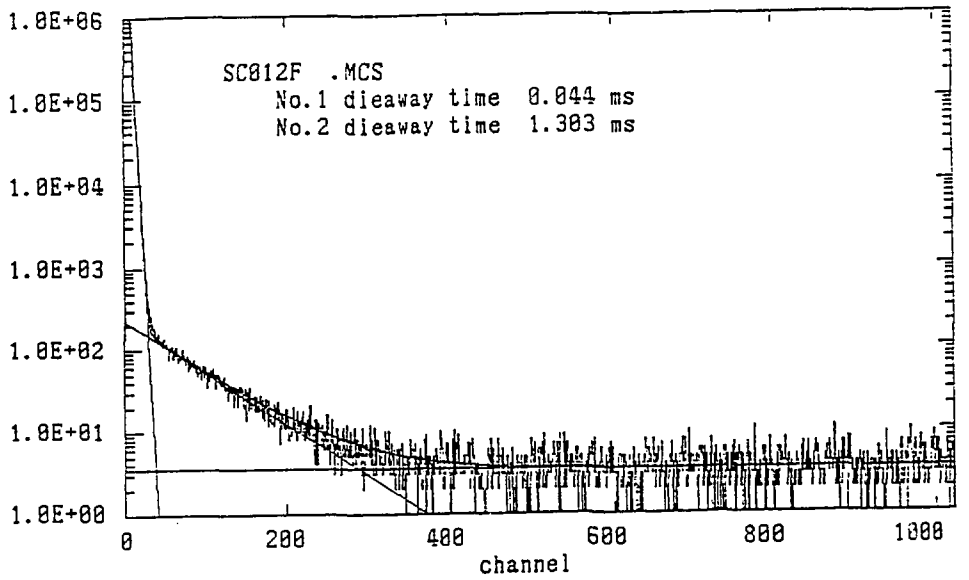

Fig. 3. Time Spectrum of the Fast Neutron Detector and Its Decomposition into Two Exponential Functions and a Constant Term

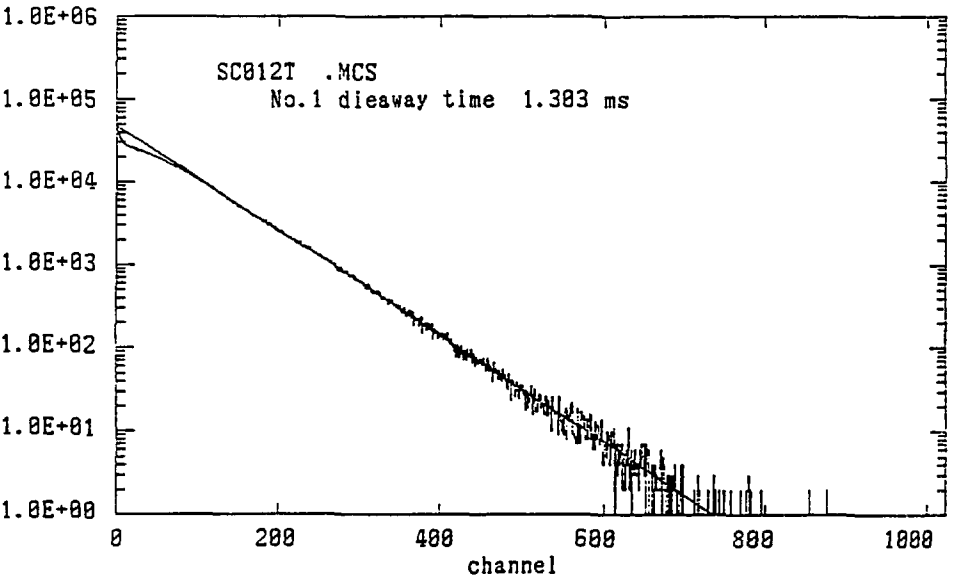

Fig. 4. Time Spectrum of the Thermal Neutron Detector Fitted with One Exponential Function

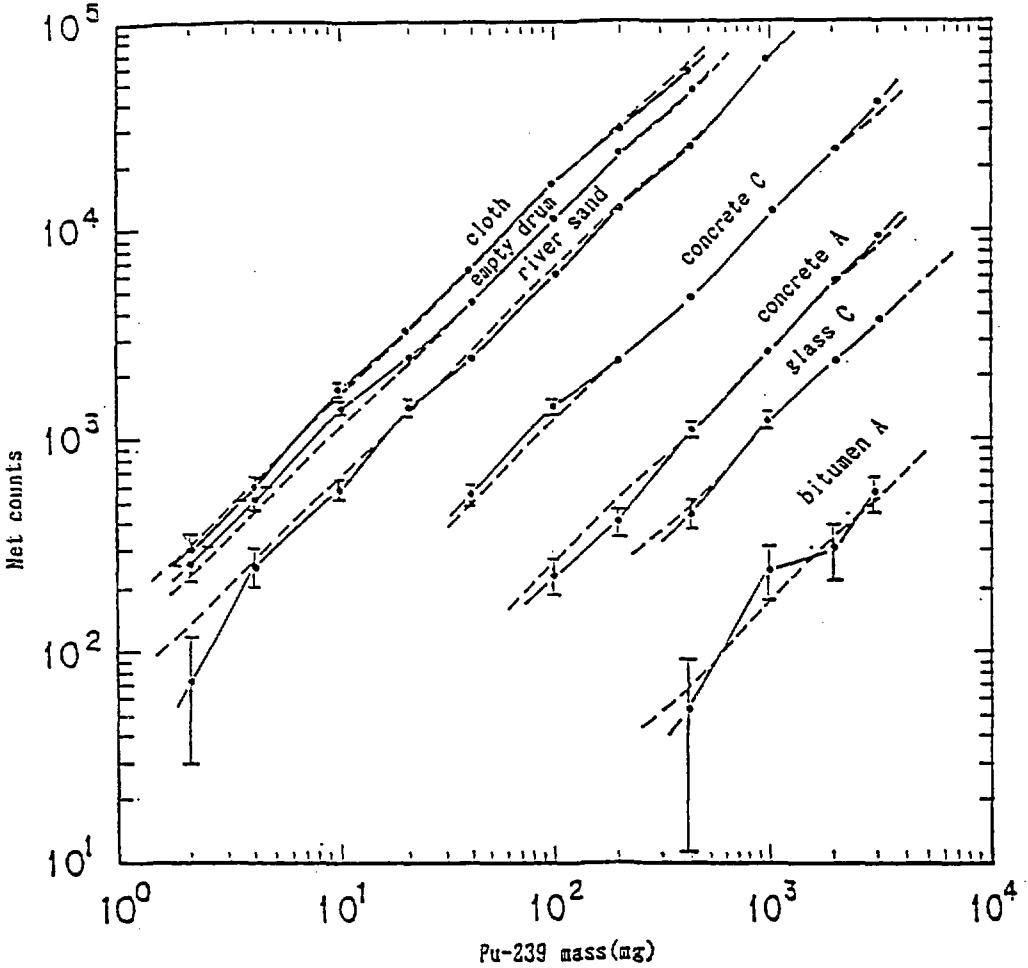

Fig. 5. Relationship Between Net Counts and Pu-239 Mass

PERFORMANCE TEST OF DRY TYPE RADON GENERATORS AND CALIBRATION

Y. HINO

Radiation Metrology Section, Electrotechnical Laboratory,
1-1-4 Umezono, Tukuba, Ibaraki 305, Japan

ABSTRUCT

The concentration of ^{222}Rn arising from a simple and practical radon generator, based upon solid ^{226}Ra sources, has been measured. Sources were made by dropping ^{226}Ra standard solution onto several materials and drying. The dried ^{226}Ra sources were encapsulated in several types of airtight capsules to collect arising ^{222}Rn. In order to measure the emission rate of ^{222}Rn from these sources, the intensity of 352 keV γ-ray from ^{214}Pb was monitored by a Ge detector. The activity ratios of ^{214}Pb to the ^{226}Ra with different source conditions were obtained. It was revealed that such dried ^{226}Ra sources had good characteristics as the basis of a practical radon generator.

1. INTRODUCTION

Recent years, as increased attention to the influence of radon on public health, many techniques have been developed for monitoring radon and its daughters. Although, the consistency in each methods itself is fairly well, the disagreements between different monitoring techniques are still serious.[1-4] It is urgently desired to have the official calibration system for radon monitoring instruments. To establish such system, it is necessary to have a well stable and easy handling radon generator. In addition, to study the behavior of radon and its daughters in biological and in environmental fields, it is also desired to supply calibrated radon laden gaseous.

Bubbling the radium solution has been widely adopted as the radon source because of its high efficiency of purging radon from the solution. However, there are some difficulties to treat such radioactive solution, especially to handle high intence sources. Solid sources, which are good for handling, but there are also some problems for stability of radon arising rate and consequential precision of the concentration. In this report, the radon arose from such solid source was corrected and arising rate with different source conditions were measured to make a practical radon generator.

2. EXPERIMENTAL PROCEDURES

Radium sources were made from ETL ^{226}Ra standard solution[5] (Radium chloride in 0.1N HCl, 3.7×10^4 Bq/g), dropping on several different metals, plastic disks and glass wool filters. These sources were kept in a desiccator more than two months to dry up and also to wait enough accumulation of radon in the radium solt. Then the sources were put into airtight capsules one by one. Figure 1 shows a most simple test capsule for measureing the emission rate with statical condition.

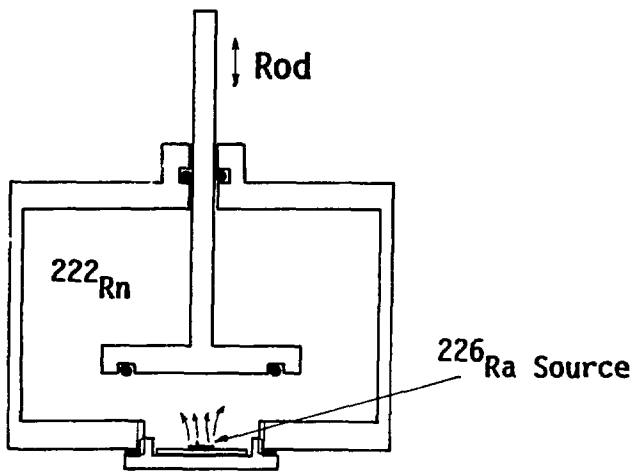

Fig. 1 The airtight capsule for ^{222}Rn collection.

The capsule was filled with low background dry air and was kept in room temperature about three weeks to arrive equilibrium between arose ^{222}Rn and the ^{226}Ra sources. Then the ^{226}Ra source was disconnected from this capsule, and concentration of collected ^{222}Rn was measured by a Ge detector. It came to clear that cetrain amount of ^{222}Rn was collected in the capsule with above measurement. To estimate the emission rate of ^{222}Rn more precisely, another capsule was desighned. Figure 2 shows the capsule with a pistone to breath in and out the carrier gas. In order to measure the concentration of arose ^{222}Rn, the source capsule was connected to the second airtight capsule with thin tube (2 mm inner dia.) and with balance pole which was jointed to the piston rods as shown in the figure.

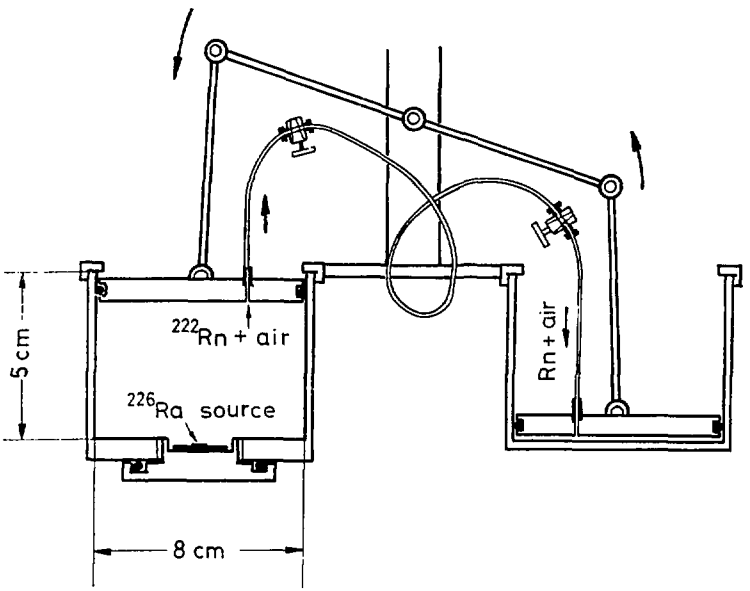

Fig. 2 The ^{226}Ra source capsule and the second capsule for γ-ray measurement.

When the piston of the source capsule was slowly downed, the piston of second capsule was lifted up just same stroke, so that radon laden air in the source capsule was successfully transferred to the another detecting capsule. The volume of source capsule was about 250 cm^3 and the hollow volume for radium source disk was 2 cm^3. Small remaining volume at the lower end of piston was

estimated to be about 3 cm^3, and small rest in the thin tube and micro valve was less than 1 cm^3. Finally, about 97% of radon laden air in the source capsule colud be transferred to the detecting capsule. Then, two capsules were disconnected and was left 4 hours to weit the equilibrium between ^{222}Rn and ^{214}Pb. After this, gamma-rays from detecting capsule were measured by a Ge detector.

Figure 3 shows a typical gamma-ray spectra form such capsule. Radon generating rates from different sources were obtained from the peak area of 352 keV gamma-ray from ^{214}Pb.

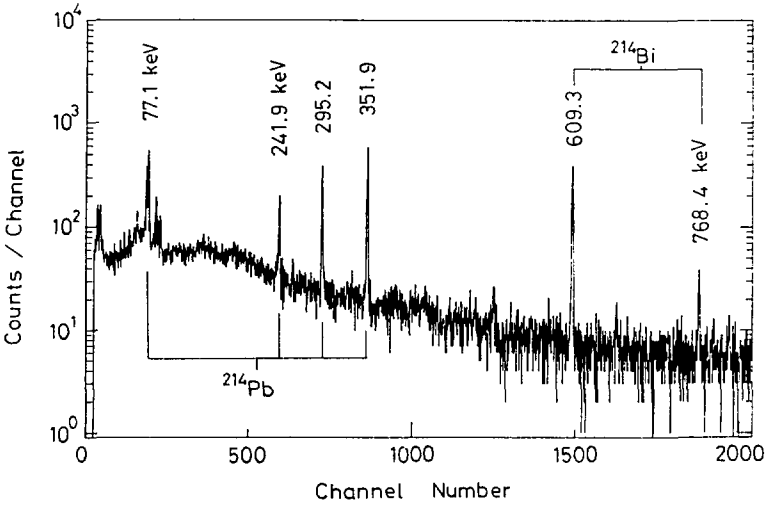

Fig. 3 Gamma-ray spectrum from ^{222}Rn dougthers.

The passive air filter type of radon generator was also tested in this study. The ^{226}Ra source was dropped on a glass wool filter and this filter was sandwiched by two additional filter to prevent contamination. Figure 4 shows this passive air type radon generator.

In this study, dry air was used as the carrier gas which was slowly introduced from one direction so that arose ^{222}Rn was removed from this filter. To estimate arising rate of ^{222}Rn, time dependent 352 keV γ-peak intencity was monitored with the Ge detector.

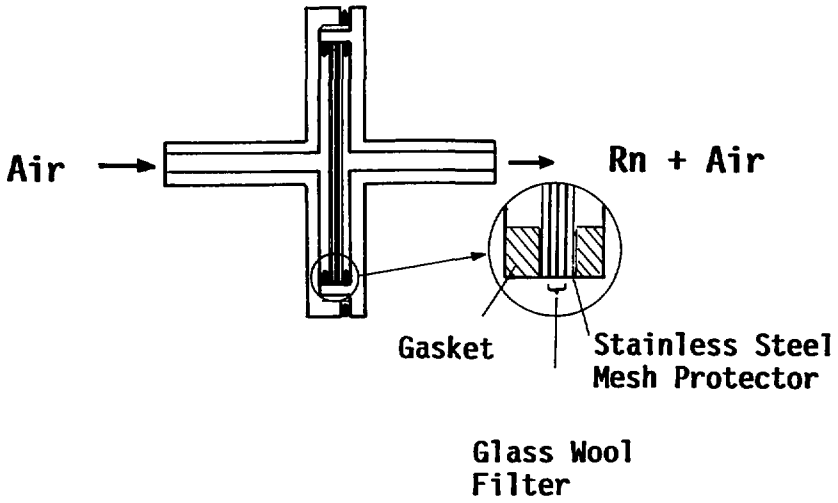

Fig. 4 Airfilter type radon generator.

Table 1 Activity ratio of transferred ^{214}Pb to the ^{226}Ra radon source.

Disk Material	Source Activity	Activity Ratio
Plastic	5.6 kBq	0.06
Plastic	20.5 kBq	0.05
Plastic + Ludox	5.8 kBq	0.09
Plastic + Ludox	20.4 kBq	0.08
Stainless steel	1.5 kBq	0.06
Stainless + Ludox	1.6 kBq	0.10
Aluminum	1.4 kBq	0.16
Copper	1.5 kBq	0.14

3. RESULTS AND DISCUSSION

The radon concentration in the detecting capsule was obtained assuming the homogeneous distribution of ^{214}Pb in the capsule. Table 1 shows the obtained activity of ^{214}Pb divided by that of ^{226}Ra source. In the case of plastic and stainless steel, higher radon arising rate was obtained when Ludox (fine colloidal silica) was added to the radium solution. Copper and aluminum disks, on which surfaces grew mold like copper and aluminum chloride, showed very good arising rate. It is clear from these results that the arising rate increases significantly with increment of the total surface area of the source. As for the source intensity, arising rate was not so affected as shown in the plastic case. Slight change might be caused because more bigger size of radium chloride solt was formed for intence source.

Figure 5 shows the result of passive air filter type radon generator monitoring the time dipendence of 352 keV γ-peak. Two different gas flow rates were tested with this system and also radium solution bubling with nearly same geometry was tried to make comparison with dry type radon generator. These result show the certain radon arising and which is almost independent with carrier gas flow rate.

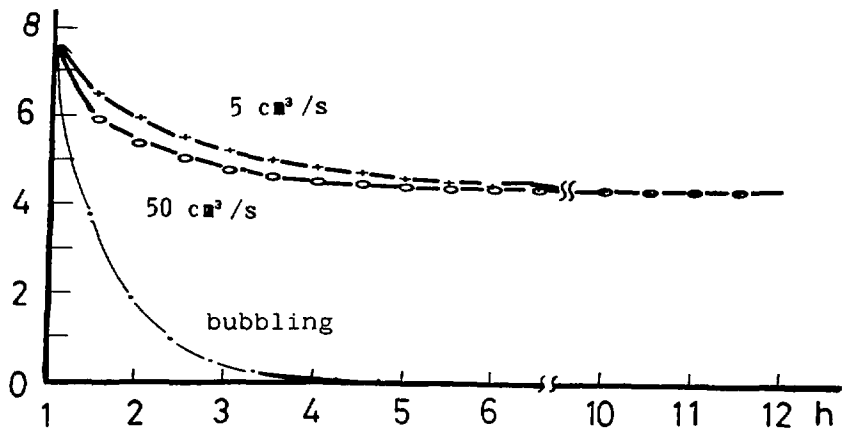

Fig. 5 The decreasing rate of 352 keV γ-peak from the airfilter type radon generator and a bubbling system.

4. CONCLUSION

It become clear that such dry type source has very good characteristics as a radon generator to supplying calibrated radon gas. The concentration of radon can be easily controlled by accumurating time and also changing source intensities. Scalling up is also no problem. In addition, there is no restriction on carrier gas and it does not include H_2O moisture nor HCl which are normally included in case from bubbling the radium solution.[6)]

In this study, ^{214}Pb was assumed in homogeneous distribution in the detection capsule. It may cause some error in the detection efficiency of the Ge detector, however, it will be solved using a well type detector and a smaller sampling capsule to get rid of this problem.

REFERENCES

1) I.M. Fisenne, A. George and M. McGahan, Health Phys. 45(2) (1983) 556.

2) J.C.H. Miles, E.J. Stares, K.D. Cliff and J. Sinnaev, Radiat. Prot. Dosim. 7(1) (1984) 169.

3) M. Simo, T. Iida and Y. Ikebe, Proc. Conf on Intercomparison of Different Instruments that Measure Radon Concentration in Air, ACS Symposium Series 331 (1987) 160.

4) J.C.H. Miles and J. Sinnaeve, Raiat. Prot. Dosim. 24(1) (1988) 313

5) O. Yura, Bull. of ETL 47(9,10) (1983) 21

6) K. Kondo, H. Muramatu, Y. Oki, T. Miura, M. Numajiri and T. Suzuki, Proc. of the 5th Workshop on Radiation Detectors and Their Uses, KEK Report 90-11 (1990) 16

RADIATION BIOLOGY OF SOFT X-RAYS

Katsumi KOBAYASHI
Photon Factory,
National Laboratory for High Energy Physics,
Oho, Tsukuba, Ibaraki 305, Japan

1. SOFT X-RAYS AND RADIATION BIOLOGY

Risk estimation of low dose and low dose-rate radiation to human body during long term is one of the most important problem for radiation biologists. One approach to this problem is an experimental one. Since radiation effects of low dose is very small or of very low frequency, huge amount of money and man-power for at least several years become necessary in order to get reliable experimental data using model animals such as rats. Epidemiological survey of people who had suffered from some kind of radiation accidents may be the only method to know the effects on human body.

Another approach to the problem is to elucidate completely the whole processes and mechanisms of biological effects of radiation and then to estimate the risk of low dose or low dose-rate irradiation logically. From this point of view, present status of the research is on the stage where the effects using cells or limited kinds of animals have been surveyed in relatively high dose region. Several molecular damages of DNA, presumably responsible for the effects, were identified in the cell level study, but process leading to the effects is still to be investigated. Dose-effect relationships have been obtained experimentally in several cases in acute irradiation. But their applicability to low dose or low dose-rate region is still in question.

One of the most important step in this course of study is to identify molecular damage and to know the mechanism

of their production in view of the deposited energy of radiation. To do this work, we need intense monochromatic radiation of desired energy from about a few eV to 100 keV. In this energy region, photon is absorbed by electrons and in some cases electrons are emitted from the atom (photoelectric effect). We are able to know the relationship between the deposited energy and molecular damages produced. Necessity of this kind of work had already pointed out by Platzman(1958)[1]. But we could not execute the experiments due to the lack of strong light (photon) source.

Recently with the advance of accelerator technology, synchrotron radiation(SR) has become available as a photon source strong enough even after monochromatized. We began to use SR for radiation biology study, after developing irradiation apparatuses. We can deposit defined amount of energy to an atom or a molecule, or generate secondary electrons having defined kinetic energy in the living organisms. Now we have three types of irradiation apparatuses corresponding to the photon energy region which covers in total from 40 ev to 15 keV. More than research proposals are accepted using various samples with various biological endpoints.

2. BIOLOGICAL EFFECTS ON MONOCHROMATIC SOFT X-RAYS

Some of the typical results obtained at the Photon Factory are introduced. One is biological effects of photoabsorption of phosphorus in deoxyribonucleic acid(DNA) molecule in living cells. DNA is known as a genetic materials and a key molecule for the cell to survive and to produce progeny. DNA molecule is the most sensitive to radiation and the damages on the molecule is closely related to the cell death or genetic changes. We irradiated monochromatic soft X-rays at the energy of phosphorus K-shell resonance absorption (2.15 keV) on yeast cells and the effects were compared to those irradiated

with soft X-ray of the energy just below the edge which can not be absorbed by phosphorus[2]. Results are shown in Fig. 1. Genetic changes were induced more effectively at the resonance absorption than at the energy below the edge, although the difference in X-ray energy is as small as 6 eV. This can be interpreted by the Auger effects at phosphorus atom in DNA. Auger electrons emitted from the phosphorus atom and/or the multiply-ionized atom are considered to play an important role in this biological enhancement. This kind of enhancement was observed in various cell lines.

Another line of study is to investigate photon energy dependence of biological effectiveness in the whole range of electromagnetic wave. Since energy deposition by accelerated heavy charged particle can be simulated as an integration of energy deposition by photon over the entire region of photon energy (so called "white radiation" approximation), accumulation of data on the effects of monochromatic photon in wide range of energy is required. Among the tested organisms, experimental data using spores are well accumulated using the advantage to survive in vacuum. X-ray energy dependence (action spectrum) of killing action to Bacillus subtilis spore is shown in Fig. 2[3]. Biological effectiveness increased with the decrease of irradiation X-ray energy. This can be interpreted by the fact that the photoelectrons produced by lower energy X-rays have lower energy and hence higher LET. Also observable is the enhancement at the absorption edges of calcium and phosphorus.

Studies on the molecular damages responsible for the enhancement are also being done. In the degradation spectrum of an amino acid, we observed the change in degradation pathway, suggesting that molecular damages specific to the resonance absorption might be produced[4].

3. FUTURE PROSPECT

Soft X-ray radiation biology began and some interesting results have been reported. In these reports, quantity of radiation was expressed in exposure (R or C/kg). Usually absorbed dose in unit of Gy is used in order to compare biological effects. When the photon energy goes down to soft X-ray region, energy of secondary electrons also goes down. Hence, the region in which secondary electron equilibrium is attained become smaller to the order of microns. We can not find out any homogeneous region in view of the atomic composition in the living organisms like living cells. For this reason, we can not define absorbed dose in the unit of Gy. Similar situation also occurs when high LET heavy ions are bombarded on the cells. Local absorbed dose depends very much on the distance from the track. Many theories have been proposed on the microdosimetry, but any theory complete enough to explain or be applicable in such cases. We, as radiation biologists, are waiting for the appearance of new theory of dosimetry or radiation biophysics which can treat our experimental results. We are sure that it will contribute very much to the estimation of the risk of low dose radiation, which has been eagerly asked by the modern human society.

References

1) Platzman, R.L.(1958) In "Radiation biology and medicine" Ed. W.D. Claus, Addison-Wesley Press. p15.
2) Kobayashi, K., Hieda, K., Maezawa, H., Furusawa, Y., Suzuki, M. and Ito, T. (1991) Int. J. Radiat. Biol., 59, 643-650.
3) Munakata, N. (submitted to Radiat. Res.)
4) Yokoya, A., Kobayashi, K., Usami, N. and Ishizaka, S. (1991) J. Radiat. Res., (in press)

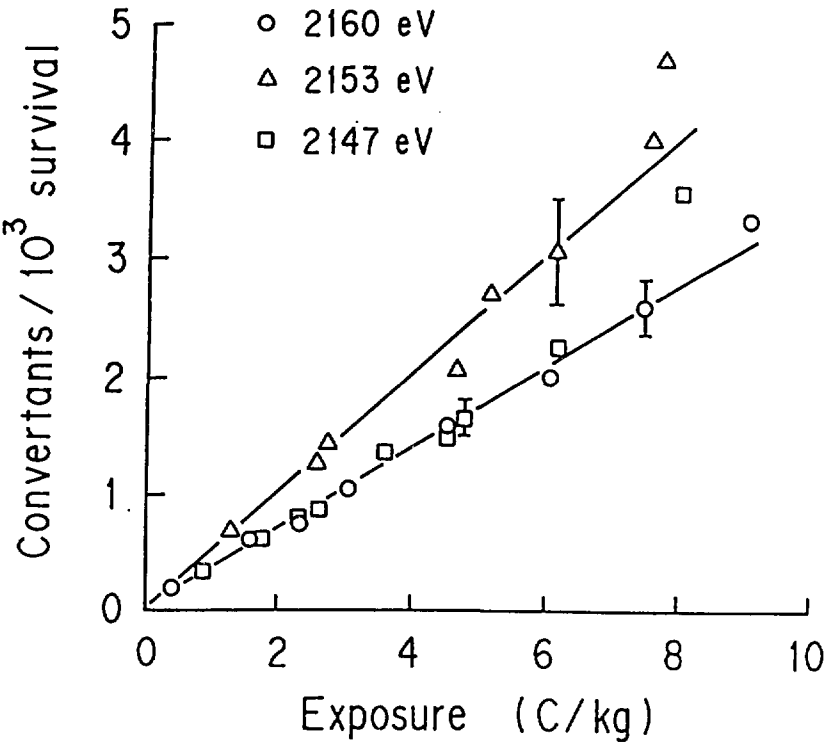

Figure 1. Induction of mitotic gene conversion at the *trp-5* locus in diploid yeast cells irradiated at three X-ray energies:2146, 2153 and 2160 eV.

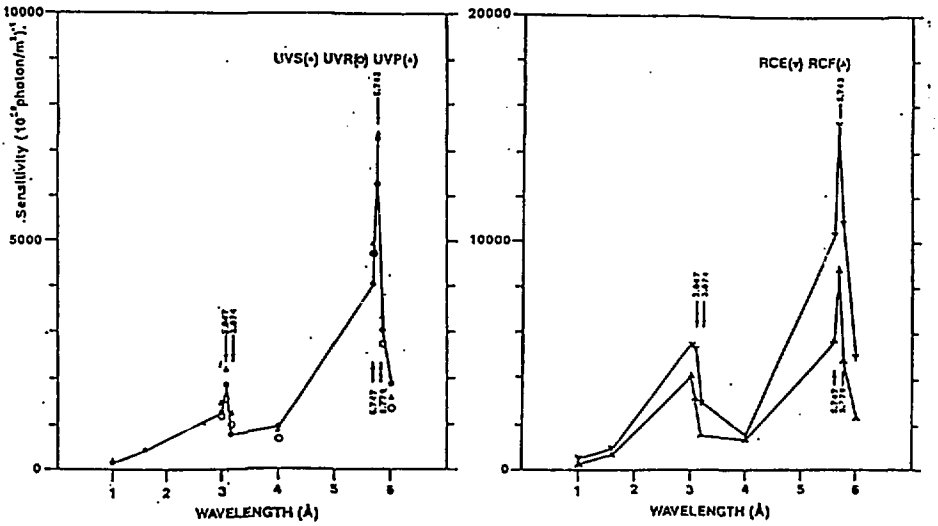

Figure 2. X-ray energy dependence of lethality of *Bacillus subtilis* spore.

DOSIMETRY OF SYNCHROTRON RADIATION IN 7-30 keV REGION AT PF

S.BAN, H.HIRAYAMA, Y.NAMITO, S.TANAKA*, H.NAKASHIMA*, Y.NAKANE*, M.YOSHIZAWA* and N.NARIYAMA**

National Laboratory for High Energy Physics, Tsukuba, Ibaraki 305
*Japan Atomic Energy Research Institute, Tokai, Ibaraki, 319-11
**Ship Research Institute, Tokai, Ibaraki 319-11

1. ABSTRACT

The characteristics of some X-rays dosimeters were studied in 7-30 keV energy regions at Photon Factory (PF) in KEK. Synchrotron X-rays intensity was measured using a parallel plate free-air ionization chamber and the chamber was calibrated by the total absorption calorimeter. Dosimeters, such as photodiodes, TLDs and ferrous sulphate dosimeters, were placed behind the chamber and irradiated by monochromatic X-rays.

2. INTRODUCTION

Measurements were done at the vertical wiggler beam line (BL-14C) using silicon (111) double crystal monochromator. At the energy region 7-30 keV, photon fluxes are between 5×10^{9} and 1×10^{11} photons $(s\ cm^{2})^{-1}$, which are more than ten times higher than usual facilities for dosimeter calibration. The absolute photon intensity was measured using the total absorption calorimeter[1]. A parallel plate free-air ionization chamber was calibrated by the calorimeter. To reduce ion recombination, space charge effect and field distortion in the chamber[2], it was put in a decompression chamber. The air pressure in the chamber was between 0.26 and 1.0 atm. The ionization chamber is shown in Fig. 1. Dosimeters were placed in the air and

irradiated by monochromatic X-rays. In front of the dosimeters, the ionization chamber was placed.

To monitor higher harmonics content from the monocromator during irradiation, 100-μm-thick Be foil was placed in a vacuum chamber and incoherent scattering photon spectra were measured at 90 degrees using HP-Ge detector. The monocromator was controlled to reduce higher harmonics. The vacuum chamber was placed in front of the ionization chamber.

3. PIN SILICON PHOTODIODE

Commercially available PIN silicon photodiodes are recently used in direct current mode at room temperature[3] though they are originally manufactured as detectors of visible radiation. The diodes were the Hamamatsu S3590-04 and -06 types which are windowless ones and photo-sensitive area size are 10x10 mm. The P-type region is on the photon incident side. Their wafer thickness are 300 and 500 μm, respectively. They were placed in an aluminum box which has 40 μm thick beryllium light-tight entrance window. Diodes were connected to a picoammeter (Keithley 485). Mainly diodes were operated in the photovoltaic mode without bias voltage. In front of the aluminum box, the ionization chamber is placed.

Hamamatsu S3590-04 type diode was irradiated by 15 keV X-rays at a reverse bias voltage of 70 V. The photon flux was monitored by the ionization chamber because the flux changes due to thermal stress of monochromator by wiggler radiation. Measured current of the diode was normalized by that of the ionization chamber and the normalized current of diode was almost constant. The changes were at most 0.1 % or less during irradiation up to 2.1×10^{14} photons cm^{-2} which corresponds to the absorbed dose of 5000 Gy at the surface of the diode.

X-rays beam was defined by 2-mm diameter slit placed in front of the ionization chamber. The mean energy required to produce one ion pair in silicon by electrons is 3.68 eV at room temperature[4]. Then photon flux is given using measured current

by diodes as follows;

$$\text{Flux} = \text{Current} * 3.68 * (\text{Photon energy} * 1.60\text{x}10^{-19})^{-1} * \text{Eff}^{-1}$$

$$\text{Eff} = (1 - \text{Backscatter Energy Loss}) * (1 - \text{Transmission})$$

Backscatter energy loss from silicon was evaluated by the simple method shown in ICRU-Report 17[5] and transmission probability was calculated using photon attenuation coefficients by Hubbell[6]. At 30 keV, only about 10 % of total energy is deposited in diodes because transmission probability is increased. Measured photon fluxes by ionization chamber and diodes are shown in Table 1. Both results are in good agreement within about 4 %.

4. FERROUS SULPHATE DOSIMETER

There are many studies about radiation chemical yield, G value, of the Fricke ferrous sulfate dosimeters and they are decreased for low energy photons. Those studies were not done for mono-energy photons and in this work dosimeters were irradiated by 15 keV mono-energy photons.

Prior to the irradiation at PF, the dosimeter solution in Teflon cells and glass cells were irradiated by ^{60}Co gamma-rays at JAERI and it was shown that storage in Teflon did not affect its radiation sensitivity.

Cylindrical irradiation cells were made of Teflon and their inner diameter is 30 mm and depth is 20 mm. Their entrance window for X-rays are made of Kapton foils 25 μm thick. They were filled with 1 mol m^{-3} ferrous ammonium sulphate dissolved in 400 mol m^{-3} sulphuric acid. Spectrophotometic analysis was done at 304 nm using 1 cm absorption cell. Increase in absorbance was between 0.16 and 0.23. Measured doses are shown in Table 2. The reported molar linear absorption coefficient in ICRU-35[7] is in a little different from that in ICRU-17[5]. So doses were evaluated using ICRU-35 and multiplied by 15.5/13.6, which is the

ratio of G value of ^{60}Co gamma-ray to that of 15 keV X-ray reported in ICRU-17[5].

The free-air ionization chamber was used to know photon fluxes during irradiation and doses in the Fricke dosimeter was also evaluated by these fluxes. Backscatter and sidescatter energy loss from irradiation cells (3 and 0.6 %, respectively) were also evaluated by the method shown in ICRU-17[5] and transmission probability (2.4 %) was calculated using photon attenuation coefficients by Hubbell[6]. These evaluated doses using the ionization chamber were in agreement with measured doses by Fricke dosimeters within 3 %.

REFERENCES

[1] H.Nakashima et al., to be published in Nucl.Instr.Meth.

[2] Patricia B. Scott and J.R. Greening, Phys.Med.Biol. 8 (1963) 51.

[3] M.Krumrey et al. Rev. Sci. Instrum. 60 (1989) 2291.

[4] ICRU Report 31, ICRU Publication (1979).

[5] ICRU Report 17, ICRU Publication (1970).

[6] J.H.Hubbell, Int.J.Appl.Radiat.Isot. 33 (1982) 1269.

[7] ICRU Report 35, ICRU Publication (1984).

Table 1. Measured photon fluxes by free-air ionization chamber and Hamamatsu S3590 type PIN silicon photodiode

Photon Energy keV	Ionization Chamber x 10^8 Photons s^{-1}	Diode	Wafer Thickness μm
7	1.70	1.68	300
7	1.66	1.65	500
10	12.0	11.7	300
10	14.1	13.8	500
10	12.6	12.4	500
15	24.1	22.5	300
15	25.5	24.5	500
30	2.67	2.68	500

Table 2. Measured photon doses at 15 keV by free-air ionization chamber and Fricke dosimeters.

Weight[a] (g)	Measured Dose (Gy)	
	Ionization Chamber[b]	Fricke Dosimeter[c]
14.11	62.5	60.4
13.50	71.2	72.1
13.96	53.1	51.6

a: Weight of Fricke dosimeter solution in irradiation cell

b: Dose in Fricke dosimeter evaluated by measured fluxes using the ionization chamber. Escape energy from dosimeters were evaluated by the simple method in ICRU-17

c: Doses were evaluated using ICRU-35 and multiplied by 15.5/13.6 which is the ratio of G value of ^{60}Co gamma-ray to that of 15 keV X-ray reported in ICRU-17

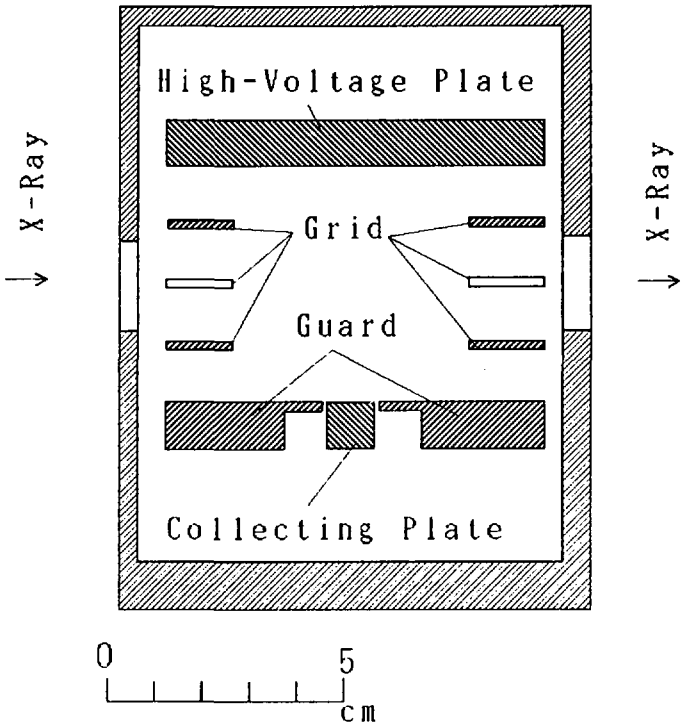

Fig. 1. Parallel Plate Free-Air Ionization Chamber

RADIATION DOSIMETRY OF TOOTH ENAMELS WITH ELECTRON SPIN RESONANCE (ESR)

--- DOSIMETRY FOR RESIDENTS CLOSE TO THE CHERNOBYL REACTOR ACCIDENT ---

Hiroshi ISHII[1,*], Motoji IKEYA[1] and Masaharu OKANO[2]

[1]Faculty of Science, Osaka Univ., Machikaneyama 1-1, Toyonaka-shi, Osaka 560, Japan

[2]Association of Radiation Effects, Kajicho 1-9-16, Chiyoda-ku, Tokyo 101, Japan

(*Present affiliation is Okayama Ceramics Research Center, Nishikatakami, Bizen-shi, Okayama 705, Japan.)

Electron spin resonance (ESR) dosimetry method using tooth enamel was developed as to detect the minimum radiation dose of around 10 mGy. The main broad signal component must be subtracted from the ESR spectrum to get the signal induced by radiation. Dosimetry of residents close to Chernobyl reactor accident was made using eight tooth pieces with ESR. The obtained dose ranges from about 20 mSv to about 70 mSv including the effect of natural radiation and the dental X-rays. The ESR dosimetry system was developed to measure, the cumulative radiation dose in a tooth without extraction.

1.ESR DOSIMETRY METHOD

Electron spin resonance (ESR) and thermoluminescence (TL) have been useful method for studies of radiation effects in solids. Radicals or unpaired electrons created by radiation is stabilized. Radiation dose is determined from the ESR signal intensity. We have investigated the ESR dosimetry of fossils and minerals that have been exposed to natural radiation and established a method of ESR dating method in earth sciences [1]. This method has been developed to the application of the various field of science and technology; radiation monitoring, health physics, earth science, anthropology, archaeology etc..

In addition to anthropological applications, tooth enamel is an adequate dosimeter materials for estimating the degree of exposure of a human being to accidental radiation [2-4]. The dosimetry technique of tooth enamel is important since it can estimate the human exposured doses directly.

2.ESR SPECTRA OF TOOTH ENAMELS

ESR dosimetry is a method to detect atomic bomb radiation as demonstrated using human tooth enamels and shell buttons at Hiroshima and Nagasaki [2,5–7]. Extensive studies on tooth enamel have been made by several investigators. The topics studied include the dependence of radical formation efficiency on radiation energies (quality effect) [3,5,6]. The separation of X-ray doses from gamma ray doses was attempted by measuring the front and back of a tooth by mechanical separation [8]. Some basic studies of the secondary electron equilibrium have been made to separate the dental X-ray effect [9]. The quality effect can be clearly seen in ESR images of the human tooth irradiated by X-rays and gamma rays [10] using microwave scanning ESR microscopy [11].

The ESR dosimetry was developed as to detect the minimum radiation dose of around 10 mGy (1Gy = 1J/kg), which causes us difficulty to separate the effects of dental X-rays and natural radiation dose [8,9].

The ESR measurements were carried out at room temperature with a JEOL RE-1X spectrometer at the microwave power of 5 mW and 100 kHz modulation amplitude of 0.2 mT following the recommended procedures described in our previous work [4].

Figure 1 shows the typical ESR signal of radicals created by radiation in a tooth enamel; peaks are observed at g=2.0037 and g=1.997. The equivalent dose (ED) of each sample was obtained by extrapolating linear enhancement of the intensity of radiation-induced signal using the least square fitting.

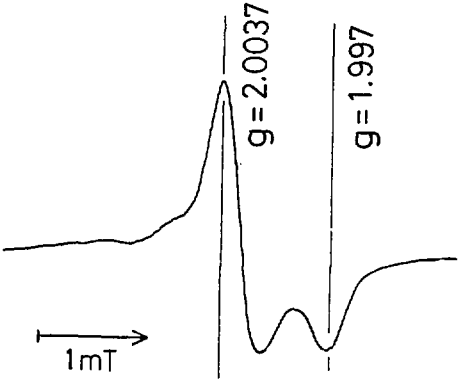

Fig.1. The typical ESR spectrum in tooth enamel exposured radiation.

The presence of the broad signal at g=2.0045 due to organic radicals prevent accurate determination of the signal intensity for lower doses of radiation. To obtain the signal intensity of radiation-induced radicals accurately, one must separate the broad signal component from the spectrum. The ESR spectrum of a tooth irradiated by gamma rays up to 2.0 Gy is indicated by the curve A in Fig.2(a). The spectrum indicated B is the one obtained with a computer by separating the signal of organic radicals, shown by the dashed-line curve, from spectrum A. The typical spectrum peaking at g=2.003 and g=1.997 which is created by radiation is separated.

Figure 2(b) shows the peak-to-peak signal intensities of the spectra as a function of the

absorbed dose. Subtracted spectrum intensities B_{pp} are better correlated than the apparent signal intensities A_{pp}, since the intensity due to organic radicals varies from sample to sample considerably.

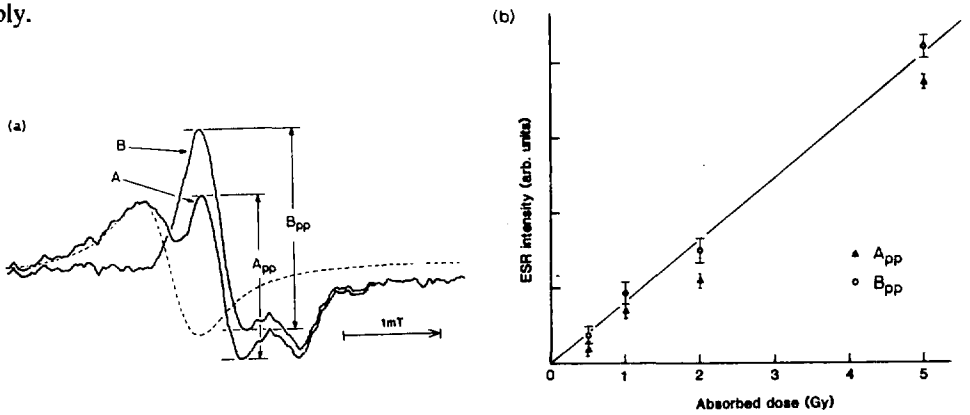

Fig.2. (a) ESR spectrum of a tooth gamma-rayed with a dose of 2.0 Gy. The spectrum indicated by the letter A is obtained by the measurement of the tooth enamel, and the spectrum indicated by B is obtained by separating the broad signal of organic radicals at g=2.0045 (broken line) from the spectrum indicated by A. A_{pp} and B_{pp} are the peak-to-peak signal intensities of radicals by radiation. (b) The relationship between the ESR intensities and the absorbed doses. A_{pp} and B_{pp} denote before and after separation from the broad signal, respectively.

3. DOSIMETRY OF RESIDENTS CLOSE TO THE CHERNOBYL REACTOR ACCIDENT

The accident of the nuclear reactor at Chernobyl is a tragedy that modern civilization has experienced in 20th century following the dropping of atomic bombs at Hiroshima and Nagasaki. Our limited information on the effect of radiation on human being is based on the accumulated data at Hiroshima and Nagasaki at the sacrifice of the survivor citizens. This information is not complete and sufficient to predict the effect at Chernobyl as the situation is completely different. Scientific investigation on radiation exposure at Chernobyl should be made thoroughly at the early stage with available scientific means.

Although major problems of radiation exposure to residents at Chernobyl are internal exposure due to radioactive elements from the foods, the cumulative external radiation exposure to residents is also important to assess the health hazard.

We have received 14 pieces of extracted human tooth out of dentists during dental treatments in Braginskij, Gomeliskoi, 50 km away from Chernobyl and investigated the absorbed radiation dose with ESR [12]. Eight tooth pieces were selected for this measurement since they were in low degree of dental caries, and retains healthy enamel parts. Both caries and dentine

were removed carefully with a diamond cutter microsaw and a small grinder with different blades in a wet state. The enamel parts were dried in oven at 40 C and were crashed with a mortar and a pestle to measure the ESR spectrum. All samples were irradiated with gamma-rays from ^{60}Co (dose rate 500 mGy/h) in 3 steps up to 750 mGy to calibrate the ESR signal intensities.

ESR spectra of sample #1 and sample #7 are shown in Fig. 3. ESR spectrum before irradiation shows a broad line for all samples except one of #7 since a signal of organic radical (g=2.0045) is dominant component. A signal of radiation effect (g=2.0037 and g=1.997) is masked. Separation of the signal of radiation effect from the signal of organic radical is necessary to obtain the accurate intensity [4]. A computer program separated the radiation-induced signal from the overlapping signal of organic radicals by subtracting.

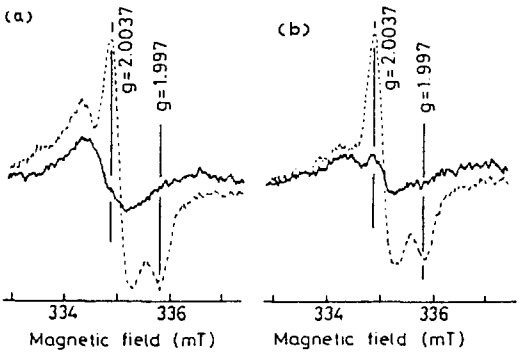

Fig.3. ESR spectra of tooth enamels; (a) #1 and (b) #7. Solid lines indicate ESR spectra induced by natural and accident radiation. The dotted lines indicate ones enhanced by gamma-rays from the source of ^{60}Co for calibration. The #7 sample shows radiation-induced signal (g=2.0037) clearly in ESR spectrum before artificial gamma-ray irradiation.

Present results of measurements are plotted in Fig.4 with natural radiation dose received tooth enamels on the assumption that annual dose rate is 0.5mGy/year or 0.9mGy/year.

One can assess that the dose ranging from 20 mSv to 70 mSv would be due to the reactor accident and to the natural radiation and the dental X-ray effects. (The effect of dental X-ray would be around 10 mSv at most assuming several exposures.)

The purpose of this measurement is only to give a preliminary report of the exposure to residents close to Chernobyl using ESR dosimetry of tooth enamels. Our conclusion is that the accidental radiation dose of residents at Braginskij, 50km away from Chernobyl would be about 5-20 mSv from the ESR signal intensity of tooth enamel if the natural background dose ((0.5 0.9 mSv/y) (permanent tooth ages)) is extracted.

We emphasize that a human tooth piece is a good radiation dosimeter in radiation accidents and that resident's teeth extracted upon dental treatment should be preserved and collected systematically with information on radiation exposure to assess the cumulative radiation dose.

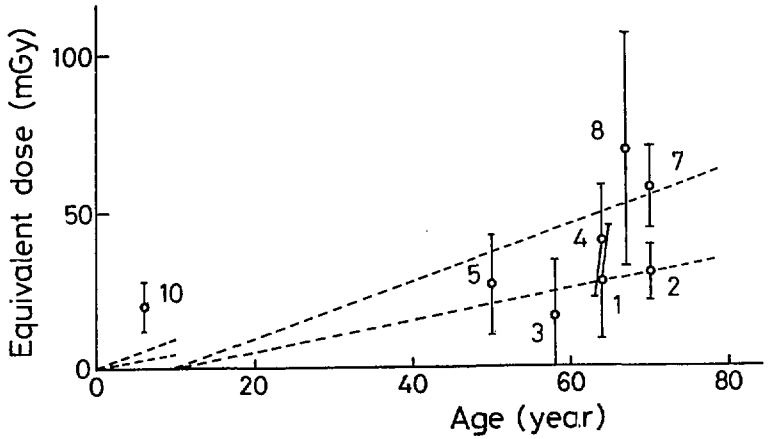

Fig.4. The results of estimated equivalent doses and persons' age. The numbers near by data points indicate data number respectively. The broken lines show cumulative absorbed dose of natural radiation on the assumption that annual dose rate is 0.5mGy/year or 0.9mGy/year.

4. ESR DOSIMETRY SYSTEM FOR AN IN-VIVO HUMAN TOOTH

ESR tooth dosimetry could be used in monitoring the radiation exposure of radiation-related work personnel or people who have encountered unexpected radiation. Since most survivors of radiation accidents or atomic bomb exposure do not carry dosimeters, the dose of radiation to which they are exposed must be estimated immediately for appropriate medical treatments.

A tooth sample is inserted into the microwave cavity of a conventional ESR spectrometer for an ordinary ESR measurement. Although tooth enamel is an adequate dosimeter material, one must use a tooth extracted by dental treatment for the measurement of the ESR spectrum in ordinary system.

We tried to develop the ESR dosimetry system to measure the cumulative radiation dose in a tooth without extraction [4]. The system consists of a TE_{102} cavity with an aperture at the end plate, a Nd-B-Fe

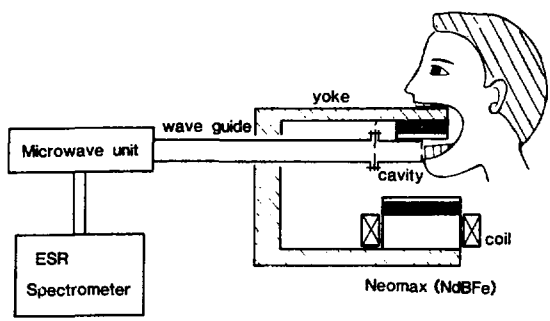

Fig.5. A schematic illustration of the ESR dosimeter reader for in-vivo human tooth measurement. The front molar of the lower jaw is attached to the end hole of the TE_{102} microwave cavity. The oral magnet using Nd-B-Fe and the field sweep coil produce the necessary magnetic field.

(Neomax) oral magnet and a commercial ESR spectrometer (JEOL RE-1X). The front molar is attached to the aperture of the cavity to detect radicals created by radiation in the tooth enamel (shown as Fig.5).

A special rectangular cavity (TE_{102} mode) with a slit aperture on the upper end plate was designed for the in-vivo ESR tooth dosimetry system, as shown in Fig.6 ('TE_{102}-slit cavity'). The slit localizes microwaves out of the cavity. Using this cavity, ESR signal of the sample from the area close to the slit can be measured.

The signal intensities of tooth pieces measured by using the TE_{102}-slit cavity and a commercial cylindrical cavity (TE_{011} mode) are shown as a function of the radiation dose in a logarithmic scale in Fig.7. The curve of intensities vs doses is linear for a wide radiation dose range. The intensity using the TE_{102}-slit cavity, however, is 1/50 of that obtained for a whole tooth in the TE_{011} cavity. ESR measurements with the TE_{011} cavity were also made at 77 K using a liquid nitrogen dewar. The overall signal intensity is less than that at room temperature due to the reduced Q-value by the dewar. The lower limit of the minimum detectable dose using the TE_{102}-slit cavity experiment was 10 Gy.

It is possible, in principle, that the present TE_{102}-slit cavity can be used to measure the radiation exposure of a human tooth directly without extraction.

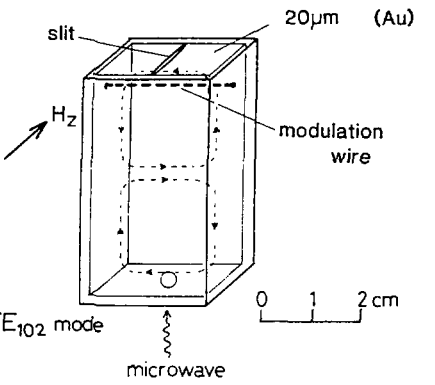

Fig.6. A home-designed cavity for in-vivo tooth dosimetry. A rectangular cavity (TE_{102} mode) with a slit aperture on the upper end of a thin Au foil (20- m thickness) mechanically enforced by a quartz plate. The microwave magnetic field is indicated by dashed lines.

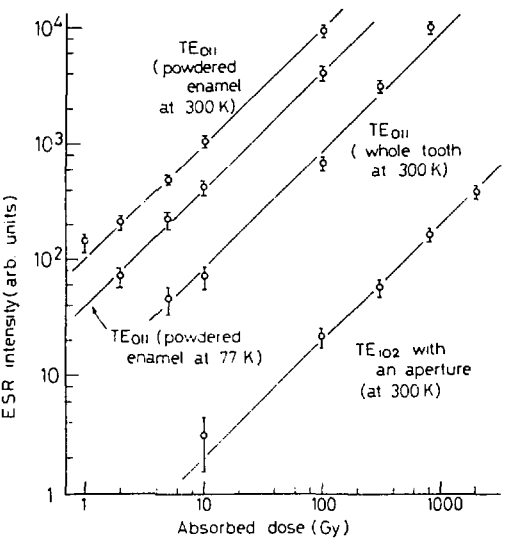

Fig.7. The relationship between the radiation dose and ESR signal intensities for a front molar measured with the TE_{102} cavity and with the TE_{011} cylindrical cavity.

A small oral magnet that produces the magnetic field only at the surface of the front molar was specially designed and manufactured with the permanent magnet material of Nd–B–Fe (Neomax) [13]. The front molar of a patient is attached to the aperture slit of the TE_{102} cavity so that the ESR signal intensity of the enamel can be directly measured without extraction. Figure 8 is an illustration of the ESR cavity system with a special oral permanent magnet with a field sweep coil.

Unfortunately, the field is too inhomogeneous to observe the signal in tooth enamel; the linewidth of 0.2mT around g=2.003 for polycrystalline hydroxyapatite of the enamel is broadened up to 1–2 mT.

A large magnet is used in magnetic resonance imaging (MRI) with a highly sensitive spectrometer. It is hoped that these can be used in detecting the radiation doses of persons. Some problems encountered in this preliminary study can be solved with the present technology.

Although this first test machine is unfortunately not practical because of the magnetic field inhomogeneity, a radiation dosimeter directly measuring the dose of exposed human beings is strongly hoped for. A human tooth dosimeter which can be used without extraction must be developed as a direct human dosimeter.

Acknowledgement —— We thank Dr. A.M. Skriabin in USSR for supplying us the extracted tooth samples and Mr. S. Toyoda for his useful discussion on a computer program to separate the ESR signal from a broad overlapping signal. We thank Dr. Kobayashi and Mr. Konishi of the Sumitomo Special Metal Co. for their help in designing and measuring the uniformity of the magnetic field of the oral magnet. The gamma irradiation was made at the Institute of Scientific and Industrial Research of Osaka University. Development of in-vivo dosimetry system is supported by the 14th Research Grant from the Nissan Science Foundation and also by a Grant-in-Aid for Developmental Research from the Ministry of Education, Science and Culture (No. 62890007).

References

[1] M. Ikeya, in: Dating and age determination of biological materials, eds., M.R. Zimmerman and J.L. Angel (Croom Helm, London, 1986) p.101.

[2] M. Ikeya, J. Miyajima and S. Okajima, Jpn. J. Appl. Phys. **23** (1984) L697.

[3] B. Pass and J.E. Aldrich, Med. Phys. **12** (1985) 305.

[4] H. Ishii, M. Ikeya, Japan J. Appl. Phys., **29** (1990) 871.

[5] M. Hoshi, S. Sawada, M. Ikeya and T. Miki, in: ESR Dating and Dosimetry, eds., M. Ikeya and T. Miki (Ionics

Co., Tokyo, 1985) p.407.

[6] J. Tatsumi and S. Okajima, in: ESR Dating and Dosimetry, eds., M. Ikeya and T. Miki (Ionics Co., Tokyo, 1985) p.397.

[7] M. Ikeaya, T. Miki, A. Kai, M. Hoshi, Radiat. Prot. Dosim., **17** (1986) 181.

[8] J.E. Aldrich and B. Pass, Health Phys., **54**, (1988) 469.

[9] T. Shimano, M. Iwasaki, C. Miyazawa, T. Miki, A. Kai and M. Ikeya, Appl. Radiat. Isotop., **40** (1989) 1035.

[10] M. Ikeya and M. Furusawa, Oral Radiol., **4** (1988) 133.

[11] M. Furusawa and M. Ikeya, Analy. Sci., **4** (1988) 649.

[12] H. Ishii, M. Ikeya and M. Okano, J. Nucl. Sci. Tech., **27** (1990) 1153.

[13] M. Sagawa, S. Fujimura, N. Togawa, H. Yamamoto and Y. Matsuura, J. Appl. Phys., **55** (1984) 2083.